

國立交通大學

電子物理研究所

博士論文

介觀物理下的兩個主題之

壹：顆粒鉻薄膜的電導率及穿隧電子態密度

貳：單重態自旋電子在量子點中的自旋阻滯

Two topics on mesoscopic electron transport

Part I : Conductivity and tunneling density of states in granular Cr films

Part II : Spin blockade with spin singlet electrons

研究生：孫羽澄

指導教授：林志忠 教授

中華民國一〇二年一月

國立交通大學

電子物理研究所

博士論文

介觀物理下的兩個主題之

壹：顆粒鉻薄膜的電導率及穿隧電子態密度

貳：單重態自旋電子在量子點中的自旋阻滯

Two topics on mesoscopic electron transport

Part I : Conductivity and tunneling density of states in granular Cr films

Part II : Spin blockade with spin singlet electrons

研究生：孫羽澄

指導教授：林志忠 教授

中華民國一〇二年一月

介觀物理下的兩個主題之

壹：顆粒鉻薄膜的電導率及穿隧電子態密度

貳：單重態自旋電子在量子點中的自旋阻滯

Two topics on mesoscopic electron transport

Part I : Conductivity and tunneling density of states in granular Cr films

Part II : Spin blockade with spin singlet electrons

研究生：孫羽澄

Student : Yu-Chen, Sun

指導教授：林志忠

Advisor : Juhn-Jong, Lin

國立交通大學
電子物理研究所
博士論文

1896

A Dissertation

Submitted to Electrophysics Department

College of Science

National Chiao Tung University

in Partial Fulfillment of the Requirements

for the Degree of

Doctor of Philosophy

in

Electrophysic

2013/01

Hsinchu, Republic of China

中華民國一〇二 年一月

介觀物理下的兩個主題之

壹：顆粒鉻薄膜的電導率及穿隧電子態密度

貳：單重態自旋電子在量子點中的自旋阻滯

研究生：孫羽澄

指導教授：林志忠

國立交通大學電子物理研究所博士班

摘要

在本篇論文中，共分有兩個主題，在主題一顆粒鉻薄膜的電導率與穿隧電子態密度的實驗中，我們在低溫下測量了四個 鋁/氧化鋁/鉻 穿隧接點的穿隧微分電導以及鉻電極的電導率。我們所製作的鉻薄膜電極為三維，並具有顆粒性，而其顆粒間的無維穿隧電導 (dimensionless intergrain tunneling conductance spanning) 介於接近一到遠大於一之間，量測到的穿隧電導曲線在零偏壓附近有一甚大的奇異點，且在低偏壓 (幾個微電子伏特) 下，與偏壓的對數有正比關係，而過渡到高偏壓時，則轉變為與偏壓的平方根成正比。同時，鉻電極的電導在某特徵溫度下亦反映了與溫度的對數有對應關係。此實驗結果可以近年來提出的顆粒金屬理論解釋。此外，在無維穿隧電導介於接近一的樣品，除了鉻電極的電導反映了與溫度的對數有對應關係外，我們亦觀察到歸一化的微分電導 $([G(V, T) - G(0, T)]/\sqrt{T})$ ，與參數 $(\sqrt{e|V|/k_B T})$ 在絕對溫度 2.5 到 32 K 之間有一統一定比 (universal scaling) 行為，但此結果還需要理論上的解釋

另一方面，在主題二當中，我們在雙電子垂直雙量子點系統內，觀察到單重態電子自旋阻滯的現象。相對於之前曾被觀察到因三重態電子所導致的包立自旋阻滯 (Pauli spin blockade)，此現象是在高磁場下被觀察到，而其一量子點的雙電子基態在此磁場下已經過單重態-雙重態轉換 (the singlet-triplet transition)。在菱形庫倫阻滯量測中所觀察到自旋阻滯所發生的區域範圍與實驗中雙子點能階頻譜的結果一致，更支持單重態電子自旋阻滯發生於此系統中。此外，我們在單重態自旋阻滯下發現了約為 10 皮安培的漏電流，此數量級的漏電流與電子單重態在核自旋擾動下的維持時間 (lifetime) 符合。

關鍵詞 1. 金屬/絕緣體/金屬 結構，共振穿隧，非晶材料電導率與態態
2. 量子點內電性傳輸，自旋相關電性傳輸，庫倫阻滯

Two topics on mesoscopic electron transport -- Part I : Conductivity and tunneling density of states in granular Cr films; Part II : Spin blockade with spin singlet electrons

Student : Yu-Chen, Sun

NCTU Advisor : Dr. Juhn-Jong, Lin

Riken Advisor : Dr. Keiji Ono

Department of Electrophysics, National Chiao Tung University

ABSTRACT

There are two topics in this thesis. In the first topic, conductivity and tunneling density of states in granular Cr films, we have measured the tunneling differential conductances, $G(V)$, of four Al/AlO_x/Cr planar tunnel junctions as well as the conductivities, $\sigma(T)$, of the Cr electrodes at liquid-helium temperatures. The Cr electrodes were made to be granular with dimensionless intergrain tunneling conductance spanning from $g \approx 1$ to $g \gg 1$, and the dimensionality of the granular array $d = 3$. For the samples with $g \gg 1$, we found that the measured $G(V)$ curves display large zero-bias singularities which obey a $\ln V$ law at low bias voltages (\lesssim a few meV), while crossing over to a \sqrt{V} law at high bias voltages. Simultaneously, the conductivities of the Cr electrodes reveal $\ln T$ dependence below a characteristic temperature. These results are explained in terms of the recent theory of granular metals. In a sample with $g \approx 1$, in addition to the conductivity dependence $\sigma(T) \propto \ln T$, we observed a universal scaling behavior of the normalized differential conductance $[G(V, T) - G(0, T)]/\sqrt{T}$ with the combined parameter $\sqrt{e|V|/k_B T}$ in a wide temperature interval of 2.5 to 32 K. This result awaits a theoretical interpretation.

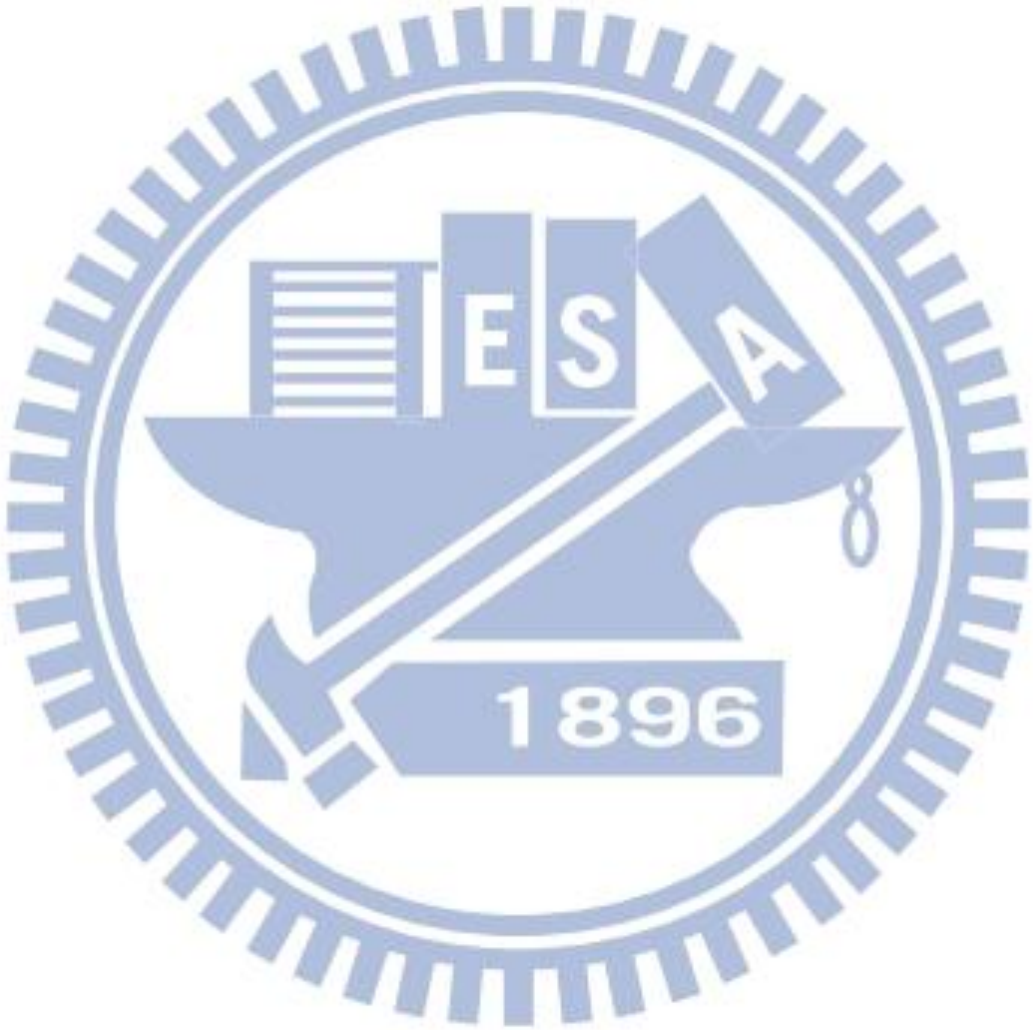
As for the second topic, spin blockade with spin singlet electrons, we observe a novel spin blockade in two-electron vertical double quantum dots where the single electron transport is blocked for spin singlet electrons. In contrast to the conventional Pauli spin blockade with spin triplet electrons, this singlet spin blockade (SSB) is observed under high magnetic field, where the doubly occupied states in one of the dots go beyond the singlet-triplet ground-state transition. The SSB region in Coulomb diamond measurements is in agreement with the two-electron excitation spectrum. A leakage current of 10 pA order is observed in SSB, which is consistent with the spin singlet lifetime due to random nuclear spin fluctuations.

Keywords: electron states at surfaces and interfaces , metal-insulator-metal structures, amorphous (conductivity) , resonant tunneling , electronic transport in quantum dots Coulomb blockade , spin polarized transport through interfaces.

誌謝

Acknowledgement

感謝我生活中的所有，獻給這一路上無論是幫助、陪伴及出現在生活中的人。



Contents

中文摘要	i
Abstract	ii
Acknowledgement	iii
Contents	iv
List of Tables	vii
List of Figures	viii
 Part I Conductivity and tunneling density of states in granular Cr films		
 1. Introduction		
1.1 A Puzzle in Chromium Systems	2
1.2 The Introduction on Granular Conductors	6
1.3 Why We Study Granular Cr films	8
 2. Background and Theory		
2.1 Tunneling in Metal-Insulator-Metal Tunnel Junctions	12
2.2 The BDR Model		
— Background Tunneling Conductance in Tunnel Junction	16
2.3 The Electron-Electron Interaction in Disorder System	18
2.4 Theoretical Prediction for Granular Electronic Systems	20

3. Experimental Method

3.1 Sample Fabrication	23
3.2 Experimental Methods	28
3.3 Experimental Setups	33

4. Result and Discussion

4.1 Temperature Dependence of Conductivity Curves	36
4.2 Temperature Dependence of Differential Conductance Curves	40
4.3 A Comparison with the Conventional EEI Effect	46
4.4 A Comparison with the Theory of Granular Metals	
— Logarithmic temperature dependence of conductivity	50
4.5 A Comparison with the Theory of Granular Metals	
— Differential conductance curves and tunneling density of states	53

5. Summary

Summary	57
---------------	----

Part II Spin blockade with spin singlet electrons

6. Introduction

6.1 Motivation	59
6.2 (A Proposal) To Entangle Nuclear Spins with Singlet Spin Blockade	62

7. Background and Theory

7.1 Single Quantum Dot Systems	66
7.2 Vertical Double Quantum Dots	73
7.3 Pauli Spin Blockade	80
7.4 The Two-Electron Energy Diagram	83
7.5 Introduction to the Singlet Spin Blockade	86

7.6 The Singlet-Triplet Transition in a Two-Electron Quantum Dot	88
8. Device Fabrication and Experimental Setups	
8.1 Structure of Devices	93
8.2 Device Fabrication	96
8.3 Low Temperature Measurement	98
9. Results and Discussions	
9.1 Experimental Conditions	101
9.2 The Two-Electron Excitation Spectrum.	104
9.3 Spin Blockade in the Vsd-Vg Diagram under Magnetic Fields	106
9.4 Hyperfine Interaction Leads to a Short Lifetime of Spin Singlet State	112
10. Summary and Further Works	
Summary and Further Works	114
Appendix	
(A) Expected Value of the Entangled Pairs of Nuclear Spins under SSB	116
(B) Constant Interaction Model for Single QD	124
(C) Constant Interaction Model for double QDs	128
(D) Device Fabrication	131
Reference	143

List of Tables

Part I Conductivity and tunneling density of states in granular Cr films

Table 1 Values for relevant parameters of the Cr electrodes in Al/AlO_x/Cr tunnel junctions.

A_j is the junction area and R_j is the junction resistance at 300 K. t is the thickness, $\rho (R_{\square})$ is the resistivity (sheet resistance) at 2.5 K, and $N_{cr,d}(0)$ is the DOS at the Fermi energy. $k_F \ell$ was calculated by using the Drude model. The diffusion constant D was evaluated through the Einstein relation $\rho^{-1} = N_{cr,d}(0)e^2 D$. The values of $k_F \ell$ and D were evaluated for 2.5 K. E_c, σ_0, g and a are defined in Sec. 2.4. Notice that the values of a are only listed for reference, because our Cr granules are disk-shaped rather than spherical. 27

Part II Spin blockade with spin singlet electrons

Table 2 Electron spins vs. nuclear spins as quantum information carriers 62

Table 3 Relevant parameters of the wafer used in our double QD device 95

List of Figures

Part I Conductivity and tunneling density of states in granular Cr films

Fig. 1.1 (a) Conductances versus voltage plot of several normal metal junction exhibiting different zero-bias behaviors. The Data were taken at 1 K..... 4

Fig. 1.1 (b) The measured normalized conductance of Al/AlOx/granular aluminum tunnel junction. The resistivities of the samples are in a range from $4.26 \times 10^{-2} \Omega cm$ (AL6) to $3.28 \times 10^{-4} \Omega cm$ (AL42). The data is taken at 0.95 K, and those at low bias where the superconducting energy gap structure dominates is omitted here 5

Fig. 1.2 (a) Electron micrographs of Ag deposited on a bent substrate of amorphous carbon (a-c) in a rate of 0.1 pm s^{-1} at room temperature 7

Fig. 1.2 (b) TEM image of a granular system composed by a gold nanocrystal monolayer...
..... 7

Fig. 1.3 (a) The temperature dependence electrical transport behaviors of the granular systems in previous studies: (Up) A logarithmic temperature dependence of the resistivity of the granular NbN cermet film (in a sample with $R_{\square}(300 \text{ K}) \sim 100 \Omega/\square$) [21]. (Down) A logarithmic temperature dependence of the conductivity of the granular Pt/C nanowires ($\rho(300 \text{ K}) \sim 4 \text{ m}\Omega \text{ cm}$) in a wide range of up to 200 K..... 10

Fig. 1.3 (b) Previous,y, the regime $g \ll 1$ in the granular has been verified to have the Efros-Shklovskii type temperature dependence, where the $\sigma \propto \exp(-\sqrt{T_0/T})$ behavior, in our experiment. In this experiment, the nanocontacts formed with granular Cr films, and the

difference between the two curve is the contact resistance. And it was observed in the broad temperature interval of 1 – 100 K, $\log R$ is a function of $T^{-1/2}$ 11

Fig. 2.1 (a) The schematic energy diagram of a metal-insulator-metal (M_1 -I- M_2) tunnel junction with a finite bias V . $\phi(x)$ describes the barrier potential. The net tunneling current flow through the junction should be the summation of current from left to right and that from right to left, i.e. $I = I_{12} + I_{21}$ 15

Figs. 2.2 (a-b) The schematic energy diagram of a metal-insulator-metal (M_1 -I- M_2) tunnel junction with (a) zero-bias (b) a finite bias V . Under BDR model, the potential of the barrier $\phi(x)$ can be described to be $\phi(x, V) = \phi_1 + \frac{x}{t}(\phi_2 - eV - \phi_1)$ (so that) $\phi(x, 0) = \phi_1 + \frac{x}{t}(\phi_2 - \phi_1)$ for (a) the zero-bias. 17

Figs. 3.1 (a-c) Schematic diagrams of the top views (left) and side views (right) of our sample during the fabrication progresses: (a) The evaporated Al film; (b) Utilizing O_2 plasma to oxidize the surface of the deposited Al film; (c) Depositing Cr film to cross the AlO_x/Al structure. The side view shows the junction area where the red dotted lines enclose on the left top view figure..... 25

Fig. 3.1 (d) The AFM image of a thin Cr layer, prepared by thermal evaporation deposition on a mica substrate, shows the granular property. The surface profile below is along the solid line indicated in the AFM image 26

Fig. 3.2 (a) Diagrams depicting (up) four-probe resistance measurements of Cr electrodes, and (down) differential conductance measurements of $Al/AlO_x/Cr$ tunnel junctions. Black

strips stand for Al films, and green (gray) strips for Cr electrodes..... 29

Fig. 3.2 (b) The equivalent circuit for the differential conductance measurements for Cr electrodes. 30

Fig. 3.2 (c) The differential conductance measurement of the most disordered Cr electrode, sample D, at temperature $T = 0.25, 0.5, 1, 2.2$ K where the Al electrode has already been superconducting. The barrier quantity can be tested and verified by the signature of the superconducting gap, since $G(V) = dI(V)/dV$ is a function of $N_{Cr}(V)$ and $N_{Al}(V)$. The measured result reveals the superconducting gap at $T = 0.25$ K is $\lesssim 0.5$ meV, while the calculated energy gap for Al being superconducting at 1.14 K is 0.34 meV. The data (■) shows the superconductivity is destroyed by the applied magnetic field. 31

Fig. 3.3 (a) The photo (left) and schematic figure (right) of He^3 cryostats..... 35

Fig. 4.1 (a) Normalized resistivity, $\rho(T)/\rho(280$ K), as a function of temperature of the Cr electrodes in junctions A – D, as indicated..... 38

Fig. 4.1 (b) Conductivity as a function of temperature of the Cr electrodes in junction B and junction D. The straight solid lines are least-squares fits to the equation of conductivity in Sec 2.4..... 39

Fig. 4.2 (a) Normalized differential conductance, $G(V)/G(70$ mV), as a function of bias voltage for junctions A, C and D, as indicated. Notice that the $G(V)$ curves are essentially symmetric around the zero bias voltage. Data were taken at 2.5 K..... 41

Fig. 4.2 (b) The $G(V)$ curve of junction A in zero magnetic field (symbols) and in a perpendicular magnetic field of 4 T (solid curve). Notice that the magnetic field causes a negligible change. Data were taken at 2.5 K..... 42

Fig. 4.2 (c) The $G(V)$ curve of junction D in zero magnetic field (symbols) and in a perpendicular magnetic field of 4 T (solid curve). Data were taken at 2.5 K..... 43

Fig. 4.2 (d) Normalized differential conductance, $G(V)/G(10\text{ mV})$, as a function of bias voltage for junctions A – D, as indicated. The straight solid lines are least-squares fits to the equation of conductivity in Sec.2.4. For clarity, the data for the junctions B, C and D have been vertically shifted up by 0.1, 0.2 and 0.8, respectively. Data were taken at 2.5 K..... 44

Fig. 4.2 (e) $G(V)/G(10\text{ mV})$ versus \sqrt{V} for junctions A, C and D, as indicated. The straight solid lines are guide to the eyes. Data were taken at 2.5 K..... 45

Fig. 4.3 (a) $G(V)$ spectra of junctions A at 2.5 K in a wide bias voltage interval, as indicated. The symbols are the experimental data and the solid curves are parabolic fits. The solid curves in junctions A are described by $G_{\text{para}}(V) = 848 + 0.067V + 0.0028V^2$ where $G_{\text{para}}(V)$ is in microsiemens and V in millivolt..... 48

Fig. 4.3 (b) $G(V)$ spectra of junctions D at 2.5 K in a wide bias voltage interval, as indicated. The symbols are the experimental data and the solid curves are parabolic fits. The solid curves in junctions D are described by $G_{\text{para}} = 272 - 0.12V + 0.0026V^2$, respectively, where G_{para} is in microsiemens and V in millivolt..... 49

Fig. 4.4 (a) Plots of temperature-dependent conductivities in Junction A under magnetic field

H = 0 T (triangles) and H = 4 T (squares). The small difference between two curves is within our experimental uncertainty. The results confirm that the WL effect (which is sensitive to the magnetic fields) is irrelevant to our system, while the prediction on conductivity in the theory of granular metals should be valid at any magnetic field..... 52

Fig. 4.5 (a) Normalized differential conductance, $(G(V, T) - G(0, T))/\sqrt{T}$, as a function of the combined parameter $\sqrt{eV/k_B T}$ for the junction D at five measurement temperatures. Notice that the data points collapse closely..... 55

Fig. 4.5 (b) Unscaled $G(V)$ versus bias voltage V at (from bottom up) 2.5, 5.0, 9.0, 16 and 32 K..... 56

Part II Spin blockade with spin singlet electrons

Fig. 6.2 (a) The schematic diagram of the hyperfine interaction in a double QD system, where \uparrow/\uparrow shows the electron/nuclear spin direction and α is the coupling strength..... 64

Fig. 7.1 (a) Schematic diagrams of semiconductor heterostructures such as AlGaAs/GaAs/AlGaAs that confine electrons to a plane..... 67

Figs. 7.1 (b-c) The equivalent circuits for the (b) vertical and (c) lateral quantum dot system. The gate couples to the dot capacitively, and barriers between electrode reservoirs and the dot can be represented as a parallel connection of resistance and capacitor..... 68

Fig. 7.1 (d) Coulomb Oscillations, the current peaks measured at $V_{sd} \approx 0$. The peaks only happens when $\mu(N) = \mu_s = \mu_d$, and we can tune $\mu(N)$ with V_g . The difference between the two neighboring peaks is the addition energy..... 70

Figs. 7.1 (e-f) The schematic diagram for (e) Coulomb oscillation occurring (f) releasing the blockade situation as $eV_{sd} \geq E_{add}$ 71

Fig. 7.1 (g) The measured Coulomb diamonds in the $V_{sd} - V_g$ diagrams revealing the shell structures of the dot 71

Fig. 7.1 (h) the Coulomb diamond boundary conditions are determined by the alignment of the chemical potential between either one of the lead and the dot, i.e. $\mu(N) = \mu_s$ or μ_d ...
..... 72

Figs. 7.2 (a-b) (a) A schematic diagram for a vertical double dot system in a crossing-section view. Two dots are separated and sandwiched by barriers, and their sizes are controlled by the depletion region due to Schottky gates, the drawn golden parts surrounding the dot side. (b) The equivalent circuits for the double vertical quantum dot system. Comparing with single dot as Fig. 7.1 (b), there is one more parameter as the interdot capacitance, which describes the interaction between dots due to the coupling, concluded..... 73

Figs. 7.2 (c-d) (c) The charge stability diagram for double quantum dot systems. (d) Three corresponding level diagram w.r.t the colored circles in Fig. 7.2 (c). Here, we treat two dots as individual ones. Electrons can do the first-order tunneling only at blue point(s)..... 74

Figs. 7.2 (e-f) The (e) schematic and (f) measured honeycomb diagrams revealing the

coupling between two dots. (g) Diagrams of corresponding chemical potentials of dots and leads at the colored circles in (e). Notice that along the line linking up the paired circles, states in each dot are tuned simultaneously and equally. Unlike Fig. 7.2 (c), the chemical potentials represented as $\mu_{1/2}(n1, n2)$ here are due to the interdot coupling..... 76

Fig. 7.2 (h) The $V_{sd} - V_g$ schematic diagram for the double dot systems. The block lines sketch the contours of blockade regions. Within the blockade area, red and blue lines show a second-tunneling process. The vertical lines indicate an offset between dots, or the offset number is revealed as the numbers of the vertical line..... 77

Fig. 7.2 (i) The measured $V_{sd} - V_g$ diagram of the double dot systems in dI_{sd}/dV_{sd} plots. The vertical line indicates an offset = 1 and the corresponding positions of levels are in Fig. 7.2 (j)..... 78

Fig. 7.2 (j) The corresponding energy level diagrams for a double dot system with interdot offset = 1. At condition **a**, we can clearly see the energy difference between two dots. Condition **b** is along the vertical line, while **c** is at the kink side. For **b** electrons tunnel through the system via the two aligned ground states at an infinite source-drain bias, The applied gate voltages simultaneously and nearly equally tune states in both dots. Therefore, we have a vertical line, as the tunneling boundary, along the V_g axis..... 79

Fig. 7.3 (a) Schematic level diagrams of the Pauli spin blockade: During the $(0,1) \rightarrow (1,1) \rightarrow (0,2) \rightarrow (0,1)$ cycle, $(1,1)$ has both probability to be either spin singlet or triplets, so the electron may transport until SB will eventually occurs..... 81

Fig. 7.3 (b) In the $V_{sd} - V_g$ diagram, SB shows an asymmetric current suppressed region at

$N=2$ as the area green lines enclose. The small current in other red color region is due to the co-tunneling process 82

Fig. 7.3 (c) The schematic diagram of the triplet tunneling channel developed by applying V_{sd} . The V_{sd} bias crossing on three barriers tunes the relative energy between the dots. The energy difference between $T(1,1)$ and $T(0,2)$ is compensated by a finite and large enough V_{sd} bias, and release the spin blockade..... 82

Fig. 7.3 (d) Spin blockade in the $V_{sd} - V_g$ diagram. A triplet tunneling channel developed at high bias as the arrow marks..... 83

Fig. 7.4 (a) The Energy levels of two-electron states in double QDs as a function of detuning under the conditions of $t_c \sim 0$; $H = 0$. For $H = 0$ T, we can ignore the Zeeman splitting terms in triplets. The hybridized states are formed at the crossing of singlets and triplets due to the coupling t_c 85

Fig. 7.4 (b) The Energy levels of two-electron states in double QDs as a function of detuning under the conditions of $t_c > 0$; $H = 0$ 86

Figs. 7.5 (a-b) Schematic diagrams for the mechanism of (a) a conventional Pauli spin blockade and (b) a singlet spin blockade..... 87

Fig. 7.6 (a) The Fock-Darwin spectrum describes a single electron within a 2D parabolic confinement under magnetic fields. At high magnetic field, the Landau levels are formed as marked $(n,l)=(0,0),(0,1),(0,2),(0,3)$ Note that the spin degeneracy is ignored here..... 89

Fig. 7.6 (b) The calculated electrochemical potential μ of a two-electron dot as a function of magnetic field for $\hbar\omega_0 = 5.6$ meV, $E_c = 5$ meV at 10 T: The lower solid curve is the ground state (GS), while the upper one is the excited state (ES). Dashed lines represent the situation involving the B-dependent Coulomb interaction. Due to the larger overlap of W.F. when both electrons staying in GS, the dashed line of GS grows faster than that of ES. The upper dashed curve with subtraction of a constant exchange energy results in the dotted curve. The GS, before and after the S-T transition, is indicated by a dashed-dotted line..... 90

Fig. 7.6 (c) Plot of $I_{sd}(V_g, B)$ measured in a single QD system with $V_{sd} = 0.1$ meV which is so small to show only the ground states (of $N = 1$ to 5). For $N = 2$, the ground-state transition is marked with a triangle. The spin configurations, indicated with the arrows, show the transition from spin singlet to be spin triplet as gradually applying the magnetic field from 0 to 4.15 T. Note that the system gains additional exchange energy when the spins of two electrons are parallel 92

Fig. 8.1 (a) Schematic energy diagram of a double QD device where only the ground state in the z-direction occupied. The equilibrium in electrostatic potential among the electrodes and well is reached..... 94

Fig. 8.2 (a) A simplified diagram for the wafer structure as in Table 3..... 96

Figs. 8.2 (b-f) The main fabricating process in both aerial view and cross-section figures. (b) The first cross-section figure shows the deposited Ti/Au bottom and top contact. Titanium here is used for bonding metal electrodes and the substrate more tightly. The second and third cross-section figures are steps for the pillar structure. The dry etching process is to “sculpt” the pillar shape and the following wet etching further lessen semiconductor parts of

the pillar in width and in depth until beneath the layers of three barrier structures. (c) Evaporating the metal gates around the pillar. (d-f) are steps for the contact pads for wire bonding. In (d), we use wet etching beneath the semi-insulating substrate; (e) step smoother with hard bake resist; (f) evaporating the metal contacts..... 97

Figs. 8.2 (g-j) Photos of device similar with our samples. (g) A SEM image of a double-gate vertical QD device. (h) A image under optical microscope; two devices are included. (i) Contact pads for wire bonding. (j) A sample wire bonding to a chip carrier..... 98

Figs. 8.3 (a-b) (a) Copper powder filters, which can work well as a low pass filter even at low temperatures, are launched between the sample holder and mixing chamber of the fridge (b) The structure of the copper powder filter..... 100

Fig. 9.1 (a) dI_{sd}/dV_{sd} plots under magnetic field from 0 to 5 T. The Spin blockade region is indicated by the dotted line at 0 T. The triplet channel which collapses the spin blockade is marked by arrows. With increasing the magnetic field, the triplet channel enters into the SB region and approaches to the zero bias, but the CB is still left 102

Fig. 9.1 (b) The $V_{sd} - V_g$ diagrams measured at 0 T with different gate conditions. The upper diagram shows the offset=1 case where $\mu_1(1,1) = \mu_2(0,2)$, whereas $\mu_1(1,1) > \mu_2(0,2)$ at the underlying diagram. These two diagrams demonstrate the ability to detune the interdot offset in our device..... 103

Fig. 9.2 (a) The Coulomb diamond diagram at 0 T. To measure the two-electron state energy spectrum, we sweep gate voltages along the yellow arrow to trace the variation of chemical potential of (0,2) states from 0 to 10 T, and the result is shown in Fig. 9.2 (b). The yellow

line indicated $\mu_2(0,2)$ is the ground (0,2) state before the S-T transition..... 104

Fig. 9.2 (b) The excitation energy spectrum for (0,2) states, measured at $V_{sd} = -4$ mV. The first current strip exhibits the (0,2) state evolution among the solid line of the $1s^2$ orbital (0,2) state with spin singlet, the dashed line of the $1s2p^+$ orbital (0,2) state with spin triplet, and the dotted line for another (0,2) state with spin singlet..... 105

Figs. 9.3 (a-b) dI_{sd}/dV_{sd} plots under the magnetic fields of (a) 0.0 T, (b) 2.0 T. The arrows mark the threshold of SB..... 108

Figs. 9.3 (c-d) dI_{sd}/dV_{sd} plots under the magnetic fields of (c) 4.0 T, (d) 5.0 T. The arrow marks the threshold of SB. At 5.0 T, SB is completely relieved and only the Coulomb blockade region is left..... 109

Figs. 9.3 (e-f) dI_{sd}/dV_{sd} plots under the magnetic fields of (e) 6.2 T, (f) 7.4 T. The arrows mark the threshold of SSB..... 110

Fig. 9.3 (g) Plots of the energy difference between the ground and 1st excited (0,2) states, ΔE_{ge} . Circles indicate data extracted from (0,2) excitation spectrum in Fig. 9.2 (b), and triangles are data from the series of Coulomb diamond measurements shown in Figs. 9.3 (a-f). ΔE_{ge} measured as V_{gL}/V_{gR} (Fig. 9.2 (b)) and V_{sd} (Figs. 9.3 (a-f)) are converted to energy using the voltage drop ratio of three tunneling barriers. 111

Fig. 9.4 (a) The $I_{sd} - V_{sd}$ curve along the dashed line in the insert $V_{sd} - V_g$ diagram measured at 7.4 T. A leakage current of 10 pA is observed in the SSB region..... 113

Fig. A (a) The schematic diagram of the electron/nuclear spins, represented as \uparrow/\uparrow , in a imaged system that there are only two nuclear spins in each dot. Under SSB, the system is blocked with electron spin singlet until it interacts with nuclear spins via the hyperfine interaction and release the SSB by spin flip-flop process which passes the entanglement to the nuclear pairs. The α indicates the hyperfine interaction strength (see Sec. 6.2)..... 116

Fig. A (b) The diagram that the nuclear spins change among mix^2 , $S \cdot \text{mix}$, and S^2 condition. The arrow show the change of the direction and the number above is the change probability..... 119

Fig. A (c) Assuming there are N nuclear spins in both QD1 and QD2, then after nth hyperfine interaction to exchange the spin state with electron spin singlet under SSB, the nuclear spins have mix^N , $S \cdot \text{mix}^{N-1}$, $S^2 \cdot \text{mix}^{N-2}$, ... or S^N possible conditions..... 121

Fig. A (d) The diagram of the nuclear spins changing among the mix^N , $S \cdot \text{mix}^{N-1}$, $S^2 \cdot \text{mix}^{N-2}$, ... or S^N possible conditions. Whenever the interaction acts at the condition of $S^n \cdot \text{mix}^m$ ($n + m = N$), it may change to be $S^{n+1} \cdot \text{mix}^{m-1}$, $S^n \cdot \text{mix}^m$ or $S^{n-1} \cdot \text{mix}^{m+1}$. The arrow show the change of the direction and the number above is the probability..... 121

Fig. B (a) An equivalent circuit for the single-quantum-dot system. The dot connected to the leads via tunnel barriers is characterized by parallel series of the resistor R_s/R_d and the capacitor C_s/C_d , while it capacitively couples to the gate through a capacitor C_g 124

Fig. B (b) A schematic diagram of the levels in single quantum-dot device, the electron can

flow via the system only when levels falls within the bias window determined by μ_s and μ_d 125

Fig. B (c) The schematic diagram for a Coulomb diamond. The alignment between $\mu(N)$ and at least one of μ_{lead} determines the boundaries. 126

Fig. B (d) The energy spectrum of a single dot represented in dI_{sd}/dV_{sd} on the $V_{sd} - V_g$ plane. The white area is the Coulomb Blockade region where no electron can flow through the dot until $-|e|V_{sd} (= \mu_s - \mu_d) \geq E_{add}$ 127

Fig. C (a) As single dot in Fig. B (a), a double quantum dot system connected to the leads and gates can be also characterized by resistors and capacitors. Besides, the tunnel barrier separating two series-connected dots is represented by a resistor R_m and a capacitor C_m , while the tiny cross-capacitances (such as between V_{g1} and dot 2) are ignored..... 128

Figs. C (b-c) Electrochemical potential levels in a double-dot system. Electrons can tunnel through the system via the sequence of (b) $(N_1, N_2) \rightarrow (N_1 + 1, N_2) \rightarrow (N_1, N_2 + 1) \rightarrow (N_1, N_2)$ or (c) $(N_1, N_2 + 1) \rightarrow (N_1 + 1, N_2 + 1) \rightarrow (N_1 + 1, N_2) \rightarrow (N_1, N_2 + 1)$ 130

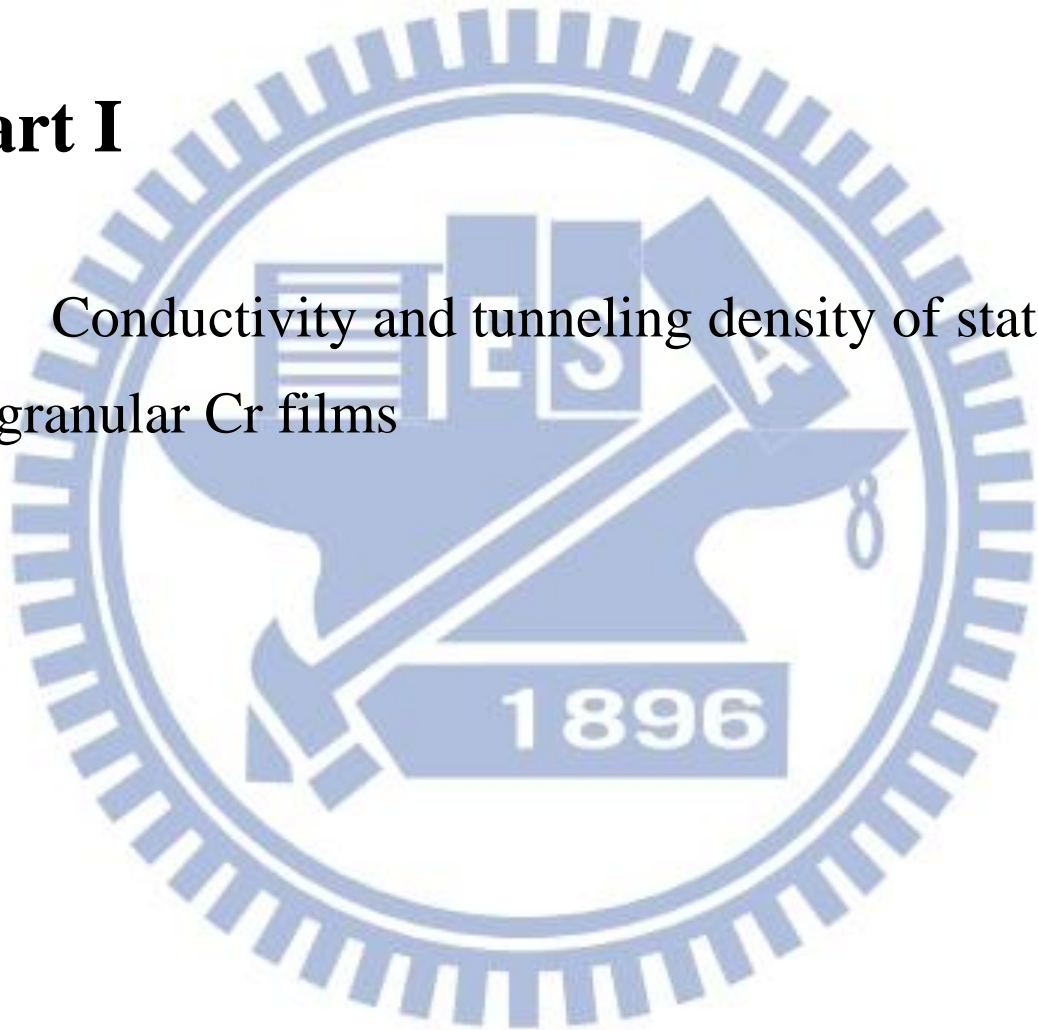
Figs. D (a-b) (a)The wafer is prepared in a size of 9×10 mm (4×10 mm chip for test samples) for the following fabrication processes (b) The simplified schematic diagram of the wafer structure composed of multilayers as Table 3..... 131

Fig. D (c) Schematic diagrams of the top views (left) and the side views (right) of the wafer during the back contact fabrication..... 132

Fig. D (d) Schematic diagrams of the top views (left) and the side views (right) of the wafer during the top contact fabrication.....	133
Fig. D (e) Schematic diagrams of the top views (left) and the side views (right) of the wafer during the dry etch process.....	134
Fig. D (f) Schematic diagrams of the top views (left) and the side views (right) of the wafer during the wet etch process.....	135
Fig. D (g) Schematic diagrams of the top views (left) and the side views (right) of the wafer during the gate fabrication.....	136
Fig. D (h) Schematic diagrams of the top views (left) and the side views (right) of the wafer during the mesa process.	138
Fig. D (i) Schematic diagrams of the top views (left) and the side views (right) of the wafer during the step smoother process.....	140
Fig. D (j) Schematic diagrams of the top views (left) and the side views (right) of the wafer during the bonding pad process.....	141

Part I

Conductivity and tunneling density of states
in granular Cr films



Chapter 1

Introduction

1.1 A Puzzle in Chromium Systems

A half century ago, Rowell and Shen [1] observed a zero-bias anomaly (a “resistance peak”) in Cr/CrOx/Ag tunnel junctions comparatively much larger than the junctions composed by other materials (see Fig. 1.1 (a)). Then subsequently, such a giant zero-bias anomaly has also been found in experiments involving Cr as the electrodes by other groups [2-4]. Rowell and Shen attributed this giant resistance peak (conductance dip) in their Cr/CrOx/Ag junctions to the magnetic nature of the insulating barrier, while CrO₂ is antiferromagnetic and Cr₂O₃ is ferromagnetic. On the other hand, Mezei and Zawadowski [5] suggested that the effect is owing to the Kondo scattering from magnetic moments embedded in the Cr electrode or at the electro-insulator interface. However, the main difficulty with the explanation is that the magnitude of the anomaly was not satisfactory with that stemming from the effect. Thus far, what really accounting for the great zero-bias resistance peaks found in many Cr consisted tunnel junctions has remained mysterious.

On one hand, the Chromium system is antiferromagnetic and its oxide, CrOx, possess magnetic nature, while, on the other hand, it often forms a granular-like structure [6-8] if it is thermally deposited. The forming of granules brings the disorder to the system. Altshuler

and coworkers [9-13] have studied the EEI effect in the presence of weak disorder. They found that the EEI effect causes to a suppression in the electron DOS at the Fermi level. And, it is also predicted that in the weakly disordered regime the density of states (DOS), proportional to the junction conductance, have the dependence on the voltage (energy). Meanwhile, McMillan [14, 15] proposed that the correlation on the DOS of a 3-dimensional (3D) system on metallic side near the Metal-Insulation transition systems is in the form which is similar to the expression given by Altshuler and Aronov [13]:

$$\text{for } E < \Delta, \quad N(E) = N(0)[1 + (E/\Delta)^{1/2}]$$

where $N(0)$ is the DOS at the Fermi energy level E_F , and Δ , called “correlation gap”, is a characteristic energy scale that vanishes as a power of the distance to the metal-insulator transition (for a system crossing over from the metallic side to be the insulator, the correlation gap gradually decreases to zero at the Metal-Insulation transition, and raise again). And, the comparison between this theory and the experiment results on Al/AlOx/granular Al tunnel junction is also made in Ref. [16] (see Fig. 1.1 (b)).

While the puzzle in tunnel junction of the Cr electrode (with the granular property) has not been answered, the theory on granular system is proposed in recently years. Therefore, before analyzing the role the granular property may play in Cr system, we start from giving a briefly introduction on the relative theory in next section.

(a)

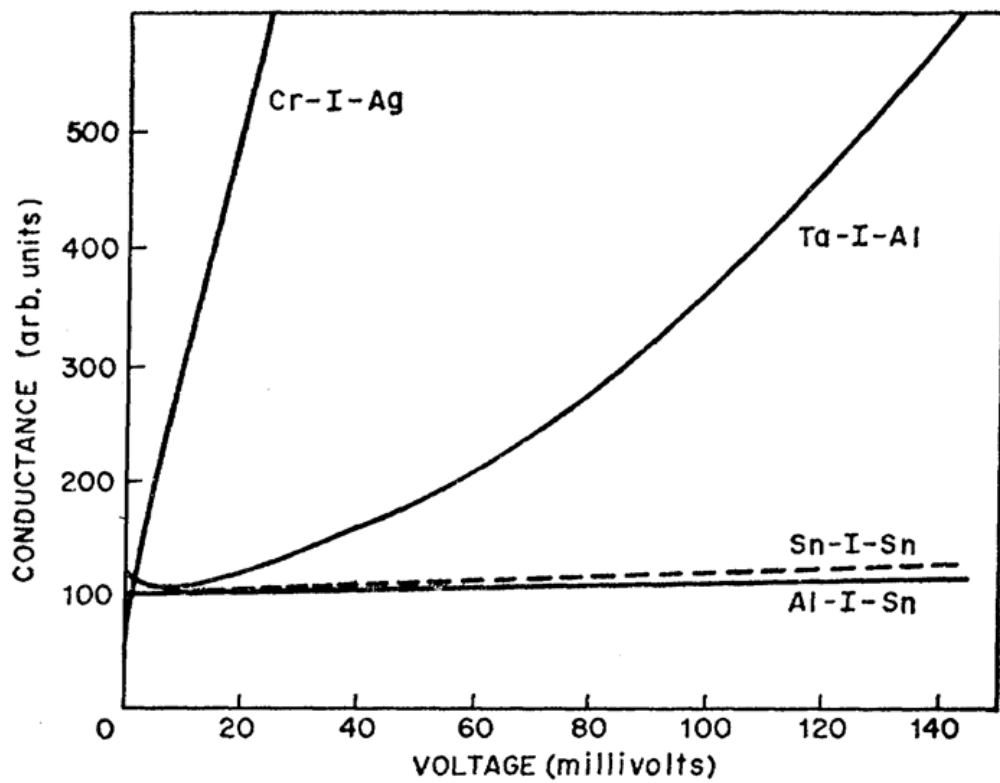


Fig. 1.1 (a) Conductances versus voltage plot of several normal metal junction exhibiting different zero-bias behaviors. The Data were taken at 1 K [17].

(b)

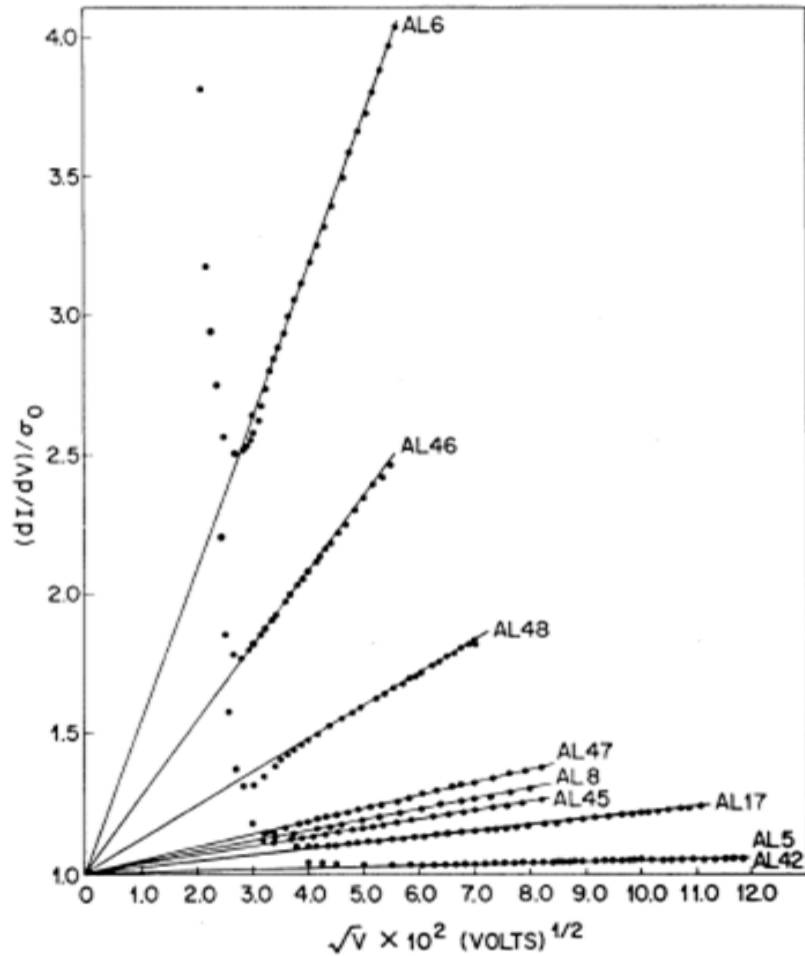


Fig. 1.1 (b) The measured normalized conductance of Al/AIOx/granular aluminum tunnel junction. The resistivities of the samples are in a range from $4.26 \times 10^{-2} \Omega cm$ (AL6) to $3.28 \times 10^{-4} \Omega cm$ (AL42). The data is taken at 0.95 K, and those at low bias where the superconducting energy gap structure dominates is omitted here [16].

1.2 The Introduction on Granular Conductors

The granular conductor here is considered a system with metallic grains embedded in dielectric components. The size of the grain is from a few to hundreds of nm, therefore the metallic grain is often regarded as an artificial atom with the discrete energy spectrum. On the other hand, the tunability of the electric properties of the whole system via the size of the grain, the tunneling coupling between grains, and so on also make the granular conductor treated as an artificial solid. The mean energy level spacing in a single granule (depending on the granular size), δ , the dimensionless tunneling conductance between neighboring granules (i.e. the tunneling coupling), g , and the single-grain Coulomb charging energy, E_c characterize granular material. These parameters are relative to the disorder effect, the quantum confinement, and the electron correlation. The interplay among those effects with tunable parameters we can control brings the attention to the granular conductors.

There are several ways to fabricate the granular system. Traditionally, the granular conductor can be made by sputtering or the thermal evaporation (see Fig. 1.2 (a)). Depending on the material such as chromium in our system, as it deposits on the substrate, it naturally gather to form the granular structure. However, the size of grains is not uniformed. The dielectric component is formed during the evaporation as the surface is oxidized. In some systems, the tunneling coupling between grains is determined and adjusted by covering the organic or inorganic molecules on grains [18]. The other ways to have granular system are, for example, with the self-assembling colloidal nanocrystals or the self-assemble semiconductor quantum dot [19]. The variation of particles in size can be controlled to be within less than with the thermal evaporation method as the gold nanocrystal colloid in Fig. 1.2 (b) [18]. The relative standard deviation of the size is about 5%. As for the self-assemble semiconductor quantum dot, it is utilized the different lattice constant of two

semiconductors.

(a)

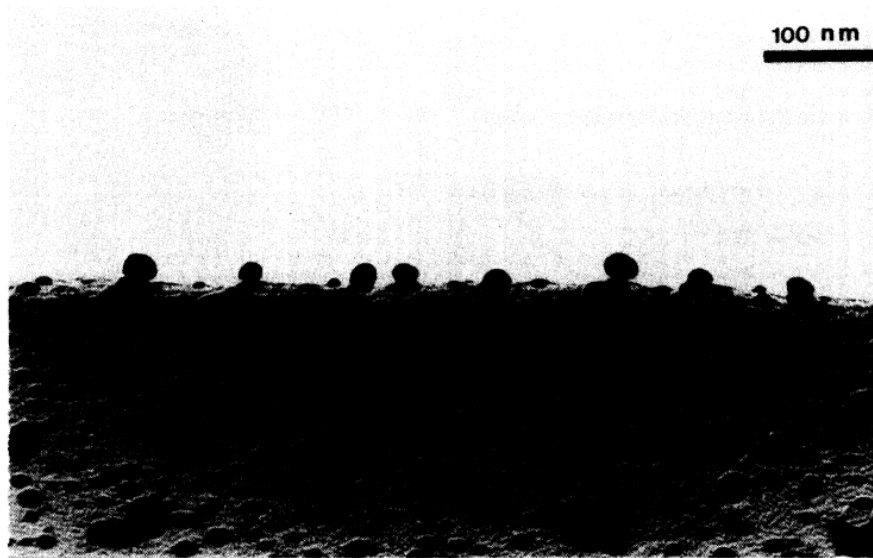


Fig. 1.2 (a) Electron micrographs of Ag deposited on a bent substrate of amorphous carbon (a-C) in a rate of 0.1 pm s^{-1} at room temperature [20].

(b)

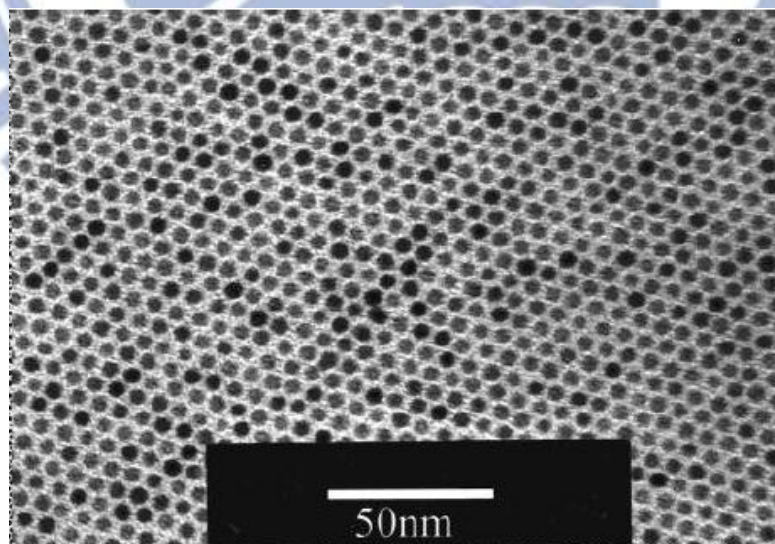


Fig. 1.2 (b) TEM image of a granular system composed by a gold nanocrystal monolayer [18].

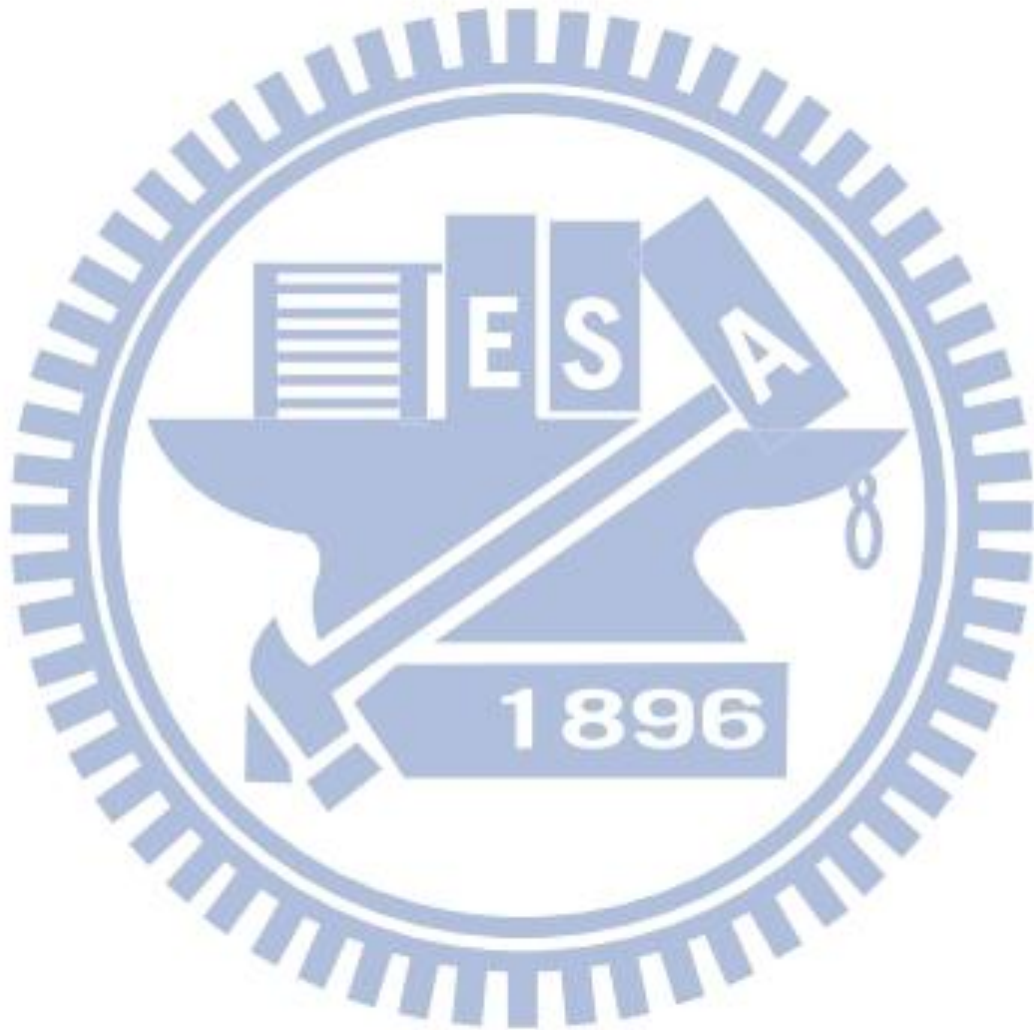
1.3 Why We Study Granular Cr films?

In this thesis, we study four the Al/AlO_x/Cr planar tunnel junctions comprising of granular Cr electrodes. The non-magnetic insulating barrier AlO_x was intentionally used, instead of the magnetic CrO_x, to rule out the possible influence of the magnetic nature of barrier on the tunneling signals. Besides, the attempt to answer the puzzle in history, we also have a great interest in the granular conductors.

Experimentally, it is intriguing that electrical-transport measurements on granular systems with strong intergrain coupling often revealed $\ln T$ dependence of resistivity [21, 22], rather than of conductivity [23, 24] as the theory predicted (see Sec.2.4 and Fig. 1.3 (a)). Therefore, it still awaits convincing experimental test. Moreover, to the best of our knowledge, there is still no experimental observation in three-dimensional (3D) granular films concerning the electronic DOS. Thus, we are motivated to study Al/AlO_x/granular Cr tunnel junctions. The dimensionality of the granular arrays (the Cr electrodes) was made to have $d = 3$, and both conductivities and tunneling DOS of the Cr electrodes (with intergrain tunneling conductance spanning from $g \cong 1$ to $g \gg 1$) are measured to verified the recent theory of granular metals [25-27]. We would like to mention that previously in our experiment, we found a Efros-Shklovskii type temperature dependence in the nanocontacts formed with granular Cr films, where the $\sigma \propto \exp(-\sqrt{T_0/T})$ behavior was observed in the broad temperature interval of 1 – 100 K [6] (see Fig. 1.3 (b)), while the conductivity at low temperatures is theoretically established to possess this type-like dependence in the opposite limit of weak intergrain coupling ($g \ll 1$), for T_0 is a characteristic temperature [23,28-31]. In that case, we experimentally realized the regime $g \ll 1$ [32].

This thesis is organized as follows: In Chap. 2, besides the granular system, the the EEI effects and the property of tunnel junctions are also briefly introduced. We discuss our experimental considerations, methods and setups in Chap. 3. Chapter 4 contains our

experimental results and discussions. We interpret our measured conductivity and tunneling DOS in terms of the theory of granular metals, and rule out the WL and EEI effects developed for weakly disordered homogeneous conductors to be the origins of our observations. Finally, our conclusion is presented in Chap. 5.



(a)

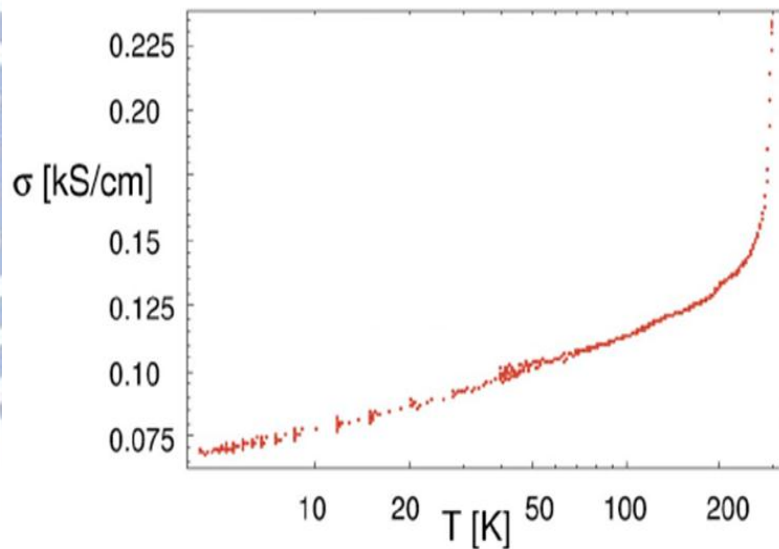
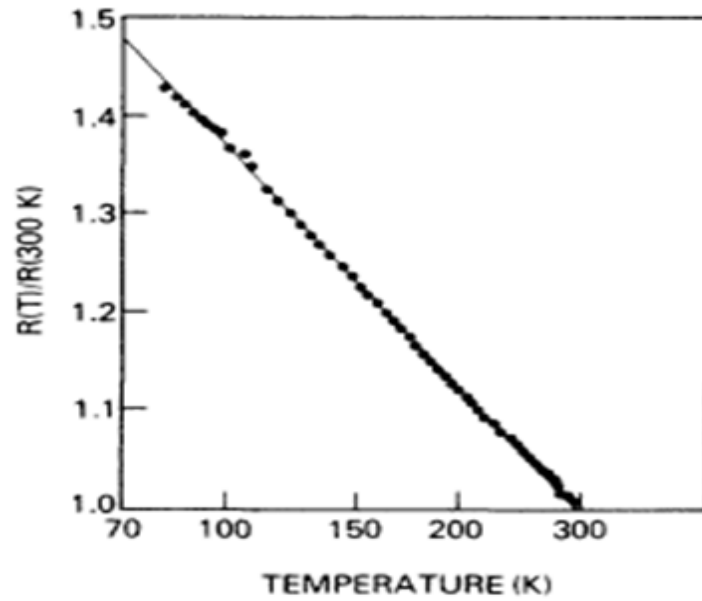


Fig. 1.3 (a) The temperature dependence electrical transport behaviors of the granular systems in previous studies: (Up) A logarithmic temperature dependence of the resistivity of the granular NbN cermet film (in a sample with $R_{\square}(300\text{ K}) \sim 100\ \Omega/\square$) [21]. (Down) A logarithmic temperature dependence of the conductivity of the granular Pt/C nanowires ($\rho(300\text{ K}) \sim 4\ \text{m}\Omega\ \text{cm}$) in a wide range of up to 200 K [24].

(b)

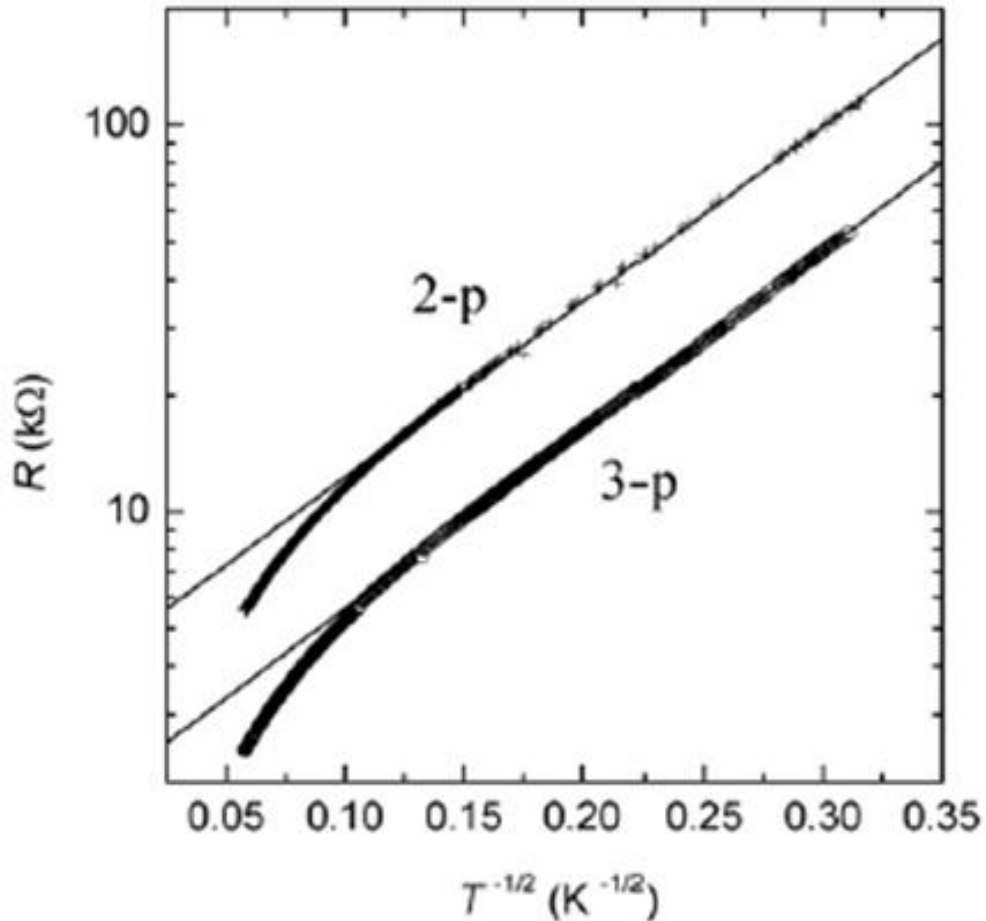


Fig. 1.3 (b) Previously, the regime $g \ll 1$ in the granular has been verified to have the Efros-Shklovskii type temperature dependence, where the $\sigma \propto \exp(-\sqrt{T_0/T})$ behavior, in our experiment. In this experiment, the nanocontacts formed with granular Cr films, and the difference between the two curves is the contact resistance. And it was observed in the broad temperature interval of 1 – 100 K, $\log R$ is a function of $T^{-1/2}$ [5].

Chapter 2

Background and Theory

There are three main parts will be introduced in this chapter. In this thesis, we measure the differential conductance to investigate the DOSs of the granular Cr electrode, so we start with Sec. 2.1 the general ***tunneling behavior in metal-insulator-metal junctions*** and Sec. 2.2 ***the BDR Model describes the background tunneling conductance in the junctions***. Then from Sec. 2.3 to 2.4, theoretical predictions related to our system will be introduced. Since the granular conductor is also a disorder system, ***the electron-electron interaction (EEI)*** effects, which have well explained weak disorder systems, will be mentioned in Sec.2.3. And finally, ***the theoretical prediction for the granular electronic system*** is in Sec. 2.4.

2.1 Tunneling in Metal-Insulator-Metal Tunnel Junctions

In this thesis, we measure the tunneling current through the metal-insulator –metal (M-I-M) tunnel junctions to investigate the DOS of granular conductors. In order to know the relation between the DOS of electrodes and the tunneling current, we start with the basis of the tunneling mechanism and extend to obtain the tunneling current in such a junction structure. Then, the relation of the DOS of electrodes and the differential conductance will be derived.

In classical view, we know that there is no way for a particle passing through a barrier

with a potential higher than its total energy. However, in quantum mechanism, whenever a particle treated as a wave runs into a barrier potential, there will be both probabilities to penetrate it and to be reflected. In our cases, we can consider the energy diagram in a M-I-M tunnel junction similar to Fig. 2.1 (a): $x < 0$ (the left of the barrier), $0 < x < t$ (within the barrier), $t < x$ (the right of the barrier). The wave incident from the left is expressed to be e^{ikx} for $k = \sqrt{2mE_x}/\hbar$ (E_x : total energy of the tunneling particle in the x direction, m: the effective mass) and it decays in an exponential form, $e^{-\kappa x}$ for $\kappa = \sqrt{2m(\phi(x) - E_x)}$ ($\phi(x)$: the barrier potential), inside the barrier. And, the wave penetrated to the right is Te^{iqx} . The transmission coefficient, D, is a ratio of the probability flux transmitted through the barrier to the probability flux incident upon the barrier. For an extremely small transmission [33], D can be reduced to be

$$D(E_x) = g e^{-2K},$$

where $g = \frac{16kq\kappa^2}{(k^2 + \kappa^2)(q^2 + \kappa^2)}$ and $K = \int_0^t \kappa(x, E_x) dx$. Notice that D is a function of both barrier height and thickness.

If we apply a voltage on this M-I-M junction, the Fermi levels of the two electrodes originally aligned will be shifted. The chemical potential in Metal 2 is lowered by eV by considering the schematic circuit in Fig. 2.1 (a). For $eV \gg k_B T$, the current density flow from Metal 1 to Metal 2 can be expressed as [33]

$$\begin{aligned} J_{1,2}(V) &= -\frac{2e}{(2\pi)^3} \int_{k_x} \int_{k_y} \int_{k_z} dk_x dk_y dk_z v_x D(E_x, V) f(E) (1 - f(E + eV)) \\ &= -\frac{2e}{(2\pi)^3 \hbar} \int_{E_x} \int_{k_y} \int_{k_z} dE_x dk_y dk_z D(E_x, V) f(E) (1 - f(E + eV)) \text{ for } v_x = \frac{1}{\hbar} \frac{dE}{dk_x} \end{aligned}$$

where f is the Fermi-Dirac distribution for $f_1 = \frac{1}{1+e^{\frac{E-\mu_1}{k_B T}}} = f(E)$ and $f_2 = \frac{1}{1+e^{\frac{E-(\mu_1-eV)}{k_B T}}} = f(E+eV)$. k_y and k_z are symmetric, and we express $\frac{dk_y dk_z}{(2\pi)^2} = \rho_r dE_r$ for ρ_r and E_r are the DOSs and the energy in the y-z plane. Therefore,

$$J_{1,2}(V) = -\frac{2e\rho_t}{h} \int_{E_x} \int_{E_r} dE_x dE_r D(E_x, V) f(E)(1 - f(E + eV)),$$

Similarly, from Metal 2 to Metal 1,

$$J_{2,1}(V) = -\frac{2e\rho_t}{h} \int_{E_x} \int_{E_r} dE_x dE_r D(E_x, V) f(E - eV)(1 - f(E))$$

Then, the net current density would be

$$\begin{aligned} J &= J_{2,1}(V) - J_{1,2}(V) \\ &= -\frac{2e\rho_t}{h} \int_{E_x} \int_{E_r} dE_x dE_r D(E_x, V) [f(E) - f(E + eV)] \end{aligned}$$

For $T \rightarrow 0$ K, all electron stay below the Fermi energy, hence, the tunnel only involve the electrons of energy within the transport window opened by eV , so

$$J = -\frac{2e\rho_t}{h} \int_{E_x} \int_{E_r} dE_x dE_r D(E_x, V)$$

(a)

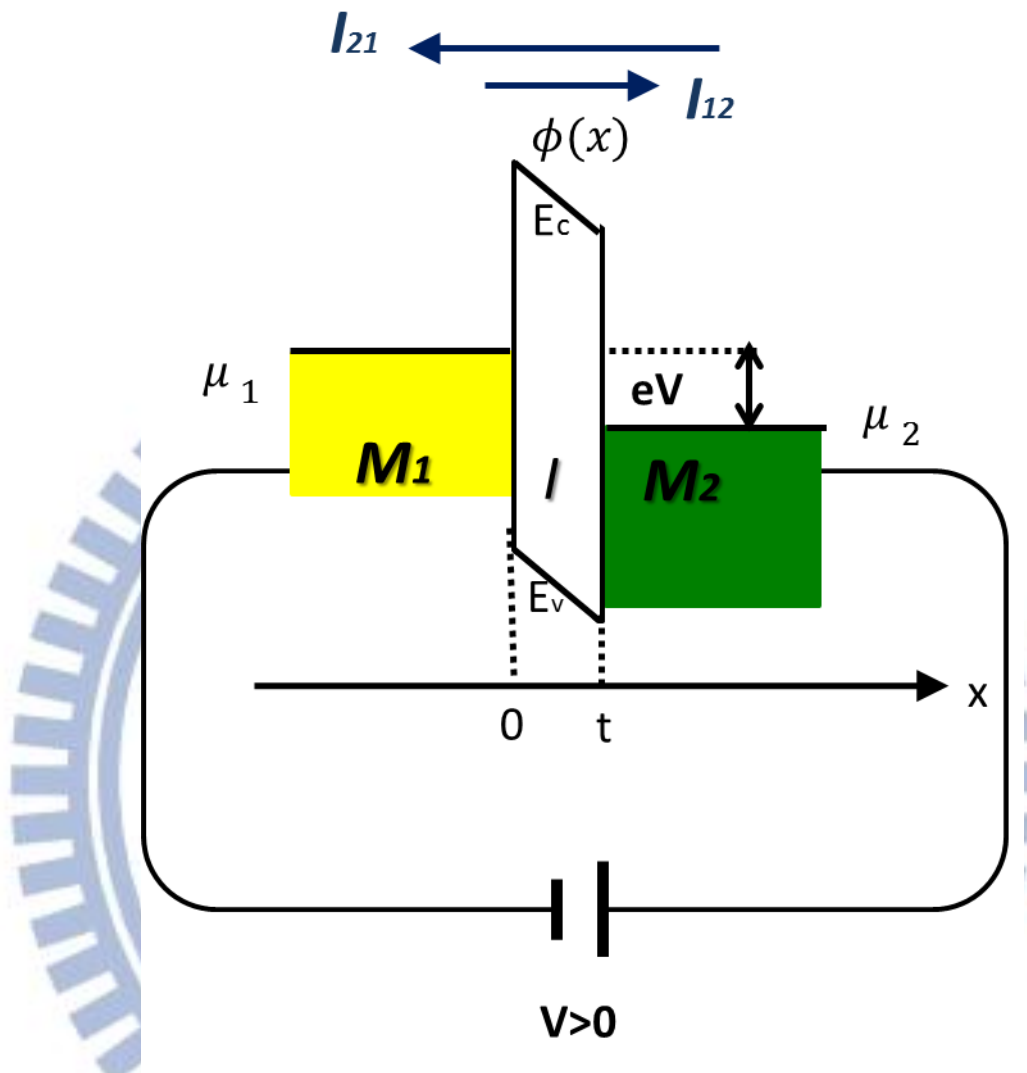


Fig. 2.1 (a) The schematic energy diagram of a metal-insulator-metal (M_1 -I- M_2) tunnel junction with a finite bias V . $\phi(x)$ describes the barrier potential. The net tunneling current flow through the junction should be the summation of current from left to right and that from right to left, i.e. $I = I_{12} + I_{21}$.

2.2 The BDR Model

-- the Background Tunneling Conductance in the Metal-Insulator-Metal Tunnel Junction

Figure 2.2 (a) shows the schematic energy diagram in a metal-insulator-metal tunnel junction. As such a structure is made, the Fermi energies of two metals become equal after the system reaches the equilibrium, and the barrier is asymmetric due to the different work function in the metals. That is, the barrier height seen from two electrodes is different, i.e. ϕ_1 for Metal 1 and ϕ_2 for Metal 2 as showed.

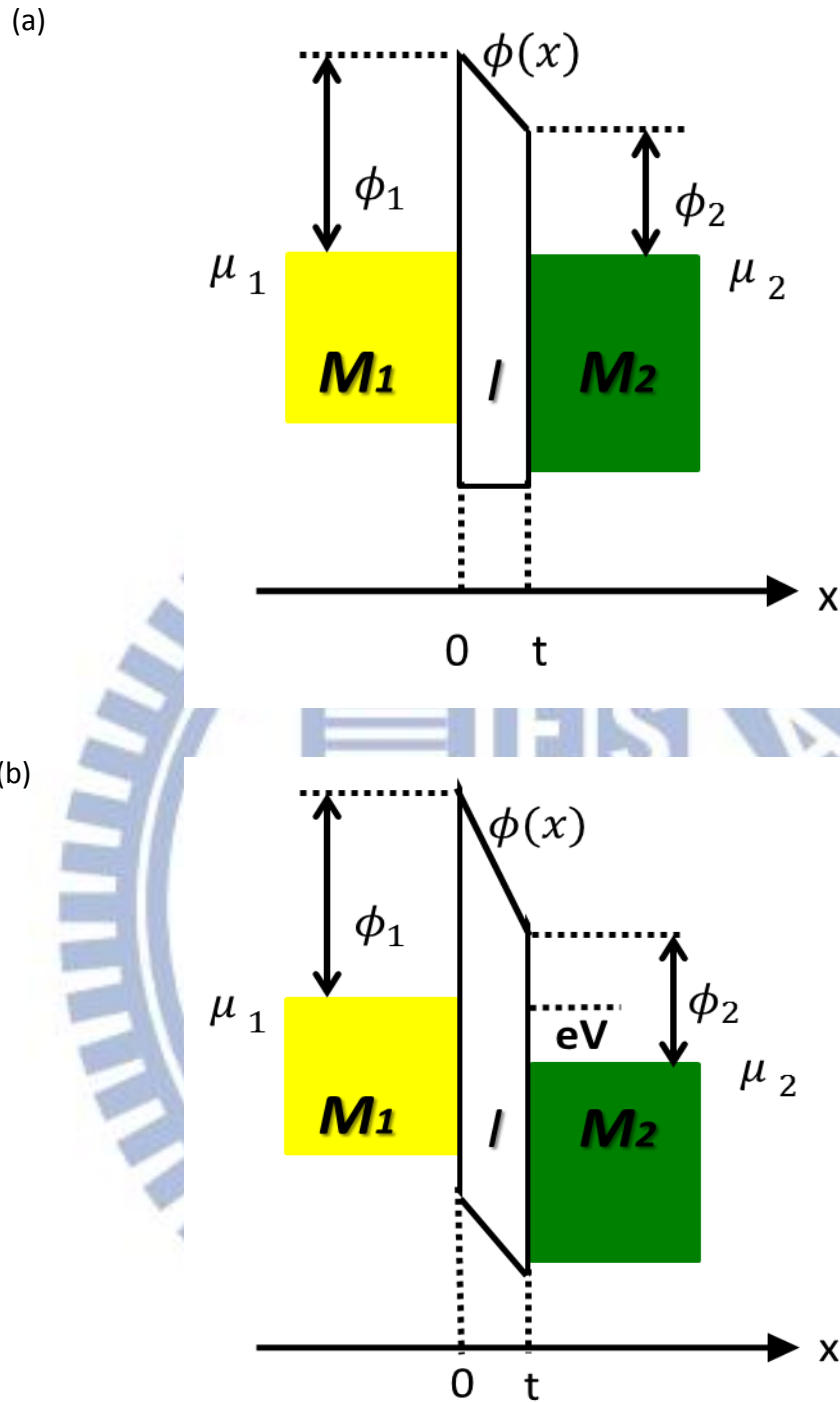
In order to see how the voltage bias affects the tunneling behavior in this tunnel junction, Brinkaman, Dynes and Rowell [34] (BDR model) describe the asymmetric barrier height in a simple form (corresponding to Fig. 2.2 (b)):

$$\phi(x, V) = \phi_1 + \frac{x}{t}(\phi_2 - eV - \phi_1)$$

where t is the barrier thickness. And, we can calculate the differential conductance $G(V) = \frac{\partial J(V)}{\partial V}$ by integrating $D(E_x, V)$ with $\phi(x, V)$ to have $J(V)$. At the low bias,

$$G(V) = G(0) \left[1 - \left(\frac{A_0 \Delta \phi}{16 \bar{\phi}^3} \right) eV + \left(\frac{9 A_0^2}{128 \bar{\phi}} \right) (eV)^2 \right]$$

for $G(0)$, the zero-bias conductce, $A_0 = \frac{4(2m)^{1/2}t}{3\hbar}$, $\Delta\phi = \phi_2 - \phi_1$ and $\bar{\phi} = \frac{\phi_1 + \phi_2}{2}$. The $G(V)$ depends on the bias approximately in a parabolic form under the BDR model, and we notice that the minimum value takes place at the zero bias for $\Delta\phi = 0$ or when the barrier is symmetric.



Figs. 2.2 (a-b) The schematic energy diagram of a metal-insulator-metal (M_1 -I- M_2) tunnel junction with (a) zero-bias (b) a finite bias V . Under BDR model, the potential of the barrier $\phi(x)$ can be described to be $\phi(x, V) = \phi_1 + \frac{x}{t}(\phi_2 - eV - \phi_1)$ (so that) $\phi(x, 0) = \phi_1 + \frac{x}{t}(\phi_2 - \phi_1)$ for (a) the zero-bias.

2.3 The Electron-Electron Interaction in Disorder System

The electron-electron interaction (EEI) and weak localization effects in disordered systems have been studied for decades [9-13, 35]. Although both the two effects contribute significantly to the electrical conduction properties of a given system, it is possible to understand the individual contribution. Indeed, the EEI effect can be isolated by studying the differential conductances, $G(V, T) = dI(V, T)/dV$, of a metal-insulator-metal tunnel junction at low temperatures. Here the (left) reference electrode is made of a clean metal while the (right) electrode is often made of a weakly disordered metal to be investigated.

According to Altshuler and coworkers [9-13], the EEI effect in the presence of weak disorder will lead to suppression in the electron density of states (DOS) near the Fermi level. Moreover, such a DOS singularity is predicted to be sensitive to both bias voltage and temperature. At a low temperature (to ignore the thermal smearing effect), and at the weak-disorder limit, i.e., $k_F \ell \gg 1$, where k_F is the Fermi wavenumber and ℓ is the elastic mean free path of electrons, the EEI-induced correction to the DOS, $\delta N_d(E)$, depends strongly on the effective dimensionality d of the sample and has the following forms:

for $d = 2$, the correction is given by [9, 11, 12]

$$\frac{\delta N_2(E)}{N_2(0)} = \frac{\lambda_2 e^2}{8\pi^2 \hbar} R_{\square} \ln \left[\frac{E}{\hbar D} \left(\frac{t}{2\pi} \right)^2 \right]$$

where λ_2 depends on the form of the effective EEI and for long range Coulomb interactions [5]

$$\lambda_2 = \ln \left[\frac{\hbar D \kappa_2^4 t^2}{(2\pi)^2 E} \right]$$

with $\kappa_2 = \frac{me^2k_F t}{2\pi^2\hbar^2\epsilon_0}$, where ϵ_0 is the permittivity of the vacuum.

for $d = 3$, the correction is given by [5, 13]

$$\frac{\delta N_3(E)}{N_3(0)} = \frac{\lambda_{3\sqrt{E}}}{4\sqrt{2}\pi^2(\hbar D)^{3/2}N_3(0)}$$

Here $N_2(0)$ and $N_3(0)$ are the DOS at Fermi level in the $d = 2$ and $d = 3$ case respectively, R_{\square} is the sheet resistance, D is the diffusion constant, t is the film thickness, and τ is the electron momentum relaxation time. The electron energy E is measured relative to the Fermi energy. Besides, the theory predicts that a crossover from two to three dimensions should occur at a characteristic bias energy $eV_c = E_c \approx (2\pi)^2(\hbar D/t^2)$. This critical energy corresponds to an EEI characteristic length of $L_c = \sqrt{\hbar D/E_c} \approx t/2\pi$. Notice that the characteristic bias voltage V_c scales with D/t^2 , and hence it reduces with increasing disorder.

For a metal-insulator-metal tunnel junction comprised of a clean metal and a disordered metal, at low temperatures, the variation in the differential conductance $G(V)$ directly reflects the energy dependence of DOS of the disordered metal [33]: $G(V) = PN_c(0)N_d(eV)$, where P is the tunneling rate which depends on the barrier properties (barrier height and thickness), N_c is the DOS of the clean metal which depends weakly on energy and can be approximated as the value at Fermi level $N_c(0)$, and N_d is the DOS of the disordered metal. Thus, the normalized conductance $G(V)/G(0) = N_d(eV)/N_d(0)$ can be compared with $\frac{\delta N_2(E)}{N_2(0)}$ and $\frac{\delta N_3(E)}{N_3(0)}$ to study the DOS suppression in disordered metals quantitatively. In particular, $G(V)$ obeys a $\ln V$ law in two dimensions, while it obeys a \sqrt{V} law in three dimensions.

Experimentally, from measurements of the $G(V, T)$ of metal-insulator-metal tunnel

junctions, the DOS singularities have been investigated by several groups. Both weakly [36-41] and strongly [15, 16, 42] disordered metal electrodes have been employed. In recent years, the EEI theory has further been critically tested by high-resolution photoemission spectroscopy measurements [43]. In general, it is found that the EEI theory is fairly successful in explaining the experimentally observed DOS singularities in weakly disordered conductors. In addition, the EEI prediction of a crossover from the two-dimensional $G(V) \propto \ln V$ law [11, 12] to the three-dimensional $G(V) \propto \sqrt{V}$ law [13] as the bias voltage increases has been confirmed by several experiments [36-39, 41] where electrodes of metal films in the tunnel junctions were used.

2.4 Theoretical Prediction for Granular Electronic Systems

Granular conductors, which are composite materials of metallic granules and dielectric components, have recently attracted much renewed theoretical attention as tunable systems for addressing mesoscopic physics problems [25, 26]. In contrast to disordered “homogeneous systems”, the electronic transport properties of granular conductors are largely governed by the strength of the intergrain tunneling [25]. Theoretically, a granular conductor is characterized by a number of physical quantities: the mean energy level spacing in a single granule, δ , the dimensionless tunneling conductance between neighboring granules, g (i.e., the average tunneling conductance between neighboring grains expressed in units of $2e^2/h$), and the single-grain Coulomb charging energy, E_c . For strong intergrain coupling ($g \gg 1$) and in the not-too-low temperature interval $g \ll k_B T \ll E_c$ (where k_B is the Boltzmann constant), charging effects are important yet the quantum-interference weak-localization (WL) effects are suppressed. This unique regime provides a tempting

opportunity to probe the electronic conduction properties due to the many-body Coulomb interaction effects in the presence of granularity. The electrical *conductivity* σ is predicted to obey the law [26, 44]

$$\sigma(T) = \sigma(0) \left[1 - \frac{1}{2\pi g d} \ln \left(\frac{gEc}{k_B T} \right) \right]$$

where d is the dimensionality of the granular array, and $\sigma(0) = 2(e^2/h)ga^{2-d}$ is the classical conductivity without the Coulomb interaction (i.e., the system conductivity at temperature $k_B T \gg Ec$), and a is the radius of the (spherical) grain. It is important to note that, unlike that due to the WL and electron-electron interaction (EEI) effects in weakly disordered homogeneous systems [9], this $\sigma \propto \ln T$ law is predicted to hold for all dimensions, since the dimensionality d only enters the prefactor of the logarithmic correction term. On contrary, the functional form of the tunneling electronic density of states (DOS) is predicted to depend critically on sample dimensionality:

for $d = 3$ [26, 44],

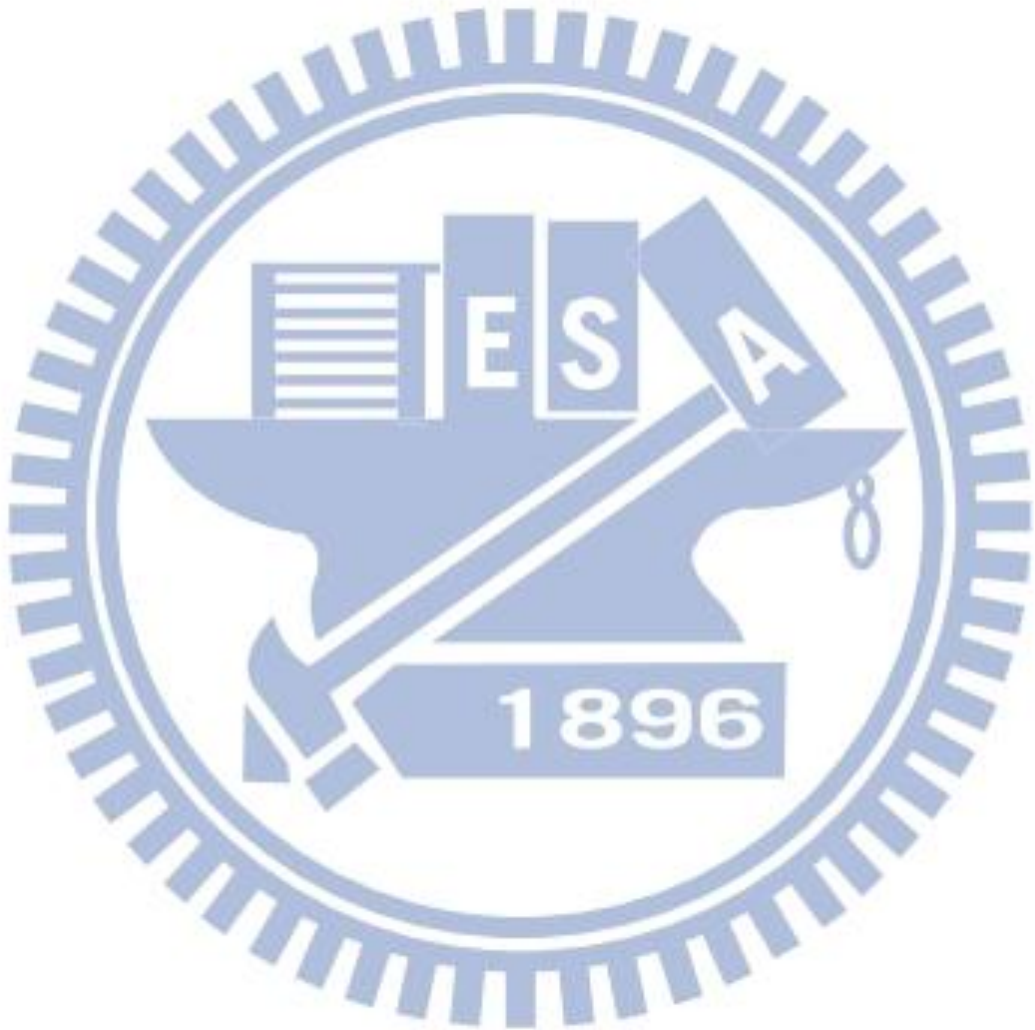
$$v_3(\epsilon) = v_0 \left[1 - \frac{A}{4\pi g} \ln \left(\frac{gEc}{\max(k_B T, \epsilon)} \right) \right]$$

where ϵ is the tunneling electron energy measured from the Fermi energy level (E_F), v_0 is the DOS in the absence of Coulomb interaction, and A is a numerical prefactor;

for $d = 2$

$$v_2(\epsilon) = v_0 \exp \left[- \frac{1}{16\pi^2 g} \ln^2 \left(\frac{gEc}{\max(k_B T, \epsilon)} \right) \right]$$

The underlying physics which leads to the conductivity and DOS corrections is due to the presence of local voltage fluctuations between neighboring granules.



Chapter 3

Experimental Method

3.1 Sample Fabrication

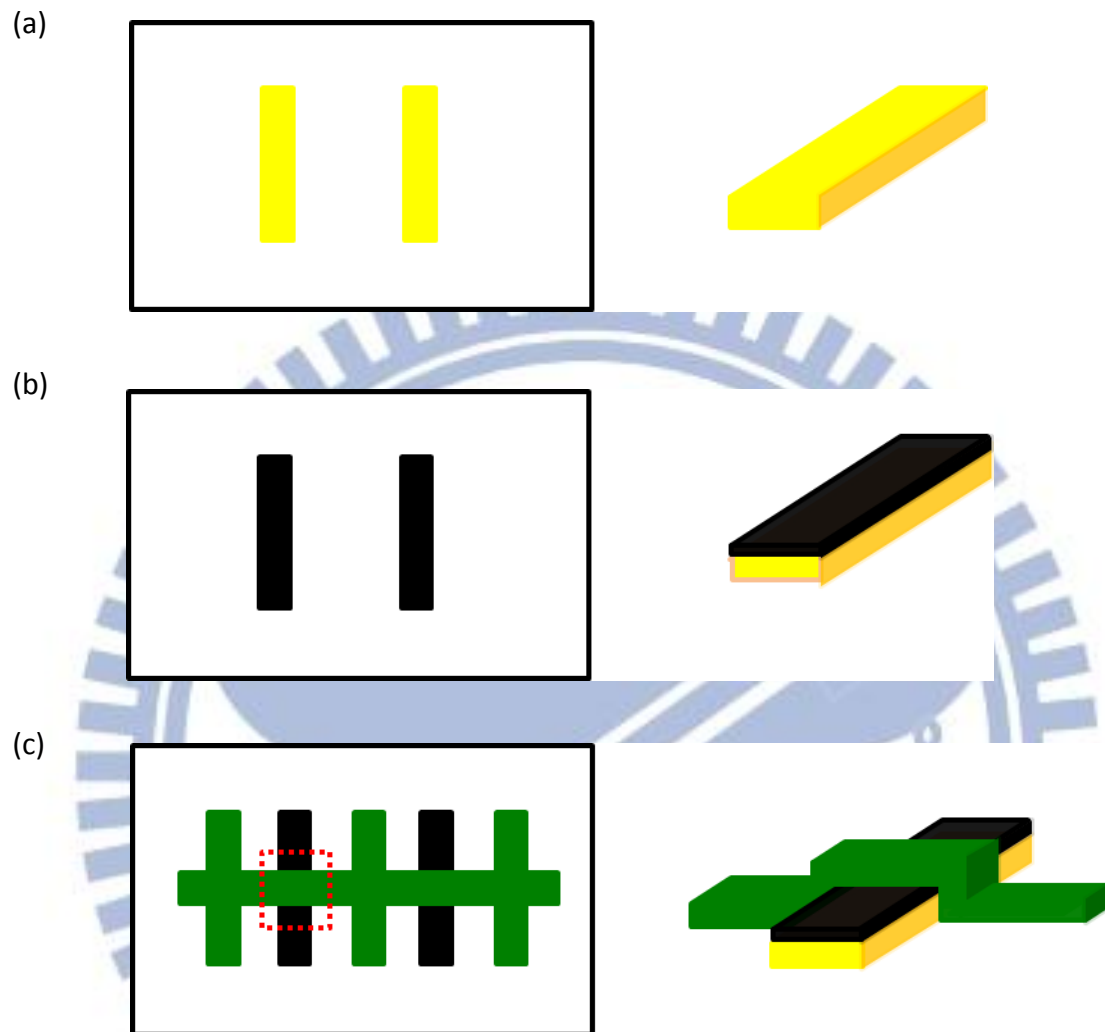
To study the conductivity and the tunneling DOS of granular Cr films, we fabricated four Al/AlO_x/Cr planar tunnel junctions by using the standard thermal evaporation method:

1. First, a set of parallel, relatively clean 0.8 or 1 mm wide and 25 nm thick Al films were deposited on glass substrates held at room temperature.
2. Then, surfaces of the as-deposited Al films were subsequently oxidized by utilizing plasma discharge to produce a \approx 1.5–2 nm – thick AlO_x layer.
3. Finally, a long Cr electrode (1 mm wide, and 15–30 nm thick) was then deposited across the parallel AlO_x coated Al strips to complete the tunnel junction geometries. At the same time, the Cr electrode was attached with leads appropriate for four-probe electrical measurements.

Figures 3.1 (a-c) show the schematic diagrams of our sample during the steps described

above. The resistivities of our Al reference electrodes were typically 13 (16) $\mu\Omega$ cm at 4 (300) K, corresponding to the product $k_F \ell \approx 54$ at 4 K, where k_F is the Fermi wavenumber and ℓ is the electron mean free path. The conductivity of the Cr electrode in each set of junctions was adjusted by varying the mean Cr film thickness and the deposition rate between 0.01 and 1.5 nm/s. To achieve a very low conductivity in the junction D, the Cr film was deposited onto a cold substrate held at liquid-nitrogen temperature, by employing a very low deposition rate of ~ 0.01 nm/s.

The reason for selecting Cr as our electrode is because Cr films deposited in a vacuum often form granular, rather than uniform and continuous, layers [6-8]. For example, a 10 – nm – thick Cr film deposited by thermal evaporation on a mica substrate showed a distribution of disk-shaped granules with a diameter of \sim a few tens of nanometer and a height of ≈ 2 –6 nm, as was evidenced from atomic force microscopy (AFM) studies (see Fig. 3.1 (d) [6]). Varying the deposition rate modified the average grain size [6]. Even thermally evaporated in a vacuum having a background pressure as low as $\sim 1 \times 10^{-6}$ mbar, the surfaces of Cr granules became oxidized and formed thin dielectric layers of CrOx [8]. In this work, we carried out our thermal evaporation deposition at a pressure of $\sim 5 \times 10^{-6}$ mbar so that our films were guaranteed to form metallic Cr granules separated by thin CrOx dielectric layers. Table 1 lists the values for the relevant parameters of the four Cr electrodes comprising the tunnel junctions A – D studied in this work.



Figs. 3.1 (a-c) Schematic diagrams of the top views (left) and side views (right) of our sample during the fabrication progresses: (a) The evaporated Al film; (b) Utilizing O_2 plasma to oxidize the surface of the deposited Al film; (c) Depositing Cr film to cross the AlO_x/Al structure. The side view shows the junction area where the red dotted lines enclose on the left top view figure.

(d)

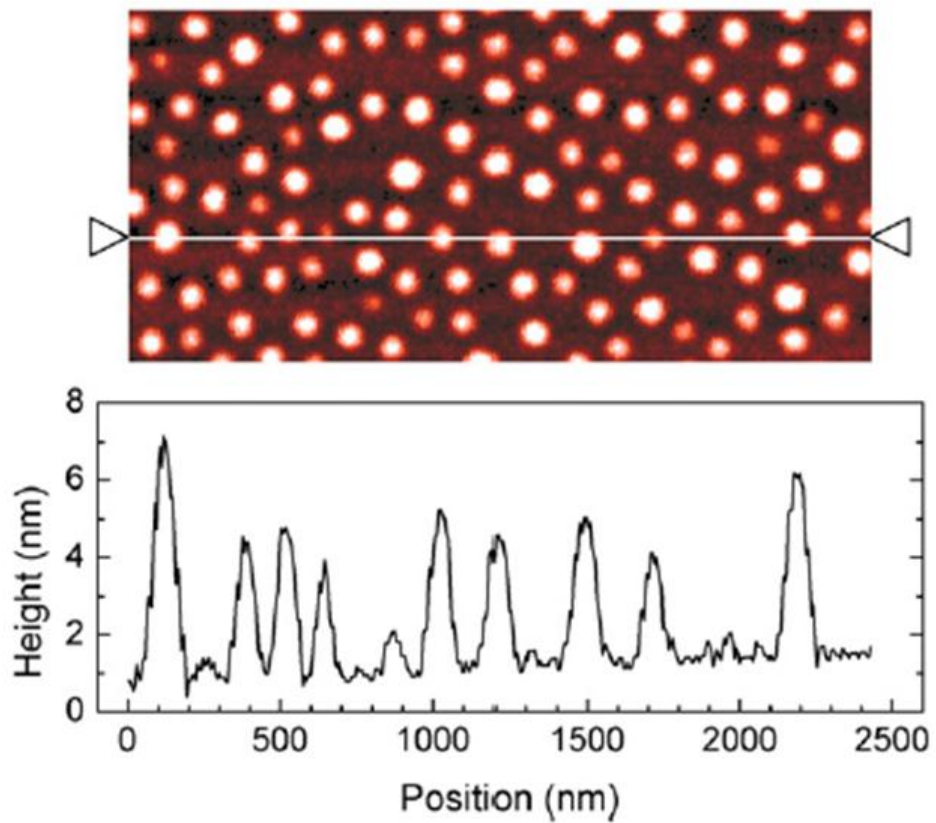


Fig. 3.1 (d) The AFM image of a thin Cr layer, prepared by thermal evaporation deposition on a mica substrate, shows the granular property. The surface profile below is along the solid line indicated in the AFM image [6].

Table 1 Values for relevant parameters of the Cr electrodes in Al/AlOx/Cr tunnel junctions. A_J is the junction area and R_J is the junction resistance at 300 K. t is the thickness, ρ (R_{\square}) is the resistivity (sheet resistance) at 2.5 K, and $N_{cr,d}(0)$ is the DOS at the Fermi energy. $k_F \ell$ was calculated by using the Drude model. The diffusion constant D was evaluated through the Einstein relation $\rho^{-1} = N_{cr,d}(0)e^2D$. The values of $k_F \ell$ and D were evaluated for 2.5 K. E_c, σ_0, g and a are defined in Sec. 2.4. Notice that the values of a are only listed for reference, because our Cr granules are disk-shaped rather than spherical.

Sample	A_J	R_J	t	ρ	R_{\square}	$N_{cr,d}(0)$
	(mm ²)	(k Ω)	(nm)	($\mu\Omega - \text{cm}$)	(Ω)	(J ⁻¹ m ⁻³)
A	0.8 × 1.0	1.0	30	115	38.3	2.4 × 10 ⁴⁷
B	0.8 × 1.0	4.5	25	154	61.6	1.8 × 10 ⁴⁷
C	1.0 × 1.0	11	15	290	193	1.1 × 10 ⁴⁷
D	0.8 × 1.0	4.0	25	5060	2024	2.8 × 10 ⁴⁶

Sample	$k_F \ell$	D	E_c	σ_0	g	a
		(cm ² /s)	(meV)	($\Omega^{-1} \text{cm}^{-1}$)		(nm)
A	5.1	1.4	5	8690	62	5.5
B	4.1	1.4	7	6560	42	5.0
C	2.6	1.3	4	3500	10	2.2
D	0.23	0.28	22	260	0.96	2.8

3.2 Experimental Methods

In our experiments, we measured the resistivity of Cr films with the four-probe method, while the tunneling differential conductances, $G(V, T) = dI(V, T)/dV$, across the junctions were measured by utilizing the standard lock-in technique, where I is the tunneling current between the Al and Cr electrodes, and V is the voltage dropped across the insulating barrier (see Fig. 3.2 (a) for a schematic diagram). Figure 3.2 (b) shows the equivalent circuit of measuring the differential conductance to have the DOS of Cr (see Sec. 2.1).

To ensure the quality of each tunnel junction, we measured the superconducting gap of the clean Al electrode at 0.25 K before performing detailed measurements of $G(V, T)$ curves. Our Al electrodes became superconducting at $\approx 1.8 - 2$ K, and Fig. 3.2 (c) shows one of the results in Sample D. Due to the great change of the superconducting gap in the differential conductance, the experiment, different from measurement for the $G(V) = dI(V)/dV$ of Cr electrodes, is performed by applying V to measure I . The equivalent circuit is in Fig. 3.2 (d).

(a)

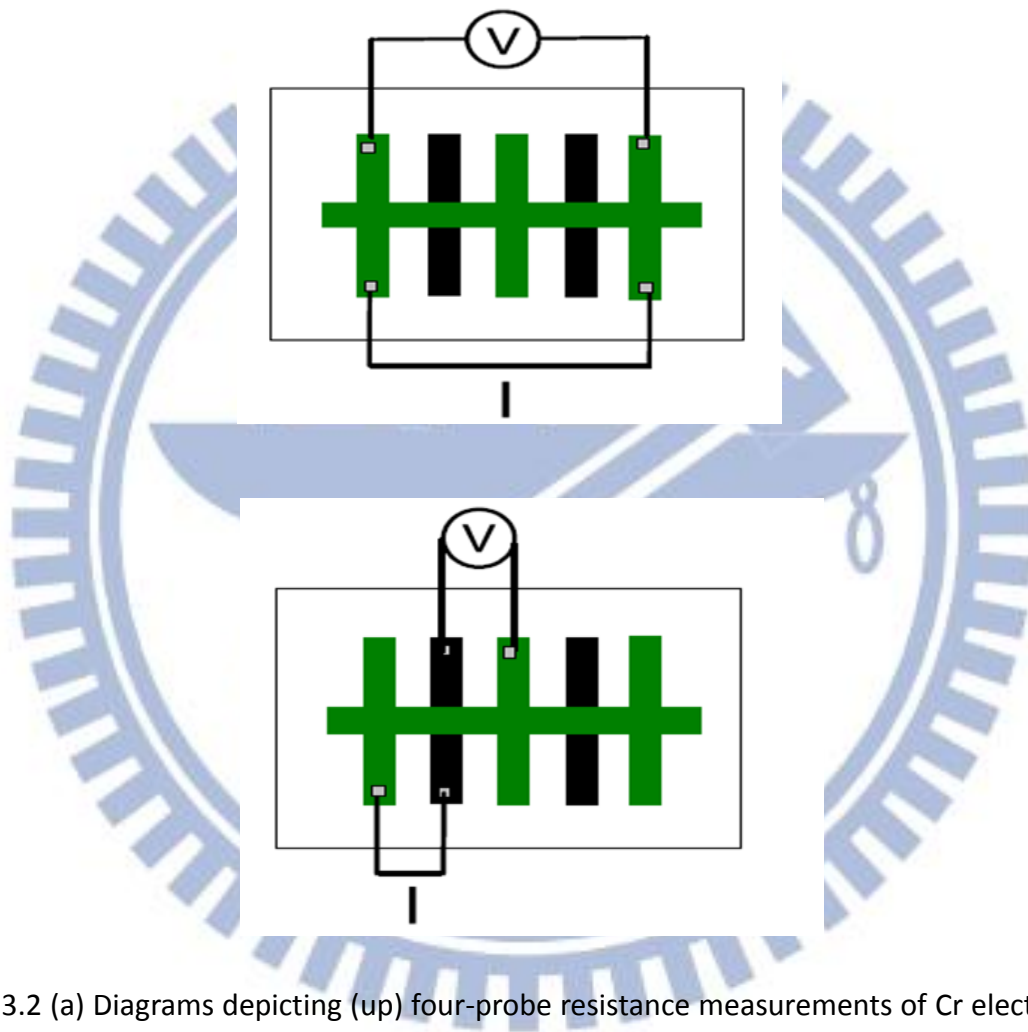


Fig. 3.2 (a) Diagrams depicting (up) four-probe resistance measurements of Cr electrodes, and (down) differential conductance measurements of Al/AIO_x/Cr tunnel junctions. Black strips stand for Al films, and green (gray) strips for Cr electrodes.

(b)

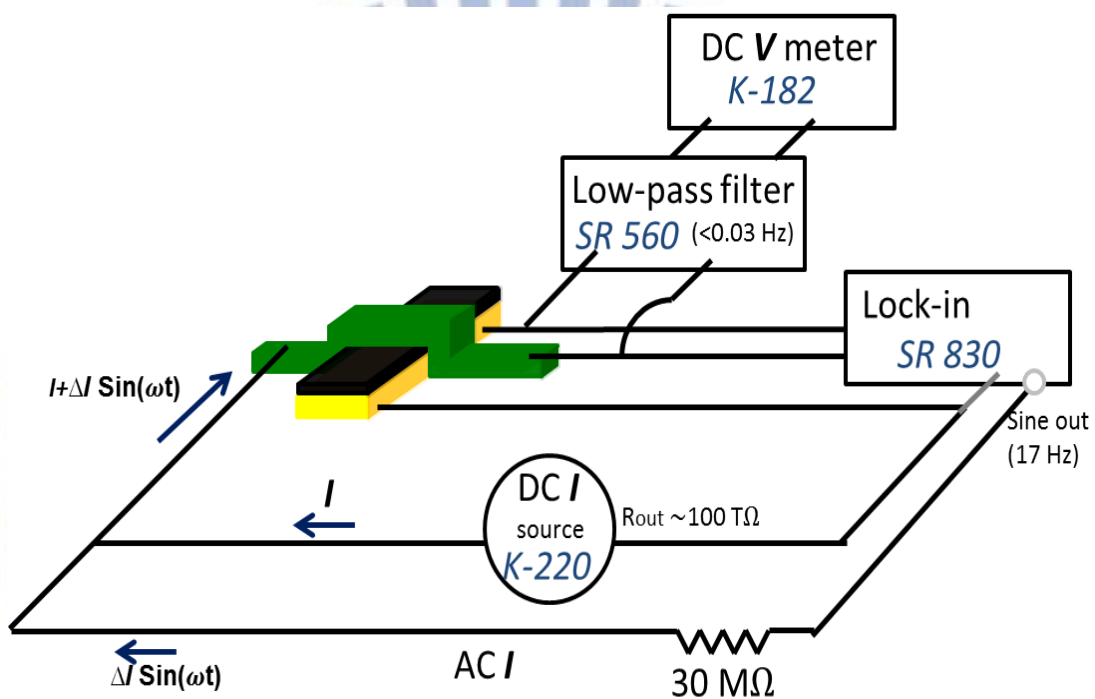


Fig. 3.2 (b) The equivalent circuit for the differential conductance measurements for Cr electrodes.

(c)

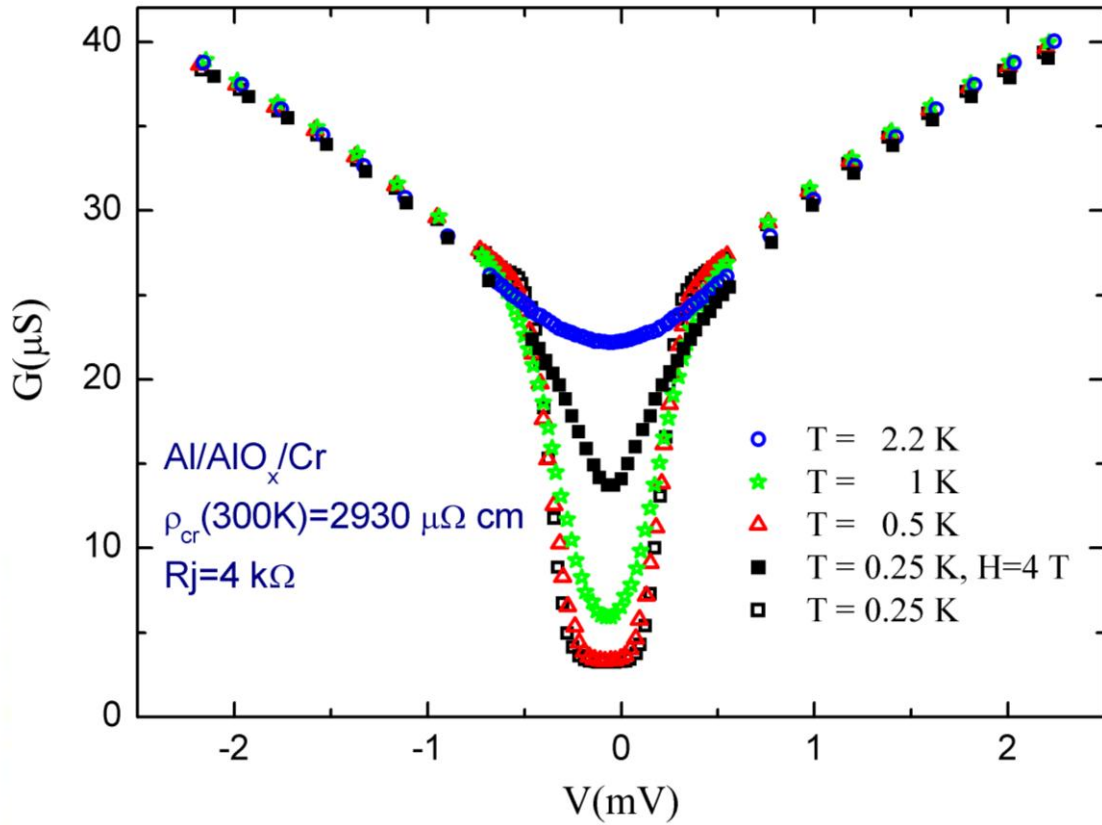


Fig. 3.2 (c) The differential conductance measurement of the most disordered Cr electrode, sample D, at temperature $T = 0.25, 0.5, 1, 2.2 \text{ K}$ where the Al electrode has already been superconducting. The barrier quantity can be tested and verified by the signature of the superconducting gap, since $G(V) = dI(V)/dV$ is a function of $N_{\text{Cr}}(V)$ and $N_{\text{Al}}(V)$. The measured result reveals the superconducting gap at $T = 0.25 \text{ K}$ is $\lesssim 0.5 \text{ meV}$, while the calculated energy gap for Al being superconducting at 1.14 K is 0.34 meV . The data (■) shows the superconductivity is destroyed by the applied magnetic field.

(d)

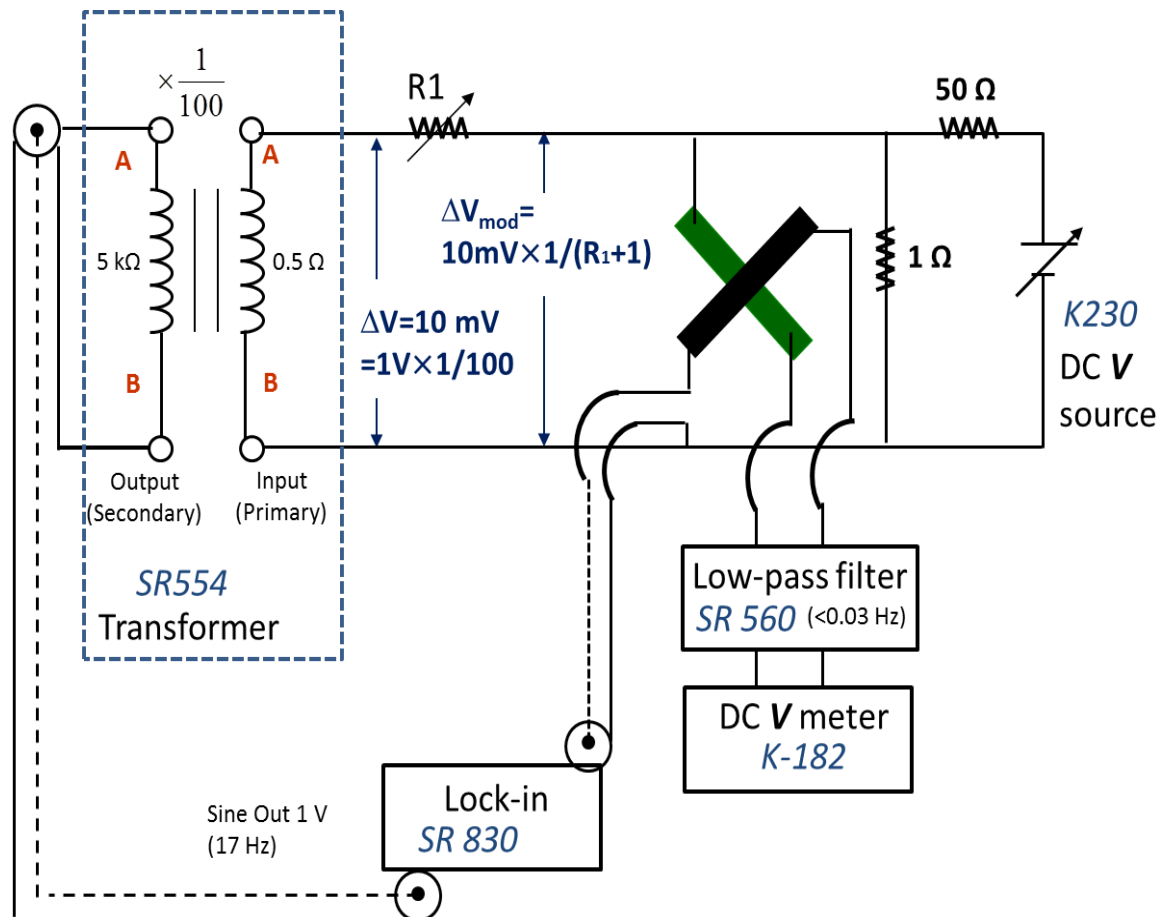


Fig. 3.2 (d) The equivalent circuit of the $G(V) = dI(V)/dV$ measurements for the superconductor energy gap. Due to the great and sudden change at the edge limit of the gap, we send V to measure I in contrary to Fig. 3.2 (b).

3.3 Experimental Setups

In our experiments, we measured and the DOS of Cr electrodes under low temperature with ^3He cryostats (see Fig. 3.3 (a)) which will be introduced together with the superconducting magnet (Fig. 3.3 (b)) in this section.

Before starting to cool down our system, we first launch our sample on the sample holder just below ^3He pot, and then seal the parts below IVC (inner vacuum chamber) flange with an IVC shell. After pumping out the air inside IVC space (to be vacuum), we put some ^4He gas utilized to be exchange gas. There are three stages to cool the system:

1. From room temperature to 4.2K

The cryostats first puts into the LN_2 for pre-cooling until $T \sim 80$ K. Then move the cryostats into LHe_4 to be $T \sim 4.2$ K. During this stage, there are only a few exchange gases inside the IVC shell, therefore the temperature will not go down too quickly.

2. From 4.2 K to 1.8 K

At this stage, we lower the temperature by lowering the pressure above the LHe_4 less than 1 atm. In Fig. 3.3 (a), 1.5 K condenser is above ^3He pot. We pump the LHe_4 in and out of a small tube attached or connected to the 1.5 K condenser with different pumping rates, so that the temperature can be decreased to be ~ 1.5 K as the pressure is lower. Through the thermal contact (from 1.5 K condenser to the sample holder), the sample can be cooled down.

3. From 1.8 K to 0.3 K

This stage uses the same method in stage 2 but with LHe_3 to cool the system down to 0.3 K. Activated carbon, cable of absorbing the gases, is used as the sorption pump, and

this ability depends on temperature (the higher temperature it is, the larger kinetic energy the gas has, and the poorer ability of the sorption pump to absorb gas). The sorption pump is connected to ^3He pot (which is just above the sample). At beginning, we control the sorb to be $\sim 45\text{ K}$ where ^3He should be gas since its condensation point at 1 atm is $\sim 2.8\text{ K}$. As the system cools to be $\sim 1.8\text{ K}$ at stage 2, ^3He should be condensed to be liquid. If we lower the temperature of the sorb at this time, then it will absorb gas more efficiently, so that the gas pressure in ^3He pot decreases. It leads to the already condensed LHe_3 evaporate! Then the ^3He pot temperature cools down again until reaches the lowest temperature $\sim 0.3\text{ K}$.



(a)



Fig. 3.3 (a) The photo (left) and schematic figure (right) of He^3 cryostats.

Chapter 4

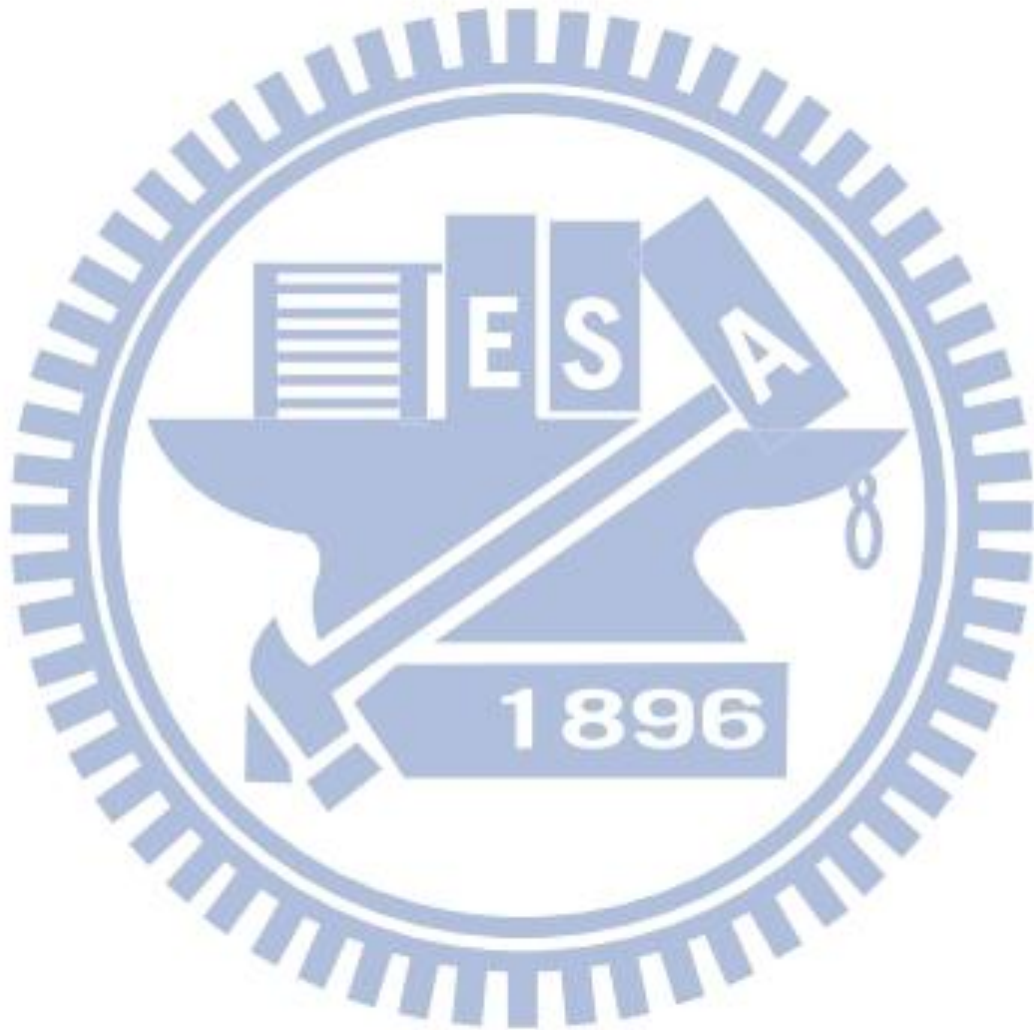
Result and Discussion

In this chapter, we first demonstrate our measured results in Sec. 4.1 *temperature dependence of conductivity curves* and in Sec. 4.2 *temperature dependence of differential conductance curves*. Then we compare our results with available theoretical predictions concerning disordered conductors: In Sec. 4.3, *a comparison with the conventional EEI effect*, originally developed for weakly disordered homogeneous conductors by Altshuler and coworkers [9, 12, 13], is made. Meanwhile, we try to discuss our observations in terms of the recent theory of granular metals, formulated by Efetov and Tschersich [26] and Beloborodov and coworkers [25, 44], in both Sec 4.4 *logarithmic temperature dependence of conductivity* and Sec. 4.5 *differential conductance curves and tunneling density of states*.

4.1 Temperature Dependence of Conductivity Curves

Figure 4.1 (a) shows the variation in normalized resistivity, $\rho(T)/\rho(280\text{ K})$, with temperature for the four Cr electrodes of our tunnel junctions. Except for the junction A, the resistivities of all other samples monotonically increase with decreasing temperature. However, the amounts of the resistivity rise are much smaller than what would be expected for samples falling deep on the insulating side, where resistivity should show

$\rho \propto \exp(\sqrt{T_0/T})$ dependence and rapidly increase with decreasing temperature. This result immediately reflects that the intergrain tunneling conductances g in our Cr electrodes must be large. In particular, a $\ln T$ dependence of the conductivity was found in all Cr electrodes at liquid-helium temperatures, and this $\sigma \propto \ln T$ behavior holds for more than one decade of temperature in the junctions B and D is shown in Fig. 4.1 (b).



(a)

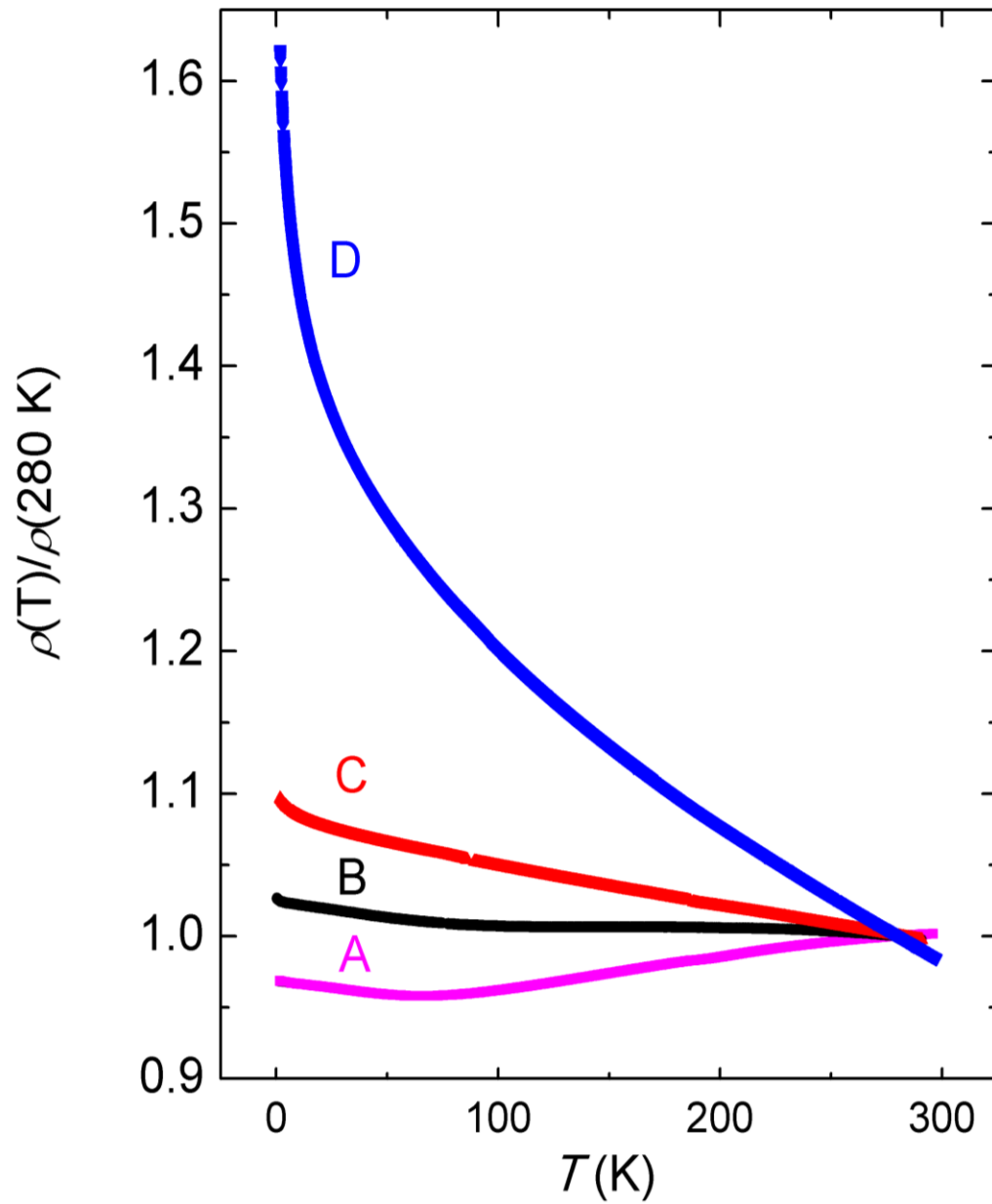


Fig. 4.1 (a) Normalized resistivity, $\rho(T)/\rho(280\text{ K})$, as a function of temperature of the Cr electrodes in junctions A – D, as indicated.

(b)

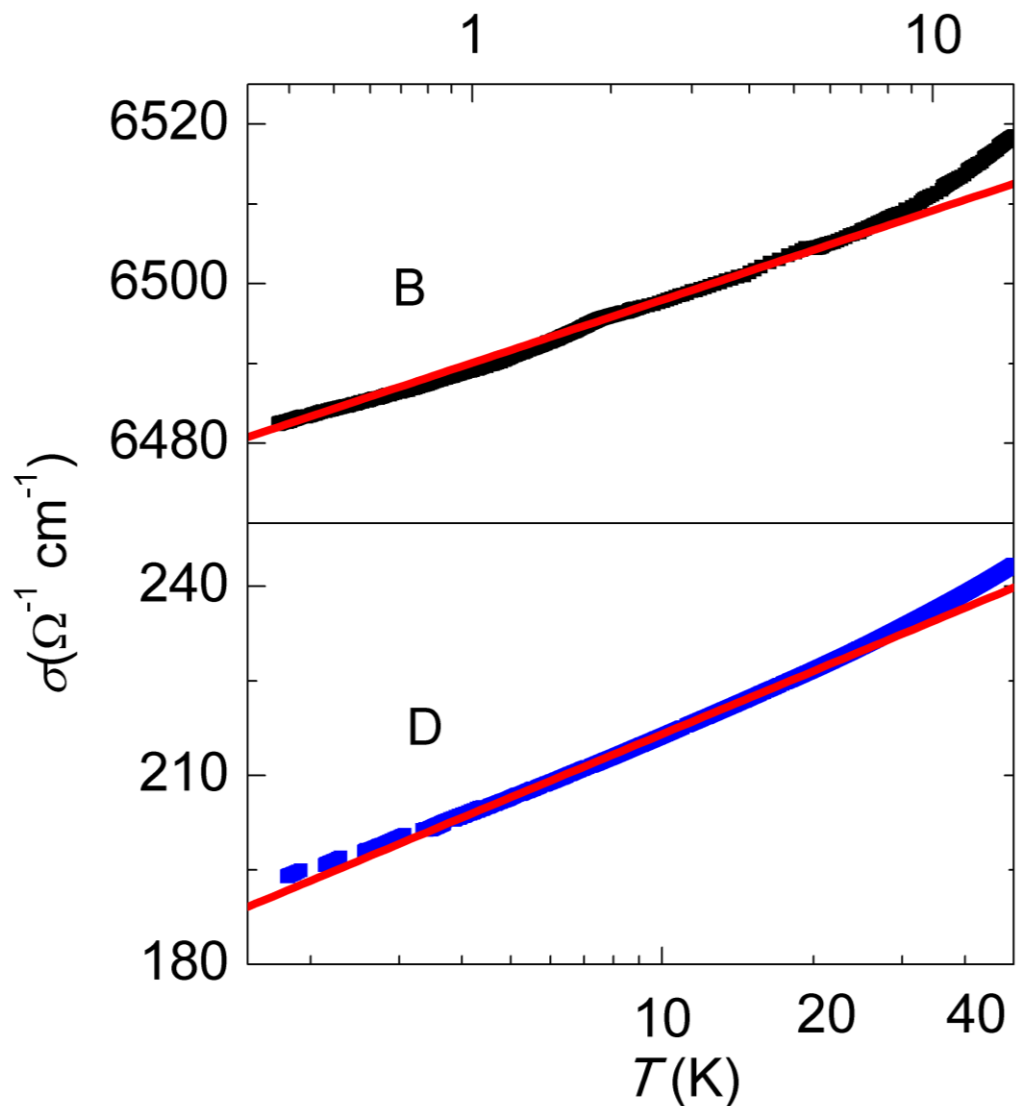


Fig. 4.1 (b) Conductivity as a function of temperature of the Cr electrodes in junction B and junction D. The straight solid lines are least-squares fits to the equation of conductivity in Sec 2.4.

4.2 Temperature Dependence of

Differential Conductance Curves

The normalized differential conductances, $G(V)/G(70 \text{ mV})$, of these tunnel junctions reveal essentially symmetric dips centered at the zero bias voltage as in Fig. 4.2 (a). It is clearly seen that the differential conductance dips are markedly more pronounced in junctions comprised of more disordered Cr electrodes. The relative changes in $G(V)$ at 2.5 K are $[G(0) - G(70 \text{ mV})]/G(70 \text{ mV}) = -0.27, -0.36, \text{ and } -0.89$ in the junctions A, C and D, respectively. These magnitudes of relative change in $G(V)$ are more than one order of magnitude larger than what would be expected from the EEI effect in weakly disordered homogeneous conductors [9].

We further measured the differential conductance curves in external magnetic fields applied perpendicular to the junction plane. Figures 4.2 (b)/(c) shows the $G(V)$ curves of the junction A/ D in zero magnetic field (symbols) and in a magnetic field of 4 T (solid curve). Figures 4.2 (b-c) firmly demonstrate that the magnetic field caused a negligible change ($\approx 0.05\%$) in $G(V)$. A negligible magnetic field effect, together with the strong dependence of the magnitudes of $G(V)$ dips on the level of disorder displayed in Fig. 4.2 (a), strongly suggests that our observed large conductance dips must be associated with some sort of disorder effect in the granular Cr electrodes. In other words, any magnetic origins, which have long been suspected to play an important role in Cr comprised junctions, can be ruled out [1, 5].

Figures 4.2 (d-e) show our voltage-dependent differential conductances of the junctions. At low bias regime ($V \lesssim 10 \text{ mV}$) in junctions A – C, we found that $G(V)/G(10 \text{ mV}) \propto \ln V$ as in Fig. 4.2 (d), the normalized $G(V)/G(10 \text{ mV})$ spectra of the Al/AlO_x/Cr junctions at 2.5 K in the positive bias voltage (recall that our $G(V)$ curves are essentially symmetric around the zero-bias voltage). And, the conductances cross over to the $G(V)/G(10 \text{ mV}) \propto$

\sqrt{V} law at higher bias voltages in Fig. 4.2 (e). Besides, as for the junction D, the $G(V)/G(10\text{ mV}) \propto \sqrt{V}$ law was obeyed from relatively low bias voltages all the way up to a notably high bias voltage of $\sim 100\text{ mV}$ (see the inset of Fig. 4.2 (e)).

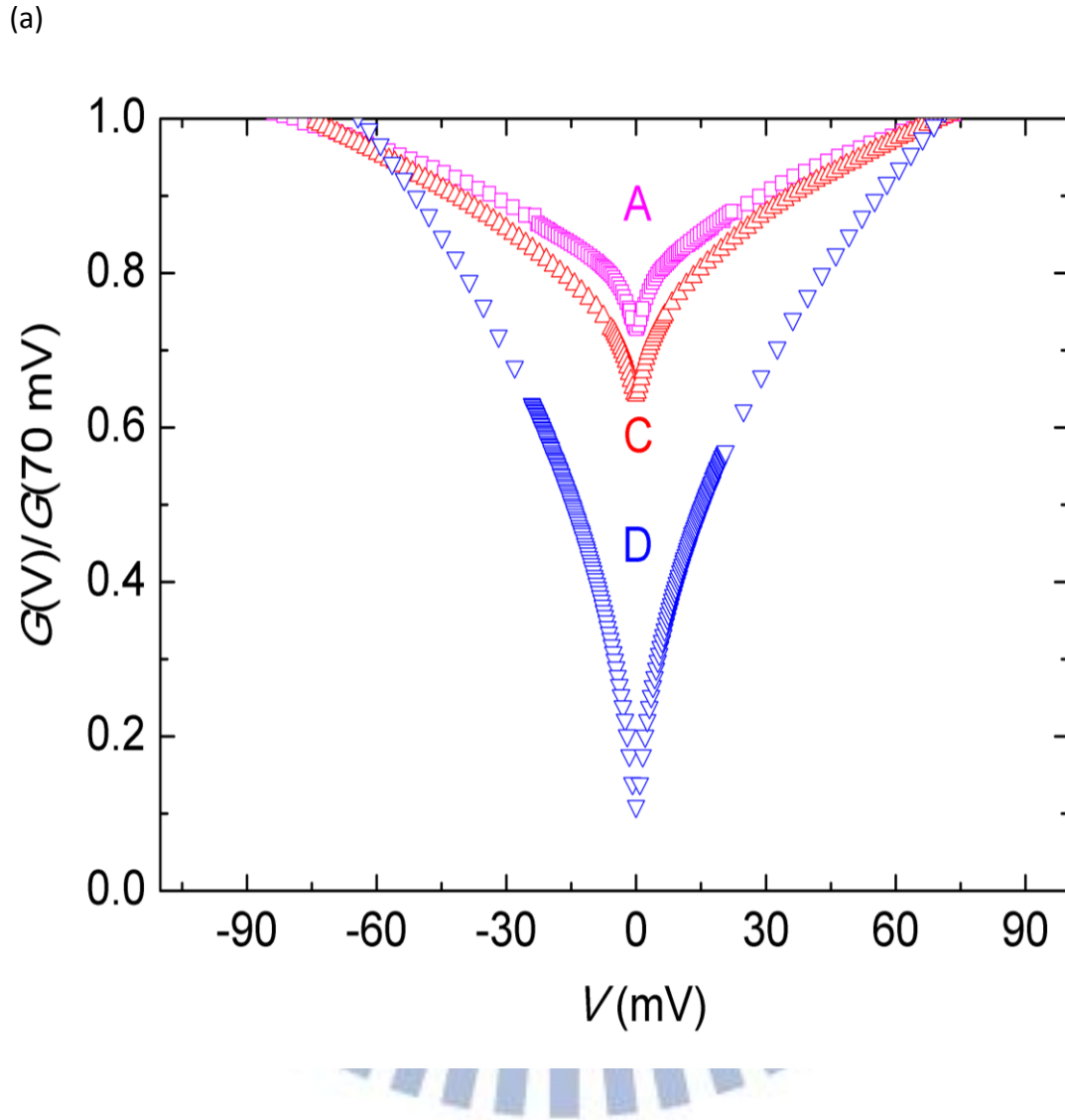


Fig. 4.2 (a) Normalized differential conductance, $G(V)/G(70\text{ mV})$, as a function of bias voltage for junctions A, C and D, as indicated. Notice that the $G(V)$ curves are essentially symmetric around the zero bias voltage. Data were taken at 2.5 K.

(b)

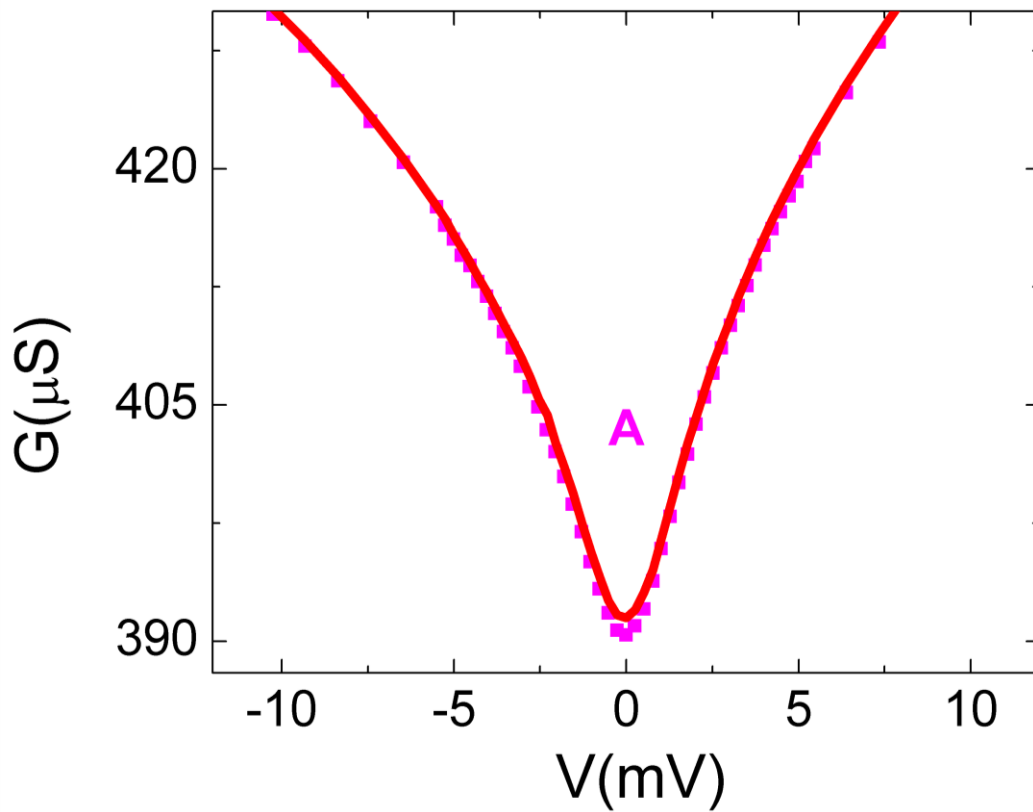


Fig. 4.2 (b) The $G(V)$ curve of junction A in zero magnetic field (symbols) and in a perpendicular magnetic field of 4 T (solid curve). Notice that the magnetic field causes a negligible change. Data were taken at 2.5 K.

(c)

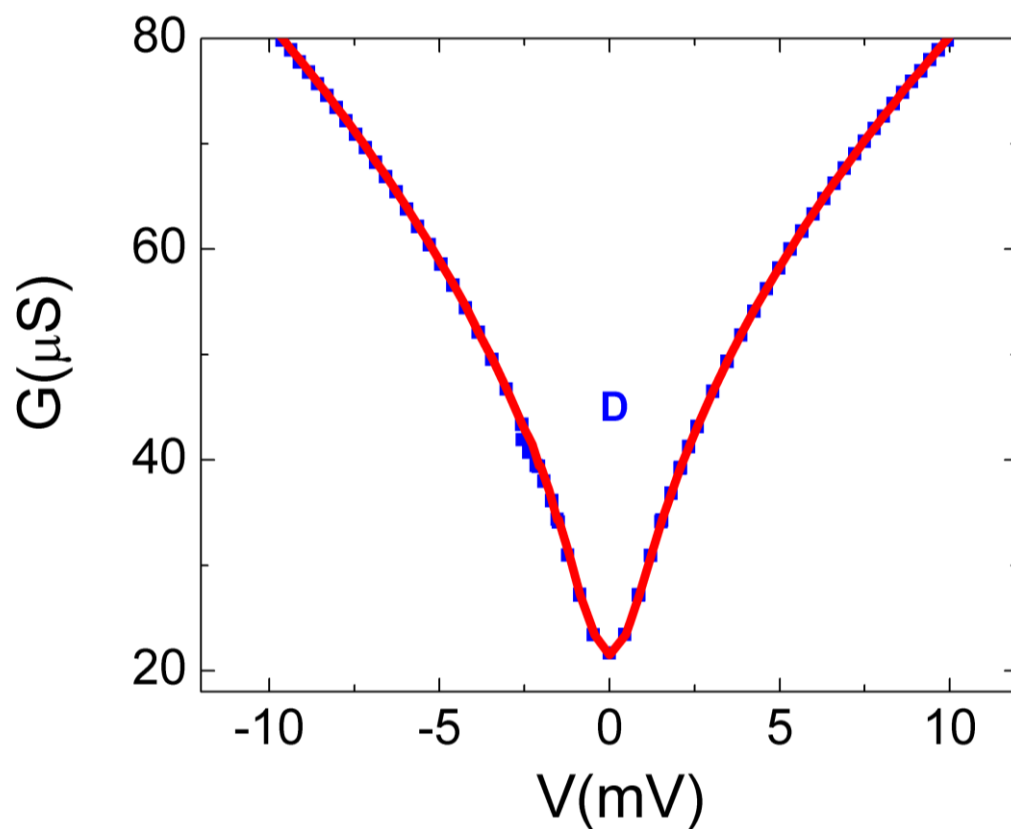


Fig. 4.2 (c) The $G(V)$ curve of junction D in zero magnetic field (symbols) and in a perpendicular magnetic field of 4 T (solid curve). Data were taken at 2.5 K.

(d)

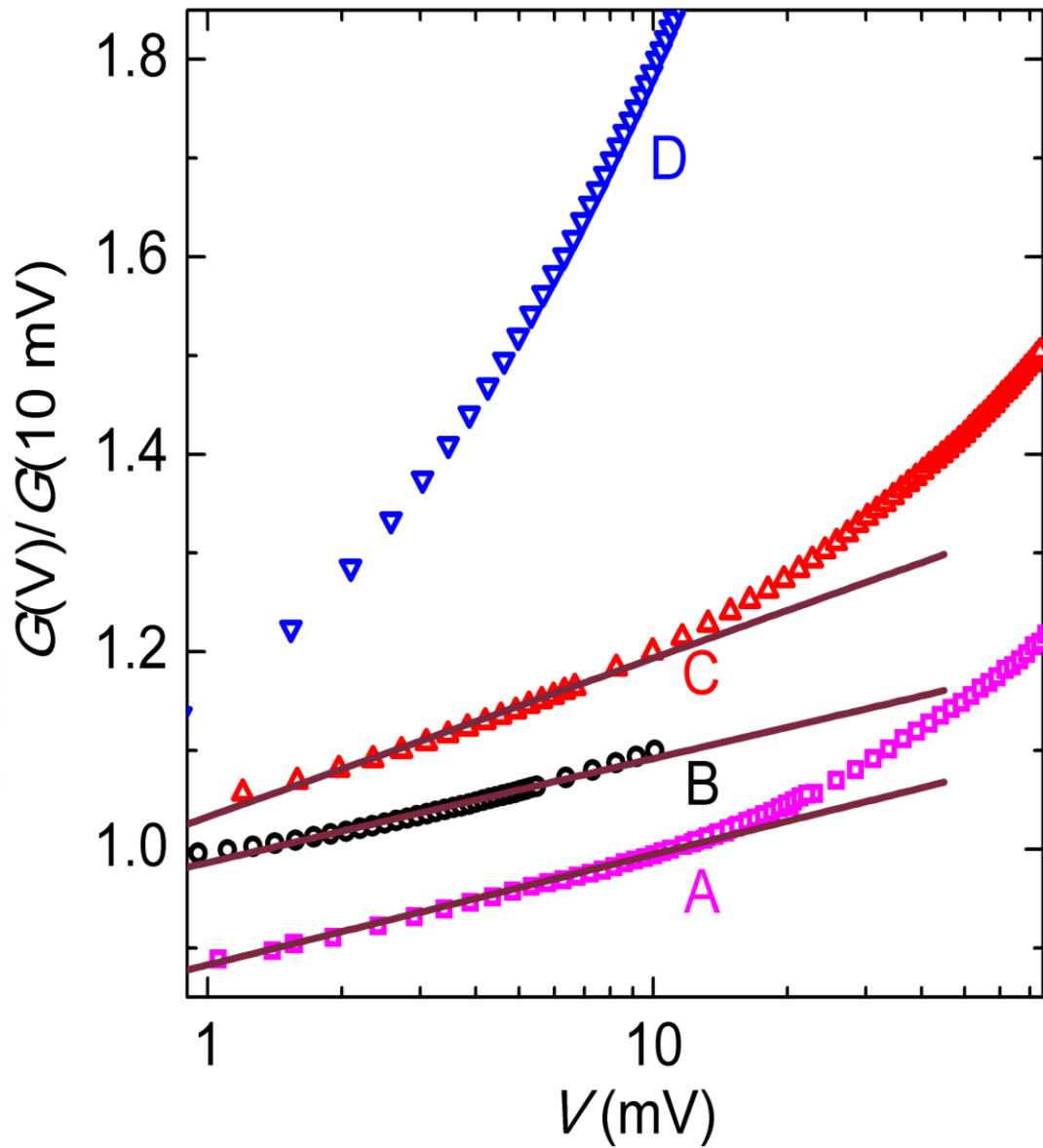


Fig. 4.2 (d) Normalized differential conductance, $G(V)/G(10 \text{ mV})$, as a function of bias voltage for junctions A – D, as indicated. The straight solid lines are least-squares fits to the equation of conductivity in Sec.2.4. For clarity, the data for the junctions B, C and D have been vertically shifted up by 0.1, 0.2 and 0.8, respectively. Data were taken at 2.5 K.

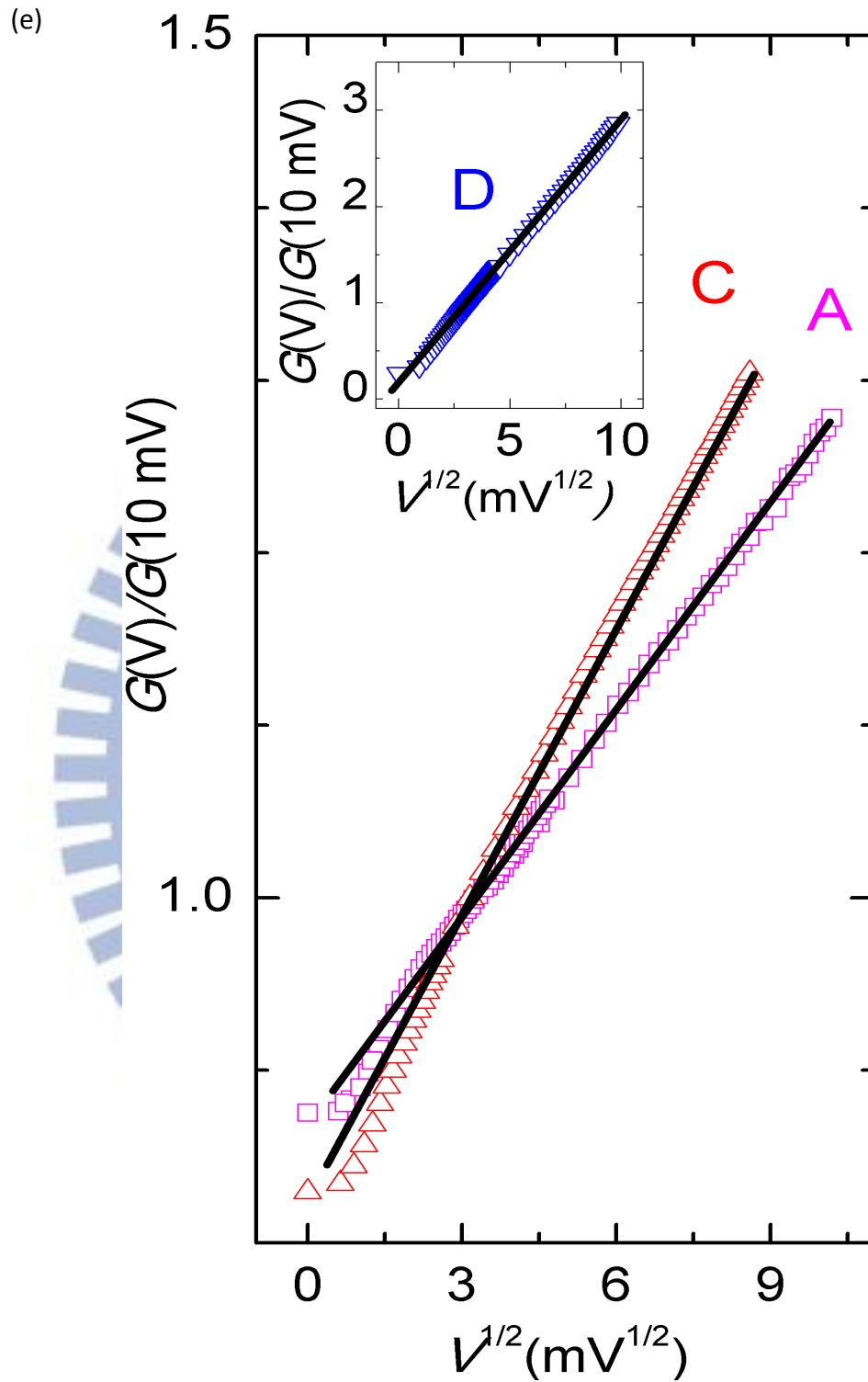


Fig. 4.2 (e) $G(V)/G(10 \text{ mV})$ versus \sqrt{V} for junctions A, C and D, as indicated. The straight solid lines are guide to the eyes. Data were taken at 2.5 K.

4.3 A Comparison with the Conventional EEI Effect

-- *Ruling out the weak-localization and electron-electron interaction effects*

In order to understand our $G(V)$ results in a quantitative manner, we first determine the parabolic background tunneling conductance (PBTC) in our junctions (see Sec.2.2) [34]. It is known that a PBTC is characteristic of every metal-insulator-metal tunnel junction at high bias voltages, where the disorder induced suppression in DOS, regardless of its origin, is insignificant [9, 26]. Figures 4.3 (a-b) shows the $G(V)$ curves in a wide range of V for the junctions A and D. It is seen that $G(V) \propto V^2$ (the solid curves) in the wide interval of $|V| \approx 200 - 400$ mV. This observation confirms that our measured zero-bias conductance dips are superimposed on a PBTC. From this fitted PBTC, we can extrapolate the zero-bias conductance, $G_{\text{para}}(0)$, of an as would be ideal Al/AlOx/Cr tunnel junction consisting of a “clean” Cr electrode. The extrapolated value of $G_{\text{para}}(0)$ contains the information about the DOS at the Fermi energy, E_F , in a clean Cr electrode, because for small bias voltages and at low temperatures, $G_{\text{para}}(0)$ can be approximated by $G_{\text{para}}(0) = PN_{\text{Al}}(0)N_{\text{Cr,c}}(0)$, where P is the electron tunneling rate (which depends on the barrier height and width), and $N_{\text{Al}}(0)$ and $N_{\text{Cr,c}}(0)$ are the DOS at E_F in the Al and clean Cr electrodes, respectively [33]. The DOS at E_F in our granular and disordered Cr electrode, $N_{\text{Cr,d}}(0)$, can then be evaluated through the relation $N_{\text{Cr,d}}(0) = N_{\text{Cr,c}}(0) \times [G(0)/G_{\text{para}}(0)]$, where the measured zero-bias conductance $G(0) = PN_{\text{Al}}(0)N_{\text{Cr,d}}(0)$. With the literature value of $N_{\text{Cr,c}}(0) = 3.5 \times 10^{47} \text{ J}^{-1} \text{ m}^{-3}$ in clean Cr metal [45], our extracted magnitudes of $N_{\text{Cr,d}}(0)$ are listed in Table 1.

As mention in Sec. 2.3, the effective dimensionality of the EEI effect will cross over from 2D to 3D at $|V| \gtrsim V_c \approx (4\pi^2\hbar D)/(et^2)$ [36]. In 2D, $(\delta N_2(\epsilon))/(N_2(0))$ has logarithmic energy dependence, while $(\delta N_3(\epsilon))/(N_3(0))$ is proportional to $\sqrt{\epsilon}$. At first glance, since our junctions A and B are nominally weakly disordered ($k_F\ell \approx 4 - 5$), one might attempt to

attribute our $G(V) \propto \ln V$ results to the 2D EEI effect. However, such an interpretation can be ruled out as follows. By comparing our measured $\ln V$ dependence of $G(V)$ in the junction A (the least disorder system in our samples) with the prediction of $(\delta N_2(\epsilon))/N_2(0)$ (see Sec.2.3), we obtained a value $\lambda_2 \approx 448$. This value is one order of magnitude larger than the theoretical prediction of $\lambda_2 = \ln[(\hbar D \kappa^4 t^2)/(4\pi^2 \epsilon)] \approx 43$, where $\kappa = (me^2 k_F t)/(2\pi^2 \hbar^2 \epsilon_0)$, and ϵ_0 is the permittivity of the vacuum [9] (we took a typical electron energy $\epsilon = 5$ meV). Furthermore, in the high bias voltage regime, a comparison of our measured $G(V) \propto \sqrt{V}$ result with $(\delta N_3(\epsilon))/N_3(0)$ yielded a value of $\lambda_3 \approx 88$, which is also far higher than the theoretical prediction of $\lambda_3 \approx 2$ [9]. Therefore, our observed “giant” $G(V)$ dips cannot be due to the conventional EEI effect in weakly disordered homogeneous conductors. Furthermore, the WL effects are even less important, because, on one hand, the electron dephasing length is short in granular samples [46] and, on the other hand, our Cr electrodes are magnetic [47]. Therefore definitely, the granularity in the structure of our Cr electrodes must play an important role [6-8], as to be addressed in Sec. 4.4 and Sec. 4.5.

(a)

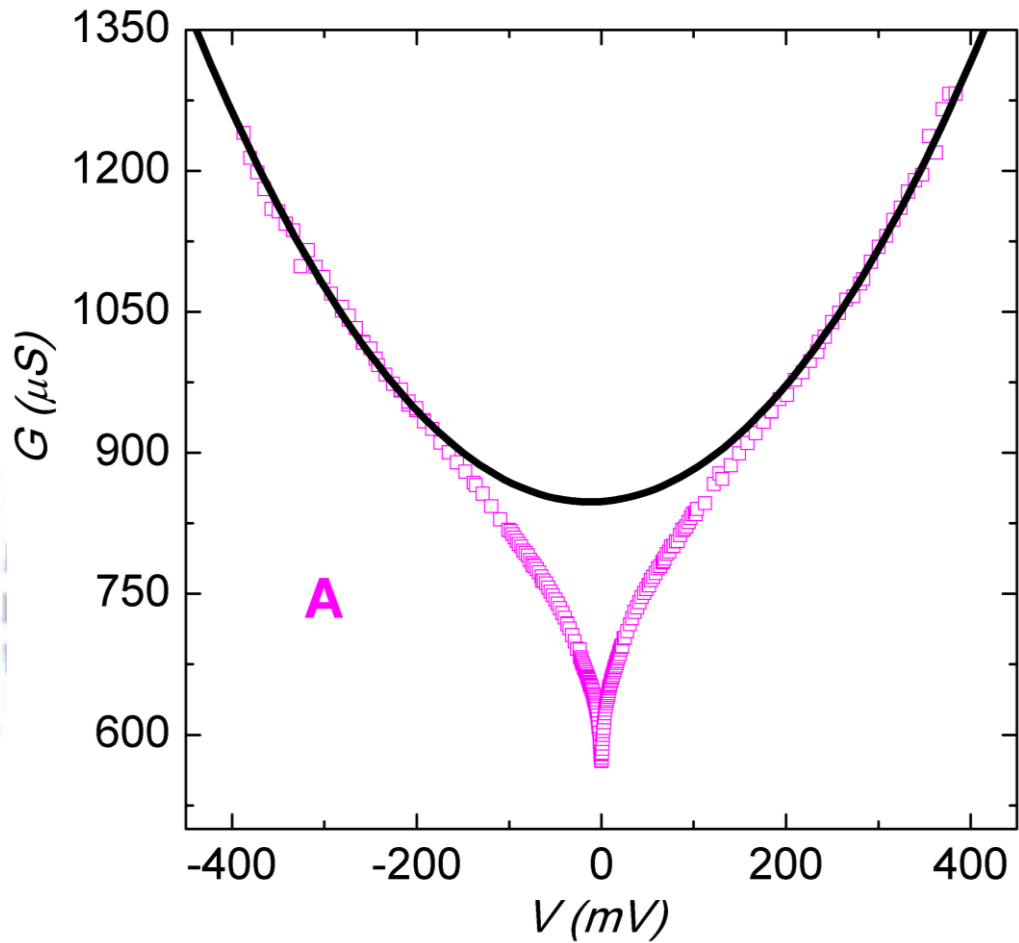


Fig. 4.3 (a) $G(V)$ spectra of junctions A at 2.5 K in a wide bias voltage interval, as indicated. The symbols are the experimental data and the solid curves are parabolic fits. The solid curves in junctions A are described by $G_{\text{para}}(V) = 848 + 0.067V + 0.0028V^2$ where $G_{\text{para}}(V)$ is in microsiemens and V in millivolt.

(b)

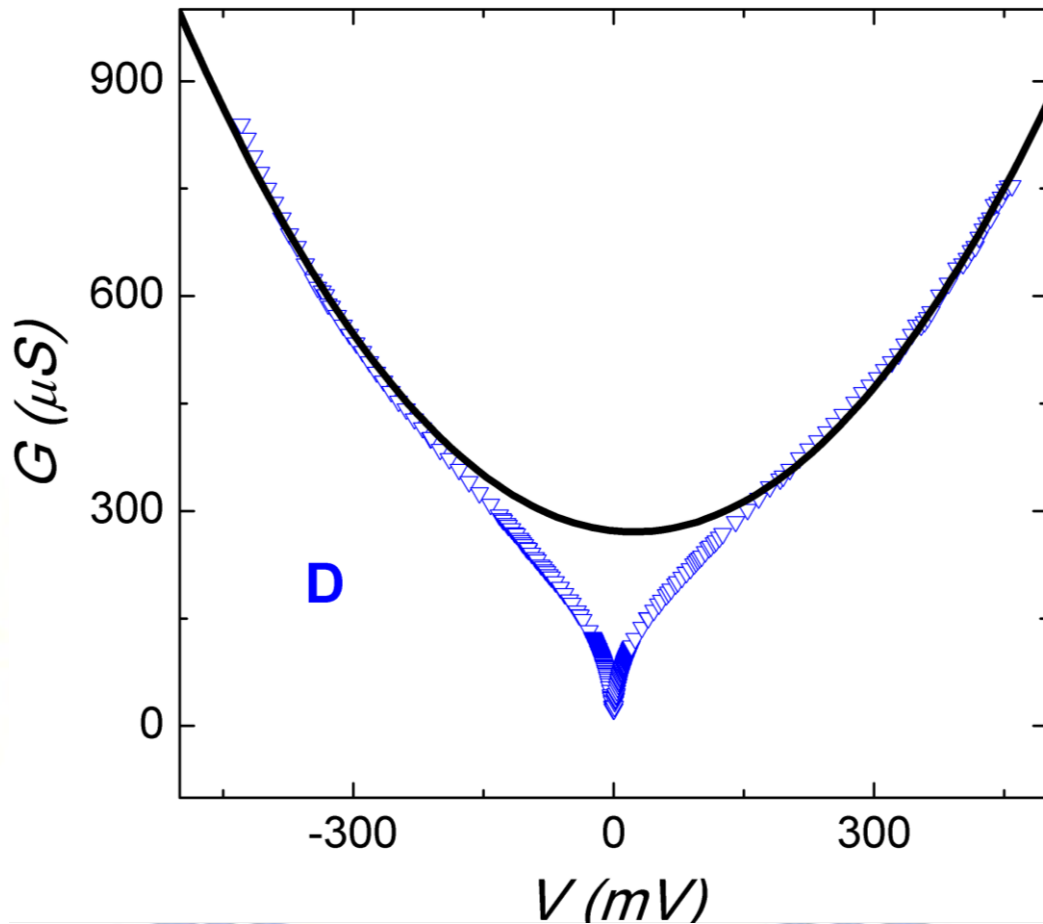


Fig. 4.3 (b) $G(V)$ spectra of junctions D at 2.5 K in a wide bias voltage interval, as indicated. The symbols are the experimental data and the solid curves are parabolic fits. The solid curves in junctions D are described by $G_{\text{para}} = 272 - 0.12V + 0.0026V^2$, respectively, where G_{para} is in microsiemens and V in millivolt.

4.4 A Comparison with the Theory of Granular Metals

-- *Logarithmic temperature dependence of conductivity*

Let us discuss that our results can be satisfactorily, but not fully, interpreted in terms of the recent theory of granular metals. We have fitted our measured $\sigma \propto \ln T$ results with the predicted $\sigma(T)$ (see Sec. 2.4). To carry out the least-squares fits, we assume a value of the charging energy $E_c \approx 10 k_B T^*$, where T^* is the temperature below which the $\sigma \propto \ln T$ law holds. Taking this value of E_c and the sample dimensionality $d = 3$ (because our Cr granules are disk-shaped with a height of $\approx 0.5\text{--}2.5$ nm, which is much smaller than our mean film thickness of 15–30 nm), we have extracted the values of the parameters σ_0 and g in our samples (see Table 1). It should be noted that the extracted σ_0 and g values are insensitive to the choice of E_c value, because E_c appears in the argument of a logarithmic function [48]. Inspection of Table 1 indicates that in the junctions A – C, we obtained $g \gg 1$. This result is in good consistency with the prerequisite for the predicted $\sigma(T)$ to be applicable. On the other hand, our extracted value of $g \approx 1$ in the junction D implies that this sample falls marginally inside the regime of validity of the predicted $\sigma(T)$. We notice that the predicted $\sigma(T)$ was formulated by considering a periodic cubic array of uniformly sized grains and neglecting dispersion of the intergrain tunneling conductance [25], while our samples contained random arrays of varying-sized, disk-shaped granules [6]. Therefore, a close quantitative comparison of our (and other groups' [24, 49, 50]) experiment with theory is not possible at this stage.

Another important feature of the predictions of the theory of granular metals is that the predicted $\sigma(T)$ should be valid at any magnetic field. This is indeed confirmed by our experiment. We have measured $\sigma(T)$ of the Cr electrode in the junction A between 4 and 20 K in both zero magnetic field and in a perpendicular magnetic field of 4 T (see Fig. 4.4 (a)). The measured values are the same to within our experimental uncertainty. On contrary,

the WL effect, if any exists, should be very sensitive to and suppressed by even a small magnetic field [47]. If the EEI effect were responsible, we should then have observed a \sqrt{T} , but not a $\ln T$, dependence in this sample in this temperature interval [51]. Therefore, both the WL and EEI effects are irrelevant to our observations in Figs. 4.1 (a-b).

The mean energy-level spacing δ in our Cr granules may be evaluated as follows. We have carried out AFM studies of a film deposited under conditions similar to those used for the fabrication of the junction B. We found that the Cr film formed a granular structure consisting of disk-shaped grains of $\approx 60 \pm 20$ nm in diameter and $\approx 1.5 \pm 1$ nm in height, along with a few larger aggregations. By taking an average diameter of ~ 60 nm and an average height of ~ 1.5 nm, we obtain an estimate of $\delta = 1/N_{cr,d}(0) \bar{V} \approx 2 \mu\text{eV}$, where \bar{V} is the average granule volume. This δ value in turn suggests a characteristic temperature $T_B \approx g\delta/k_B \approx 1$ K above which the predicted $\sigma(T)$ equation is expected to apply. Experimentally, the $\sigma \propto \ln T$ law in our junction B is observed in the temperature interval 0.3–7 K, see Fig. 4.1 (b). This degree of agreement is satisfactory, considering that the evaluations of parameters in a granular sample unavoidably involve large uncertainties.

Using our estimated values of $E_c \approx 6$ meV (see Table 1) and $\delta \approx 2 \mu\text{eV}$, we obtained the ratio $E_c/\delta \approx 3 \times 10^3$. This ratio suggests the existence of a broad range for logarithmic corrections to conductivity. However, even under such circumstances, Feigel'man et al. have theoretically shown that a simple $\sigma \propto \ln T$ law should still hold in a wide range of temperature [52]. This prediction is confirmed by the present experiment.

(a)

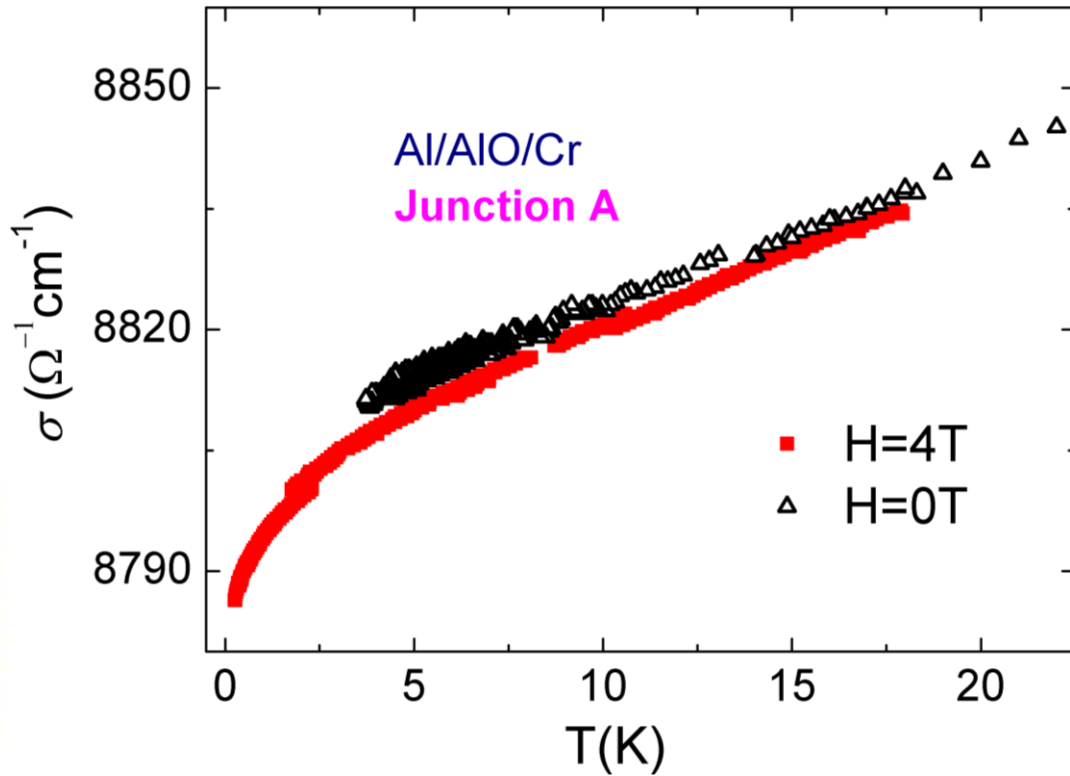


Fig. 4.4 (a) Plots of temperature-dependent conductivities in Junction A under magnetic field $H = 0 \text{ T}$ (triangles) and $H = 4 \text{ T}$ (squares). The small difference between two curves is within our experimental uncertainty. The results confirm that the WL effect (which is sensitive to the magnetic fields) is irrelevant to our system, while the prediction on conductivity in the theory of granular metals should be valid at any magnetic field.

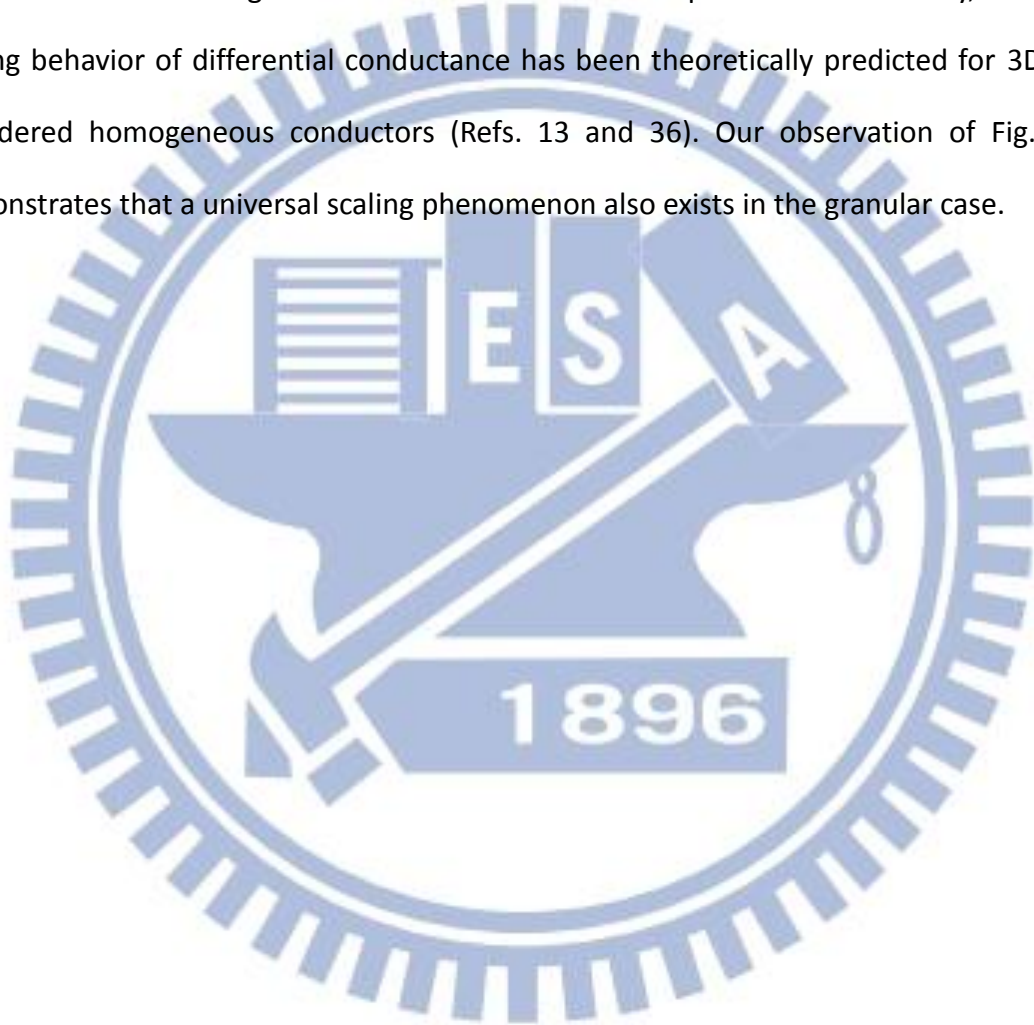
4.5 A Comparison with the Theory of Granular Metals

-- *Differential conductance curves and tunneling density of states*

Tuning to the differential conductance curves, we discuss the crossover behavior of $G(V)$ from the $\ln V$ to \sqrt{V} dependence. This occurs at a characteristic bias voltage of $V_c \approx E_c/e \approx 10k_B T^*/e$. Theoretically, the application of the predicted $\nu_3(\epsilon)$ (see Sec. 2.4) requires the condition $\max(T, \epsilon) \lesssim E_c$ to be satisfied. That is, at low temperatures such that $k_B T < \epsilon$, the $\nu_3(\epsilon) \propto \ln \epsilon$ law is predicted for the regime $\epsilon \lesssim E_c$. On the other hand, the variation in ν_3 with ϵ in the opposite limit ($\epsilon \gtrsim E_c$) has not been calculated. Experimentally, in the junctions A – C, we observed $G(V) \propto \ln V$ in the low bias voltage regime ($V \lesssim V_c \approx E_c/e \approx$ a few to ~ 10 mV). This is qualitatively in line with the prediction of $\nu_3(\epsilon)$. However, a close comparison with theory cannot be made at this stage, because the numerical prefactor A in the predicted $\nu_3(\epsilon)$ was calculated for the case when the logarithmic term is much smaller than 1 [26]. Quantitatively, the magnitudes of the $G(V)$ dips we observed are much larger than that predicted by $\nu_3(\epsilon)$ in Sec.2.4. On the other hand, our g values are larger than the critical intergrain tunneling conductance $g_c = (2\pi d)^{-1} \ln(E_c/\delta)$ (≈ 0.4 , using the above E_c/δ value) [44]. Therefore, we do not expect to find a “hard” gap in our samples [27]. Our $G(V) \propto \sqrt{V}$ results in the high bias voltage regime ($V \gtrsim V_c$) also have to await a future theoretical explanation [52].

Finally, in the junction D, we did not observe any $G(V) \propto \ln V$ dependence even at relatively low bias voltages, which may be due to the fact that $g \approx 1$ in this sample and thus the prediction of $\nu_3(\epsilon)$. is marginally applicable. However, recall that we found the $\sigma \propto \ln T$ behavior, as predicted by the predicted $\sigma(T)$. In fact, $G(V) \propto \sqrt{V}$ was observed in this sample in a wide range of $|V| \approx 1-100$ mV at 2.5 K, the insert of Fig. 4.2 (e). Furthermore, we found that in this particular sample, the scaled differential conductance $[G(V, T) - G(0, T)]/\sqrt{T}$ versus the combined parameter $\sqrt{e|V|/k_B T}$ for different

measurement temperatures between 2.5 and 32 K collapse closely onto a single curve, Fig. 4.5 (a). This result strongly suggests the existence of a universal scaling function in the $g \approx 1$ regime. That is, there exists a function f such that $G(V, T) - G(0, T) = \sqrt{T} \times f(\sqrt{eV/k_B T})$, where f should depend on the combined parameter $eV/k_B T$, instead of depending independently on eV or $k_B T$. For comparison, Fig. 4.5 (b) shows the unscaled $G(V)$ versus bias voltage V at five measurement temperatures. Previously, a universal scaling behavior of differential conductance has been theoretically predicted for 3D weakly disordered homogeneous conductors (Refs. 13 and 36). Our observation of Fig. 4.5 (b) demonstrates that a universal scaling phenomenon also exists in the granular case.



(a)

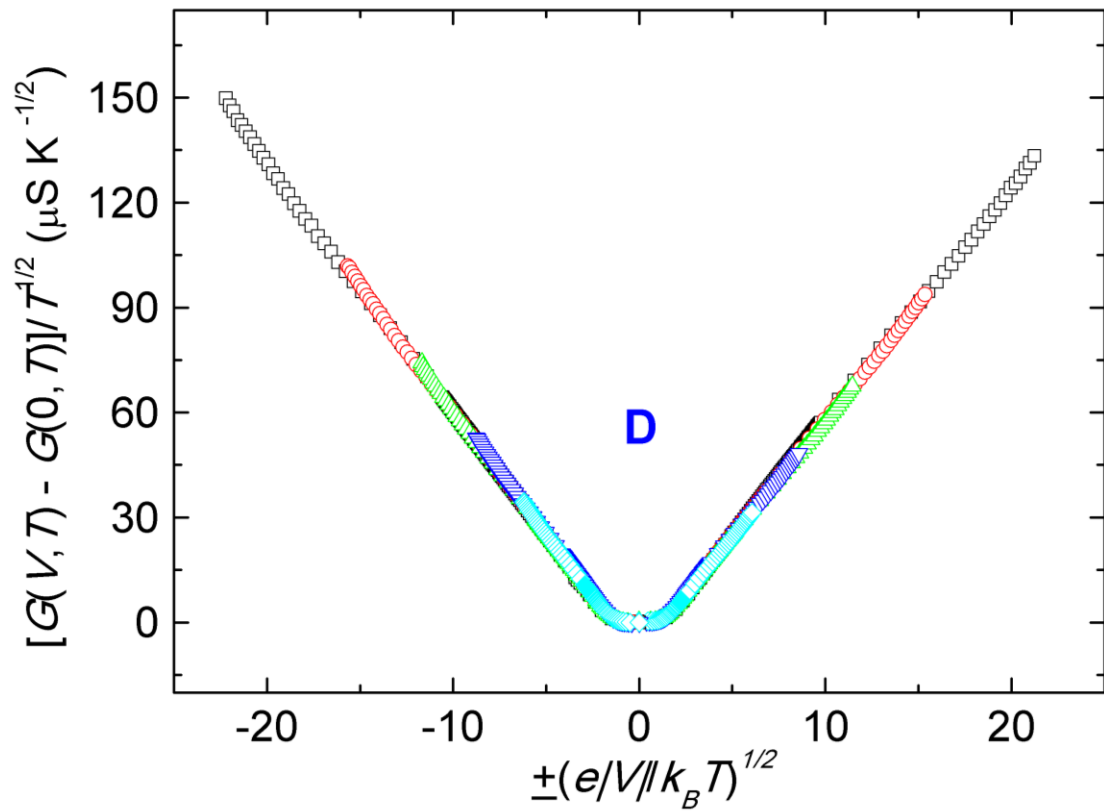


Fig. 4.5 (a) Normalized differential conductance, $(G(V, T) - G(0, T)) / \sqrt{T}$, as a function of the combined parameter $\sqrt{eV/k_B T}$ for the junction D at five measurement temperatures. Notice that the data points collapse closely.

(b)

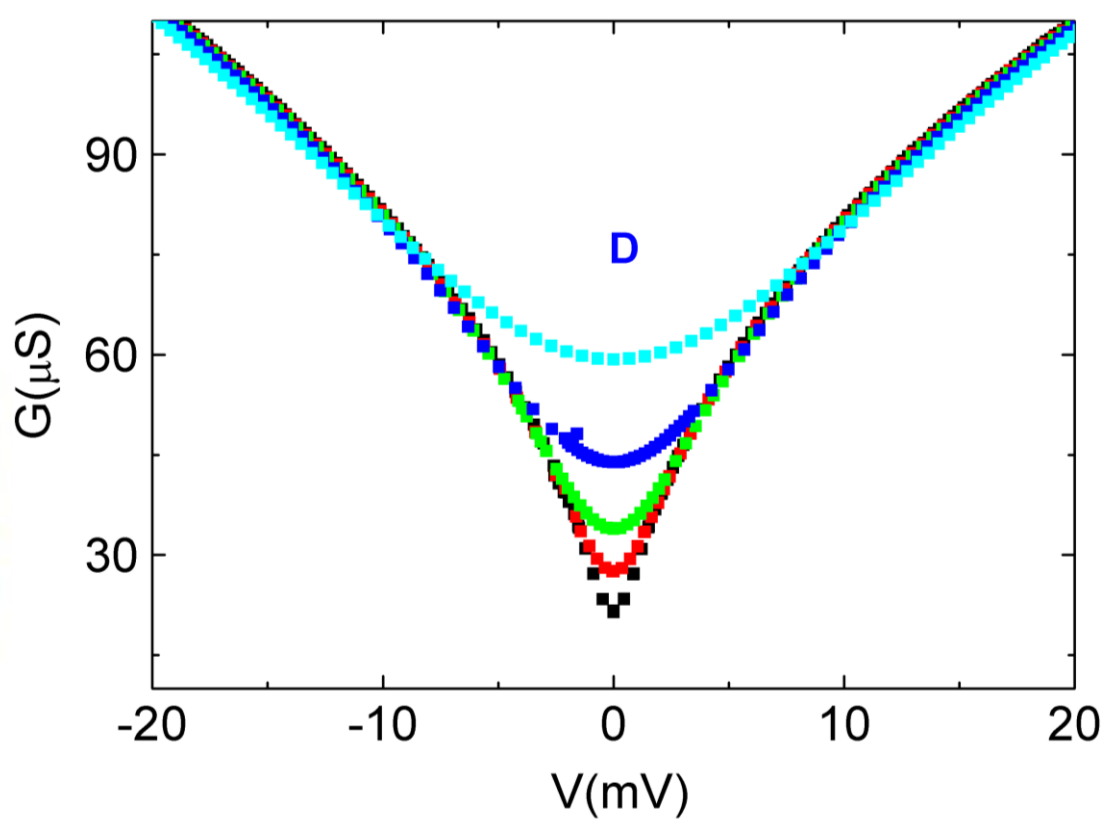


Fig. 4.5 (b) Unscaled $G(V)$ versus bias voltage V at (from bottom up) 2.5, 5.0, 9.0, 16 and 32 K.

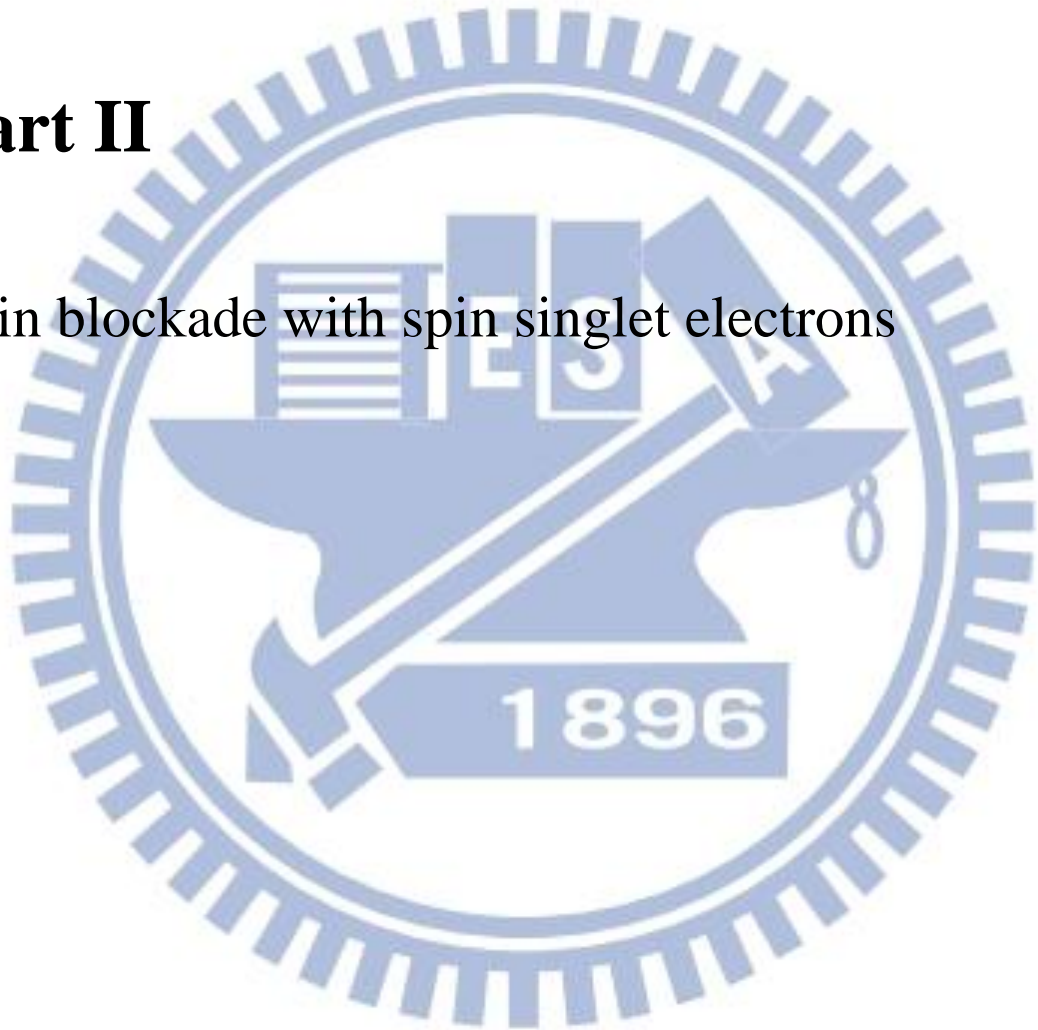
Chapter 5

Summary

We have measured the conductivities $\sigma(T)$ in granular Cr electrodes and the differential conductances $G(V)$ in Al/AlO_x/Cr tunnel junctions at liquid-helium temperatures. In samples with dimensionless intergrain tunneling conductances $g \gg 1$, we found $\sigma \propto \ln T$ and $G(V) \propto \ln V$ at low bias voltages. These results are satisfactorily understood in light of the recent theory of granular metals. A crossover of $G(V)$ from the $\ln V$ to \sqrt{V} dependence was observed at high bias voltages. In a sample with $g \simeq 1$, we found $\sigma \propto \ln T$ and $G(V) \propto \sqrt{V}$ in a wide bias voltage interval. Moreover, the normalized differential conductance $[G(V, T) - G(0, T)]/\sqrt{T}$ reveals a universal scaling behavior with the combined parameter $\sqrt{e|V|/k_B T}$ in a wide range of temperature. This last observation requires a further theoretical explanation. Finally, we would like also to note that, while the theory of granular metals considers a periodic array of uniformly sized grains, in real samples one often has some distribution in granule size. The effect of such size distribution on our results in the present study has yet to be fully addressed.

Part II

Spin blockade with spin singlet electrons



Chapter 6

Introduction

6.1. Motivation

Quantum dot (QD) systems, developed with the growing of the semiconductor device fabrication technique, provide a possible candidate for the application on the quantum computer area [53-55] and a path to investigate the fundamental physics, especially atomic physics, in more easily accomplishable experimental conditions [56,57].

In classical computers, information is represented by a string of bits indicating as “0” and “1”. However, in the quantum world, if a system can be controlled between two states, resembling as the mentioned “0” and “1”, the wave property enables the information to be computed in a combination or superposition of the two states. And, this so called “quantum parallelism” ability makes quantum computers more powerful to solve the problems which are considered intractable nowadays [58].

We can summarize five requirements [59] for establishing quantum computers. And, through the introduction on these requirements in the following paragraph, we could know how **spins are treated as quantum bit (qubit) in double QD systems [53, 54, 59] and what kind of roles the spin blockade phenomenon can play [60-63]**. These both motive us to study our topics in this thesis:

1. A system with a few discrete quantum states

A two-level system is normally ideal for representing the qubit. For a single spin (a one-bit operation), the two levels can be *spin up* and *spin down* respectively; for a two-bit operation, the two-particle spin configuration as *spin singlet* and *spin triplet* can be are utilized as two discrete levels.

2. Able to accomplish logic gates

A XOR (or controlled-NOT) gate, known to be employable for any arbitrary quantum computation, can be produced by two square roots of the swap operation of a two-qubit gate with a set of a one-qubit gate.

3. High coherence time

Spin state coherence time should be longer enough to execute a logic gate accurately. That is, it should be at least 1000 times larger than the logic gate operation time. As we know, spin is less sensitive to the environment as comparing with charge. However, according to materials composed of the QD systems, the spin orbital interaction and/or the hyperfine interaction will play important parts to influence the coherence.

4. Able to initialize the qubit state

5. Able to measure the qubit state

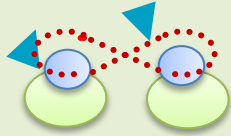
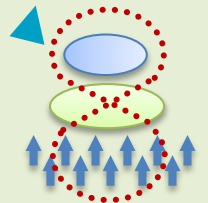
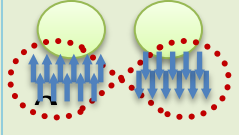
Before having a brief illumination on the Pauli spin blockade (SB) in a double QD system in Sec. 7.3, we can first consider it just as a spin dependent barrier that only allows electrons to flow through if they are spin singlet, whereas spin triplets will lead the system to a blockade. This property helps out both the requirement 4 & 5 [60-63], since we can simply prepare a two-electron system to stay in triplet spin states for experiments (i.e. to initialize the qubit state). Further, we can measure or identify which qubit state the system is by only

observing the electron-flow signals or the tunneling current (i.e. to measure the qubit state).

In this work, we observe a novel spin blockade phenomenon in the double QD system -- the singlet spin blockade (SSB). In contrast to the Pauli spin blockade resulting from forming one of three triplet states randomly, whenever SSB takes place, it blocks with the only state -- electron spin singlet. We propose a mechanism to utilize the singlet spin blockade and the hyperfine interaction to entangle the nuclear spins in Sec. 6.2. For a two-qubit operation, we need to establish links between distant qubits; that is, to entangle states between separated quantum systems. In the past studies, the entanglement between electron spins or between electron spin and nuclear spin is possible [53, 65]. However, so far the entanglement between nuclear spins has not been achieved. In Table 2, the conditions or developments for electron spins and nuclear spins as quantum information carriers in GaAs, which composes of our QD system, are summarized.



Table 2 Electron spins vs. nuclear spins as quantum information carriers

	Electron Spin in GaAs	Nuclear Spins in GaAs	
Two-level system	○	○(Four level)	
Initialization	○	○(Polarization ~ 40%) [66]	
Coherence	○(~ μs) [63]	○(~ ms) [67]	
Measurement	○	○	
Unitary operation			
1 qubit operation	○(ESR)	○(NMR)	
2 qubit operation	electron-electron ○  [53]	electron-nuclear ○?  [65]	nuclear-nuclear x? 

6.2 (A Proposal)

To Entangle Nuclear Spins with Singlet Spin Blockade

The singlet spin blockade occurs when there is only one electron staying in each of the double QDs and the two-electron spin configuration is singlet. In this section, we propose a mechanism that while the singlet spin blockade phenomenon is relieved via the spin flip-flop process due to the hyperfine interaction between electron spin and nuclear spin, the nuclear spins residing in two QDs are entangled at the same time.

In Fig. 6.2 (a), each of the two QDs has a single electron interacting with one of numerous nuclear spins inside the QDs via the hyperfine interaction, and the Hamiltonian can be expressed as

$$H_{hf} = \sum_{i,j} \alpha_{ij} \vec{S}_i \cdot \vec{I}_j$$

where \vec{S}/\vec{I} is the spin operator for electron spin/ nuclear spin, α is the coupling strength, and i/ j indicates the QD (QD1 or QD2) where the electron/the nuclei stays. The cross-dot interactions are tiny, so that the α_{12} and α_{21} terms can be dropped. If we further assume that α_{11} and α_{22} have the same strength as $\alpha_{11} \approx \alpha_{22} = A$, then the hyperfine interaction can be shortened as

$$\begin{aligned} H_{hf} &= \sum_{i,j} \alpha_{ij} \vec{S}_i \cdot \vec{I}_j \\ &= \alpha_{11}(S_{1+}I_{1-} + S_{1-}I_{1+} + S_{1z}I_{1z}) + \alpha_{12}(S_{1+}I_{2-} + S_{1-}I_{2+} + S_{1z}I_{2z}) \\ &+ \alpha_{21}(S_{2+}I_{1-} + S_{2-}I_{1+} + S_{2z}I_{1z}) + \alpha_{22}(S_{2+}I_{2-} + S_{2-}I_{2+} + S_{2z}I_{2z}) \\ &\quad \text{for } \alpha_{11} \approx \alpha_{22} = A; \alpha_{12} = \alpha_{21} = 0 \\ &= A(S_{1+}I_{1-} + S_{1-}I_{1+} + S_{1z}I_{1z}) + A(S_{2+}I_{2-} + S_{2-}I_{2+} + S_{2z}I_{2z}) \end{aligned}$$

For example, if the hyperfine interaction acts on a state $|\uparrow_1\uparrow_2\uparrow_1\downarrow_2\rangle$, it turns out to be $|\uparrow_1\downarrow_2\uparrow_1\uparrow_2\rangle$

$$\begin{aligned}
 H_{hf}|\uparrow_1\uparrow_2\uparrow_1\downarrow_2\rangle &= \{A(S_{1+}I_{1-} + S_{1-}I_{1+} + S_{1z}I_{1z}) + A(S_{2+}I_{2-} + S_{2-}I_{2+} + S_{2z}I_{2z})\}|\uparrow_1\uparrow_2\uparrow_1\downarrow_2\rangle \\
 &= A|\uparrow_1\downarrow_2\uparrow_1\uparrow_2\rangle
 \end{aligned}$$

Only at the condition that spin directions of the electron and the nucleus within the same dot are opposite, the spin flip-flop process is executable to exchange their spin states. However, if we only consider the spin states before and after the interaction (such as the example above, $|\uparrow_1\uparrow_2\uparrow_1\downarrow_2\rangle$ turns to be $|\uparrow_1\downarrow_2\uparrow_1\uparrow_2\rangle$), it looks like that the interaction exchange electron and nuclear spin states with each other no matter whether their spins direct oppositely or not. Since if the spin states of the electron and the nuclei have the same orientation, the states after the interaction will be the same as those after the exchange (if it really happens).

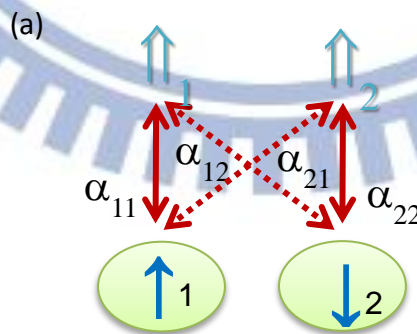


Fig. 6.2 (a) The schematic diagram of the hyperfine interaction in a double QD system, where \uparrow/\uparrow shows the electron/nuclear spin direction and α is the coupling strength.

Similarly, we can also see what would happen if the hyperfine interaction works on two electrons forming the spin singlet state $|(\uparrow_1\downarrow_2 - \downarrow_1\uparrow_2) \uparrow_1\uparrow_2\rangle$

$$\begin{aligned} H_{hf}|(\uparrow_1\downarrow_2 - \downarrow_1\uparrow_2) \uparrow_1\uparrow_2\rangle &= H_{hf}|\uparrow_1\downarrow_2\uparrow_1\uparrow_2\rangle - H_{hf}|\downarrow_1\uparrow_2\uparrow_1\uparrow_2\rangle \\ &= A|\uparrow_1\uparrow_2\uparrow_1\downarrow_2\rangle - A|\uparrow_1\uparrow_2\downarrow_1\uparrow_2\rangle \\ &= A|\uparrow_1\uparrow_2(\uparrow_1\downarrow_2 - \downarrow_1\uparrow_2)\rangle \end{aligned}$$

Again, the spin states of the electrons and the nuclei exchange! Meanwhile, the entanglement between electrons as a spin singlet state passes onto the nuclei. Recall that the spin flip-flop process, no matter which direction the electron spin and the nuclear spin point to, can be retreated as an exchange spin state action within the same dot as just mentioned. And further, **for the spin singlet state**, even though we do not know the electron spin direction in one dot but we do know the electron spin in the other dot should direct oppositely. Therefore, when two electron spins respectively exchange the state with the nuclear spin in its own dots, the connection between nuclei in two separated dots is established. The probability of being either $|\uparrow_1\downarrow_2\rangle$ or $|\downarrow_1\uparrow_2\rangle$ in electrons now passes toward an arbitrary nuclear spin pair which is entangled as forming to be the singlet state at the same time.

Compared with the Pauli spin blockade keeping the system in triplet spin states that we cannot determine the precious one, the singlet spin blockade with the aim of the spin flip-flop process via the hyperfine interaction provides a way to entangle the nuclear spins staying in two dots to be just as one spin state—the singlet spin state. We can also calculate how many nuclear spin pair will be entangled under the steady condition if this mechanism works repetitively. And, the calculation on the expected value of the entangled nuclear spin pairs under the steady condition and a possible verified measurement as our further work are introduced in Appendix (A).

Chapter 7

Background and Theory

Basics of the semiconductor QDs and the relative spin-dependent electron transport behavior will be introduced in this chapter. We start with the general transport properties of Sec. 7.1 *single quantum dot systems*, and then extend to Sec. 7.2 the *vertical double quantum dots* which we chose as our system in this thesis. In such a system, we control and limit the electron number to be within one or two, so that we can see the occurrence of Sec. 7.3 (*Pauli spin blockade*). Further, a more clear vision of this spin blockade behavior will be shown with an understanding on *the two-electron energy diagram* in Sec. 7.4. We *introduce the singlet spin blockade* (SSB) in Sec. 7.5, while *the two-electron singlet-triplet ground state transition*, which we demonstrate in this thesis to achieve SSB, is in Sec. 7.6.

7.1 Single Quantum Dot Systems

As the development in the semiconductor device fabrication technique grows, it is possible to restrict electrons in a nano- to micro-meter-sized device composed of 10^3 to 10^9 atoms. We call such a small device as *Quantum dot (QD)* where electrons are confined to a dimension close to de Broglie wavelength (~ 100 nm). Therefore, it has two distinct well-known features -- *the discrete energy spectrum* and *manifest quantum effects*, and is often regarded as an artificial atom [68].

Since every semiconductor material has different or its own bandgap, the conduction band of multilayers of semiconductors can form a potential well with discrete energy levels sandwiched between barriers as in Fig. 7.1 (a). In such semiconductor heterostructures, the confinement is one dimensional, or along the z-direction in this thesis. All the parameters, including electrode reservoirs for electron transport between the external environment and QDs, are well-considered so that all the excited states in the z-direction will be empty; that is, only the ground state is occupied with electrons. For building a quantum dot, however, it is still not enough, and we need to further confine the x-y plane. This can be done just with the evaporated metal gates or combining with the etching technique. And, in this way, we will have disk-like shaped quantum dots. The metal gates surround the semiconductor dot, so that we can control the depletion region by applying the gate voltage, V_g , and the confinement in x-y plane or the size of the dot will be changed. That is to say, energy levels of the dot with respect to the reservoirs are able to be tuned with V_g . The equivalent circuit diagrams of the vertical and lateral QD systems are shown in Figs. 7.1 (b-c).

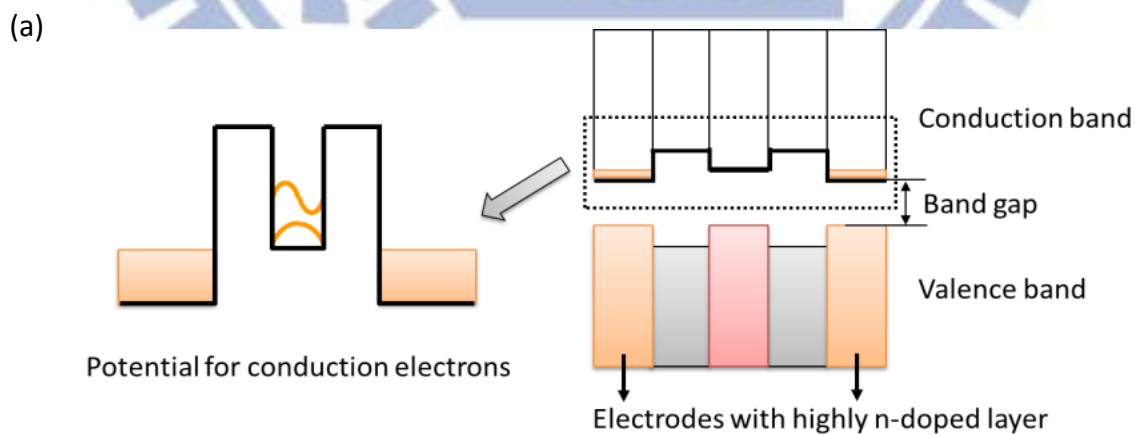
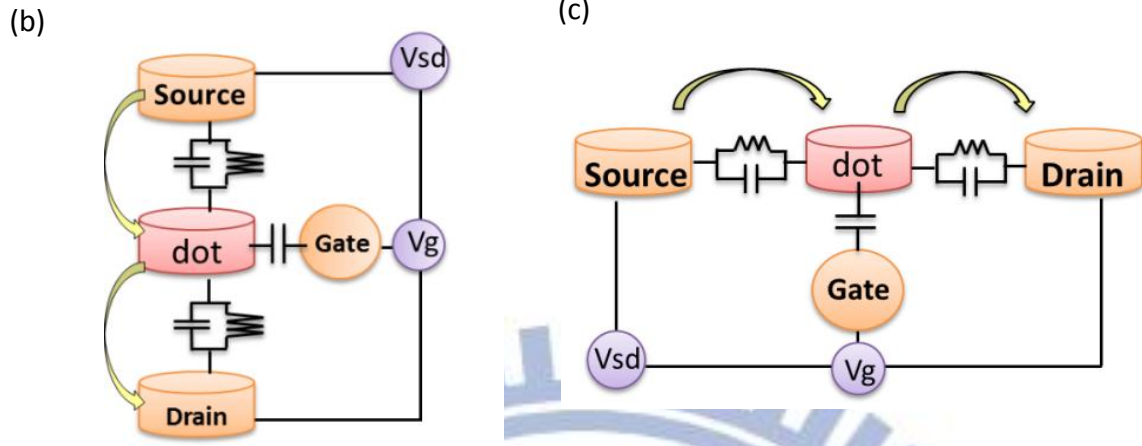


Fig. 7.1 (a) Schematic diagrams of semiconductor heterostructures such as AlGaAs/GaAs/AlGaAs that confine electrons to a plane.



Figs. 7.1 (b-c) The equivalent circuits for the (b) vertical and (c) lateral quantum dot system. The gate couples to the dot capacitively, and barriers between electrode reservoirs and the dot can be represented as a parallel connection of resistance and capacitor.

In a disk-like shaped QD system, the energy spectrum can be solved with a 2D harmonic parabolic confinement, and $E_{n,l} = (2n + |l| + 1)\hbar\omega_0$, for $\hbar\omega_0$: the electrostatic confinement energy, n : the radial quantum number, and l : the angular momentum quantum number. When we consider the electron transport conditions through the QD system, besides the energy level spectrum, the Coulomb repulsion among electrons also has to be taken into account when the total electron number, $N > 1$. The phenomenon that an electron needs to overcome this Coulomb repulsion energy to tunnel into the QD is called **Coulomb blockade (CB)** [57]. The constant interaction (CI) model generalizes both concepts of discrete levels and the Coulomb repulsion, which parameterizes the Coulomb interaction of an electron on the QD with a constant capacitance C as facing the environment and other electrons on dot. The details are in Appendix (B), and we calculate

1. The total energy of the dot, $U(N)$

2. The electrochemical potential, $\mu(N)$, which is defined as the energy of adding the N-th electron into the dot, and is the difference in the total energy of the dot containing N and (N-1) electrons, i.e.

$$\mu(N) = U(N) - U(N - 1)$$

3. The addition energy, E_{add} , the energy needed for adding one more extra electron into the system, is the summation of charging energy $E_c = e^2/C$, and the energy spacing between two discrete levels, ΔE .

$$E_{add} = \Delta E + E_c = \mu(N + 1) - \mu(N) = \Delta\mu(N)$$

We can express the allowing condition for the current flow via the QD as $\mu_s \geq \mu(N) \geq \mu_d$, where μ_s/μ_d stands for the electrochemical potential of the source/ drain electrode. There are two parameters affecting the electron transport: $\mu(N)$ for the dot, and μ_s/μ_d for the electrode, and both of them are controllable. As in Fig. 7.1 (f), the transport window opened by μ_s, μ_d is determined by eV_{sd} , or $\mu_s - \mu_d = eV_{sd}$; meanwhile, $\mu(N)$ can be tuned by V_g as mentioned in the second paragraph.

With the basic understanding of the above, we analyze or measure the current behaviors in the QD from Figs. 7.1 (d-h). First, in the simplest case $V_{sd} \approx 0$, a series of separated current peaks, or **Coulomb oscillation peaks**, shows up as applying continuously V_g (see Fig. 7.1 (d)). Figure 7.1 (e) is the corresponding situation of these peaks: only when $\mu(N)$ aligns with $\mu_s = \mu_d$, electrons are able to tunnel through the dot; the distance between the peaks is actually the addition energy, E_{add} . Second, if we apply a finite V_{sd} so that $eV_{sd} \geq E_{add}$ such as the condition in Fig. 7.1 (f), then the blockade will be

completely released. In Fig. 7.1 (g), we sweep V_{sd} at continuously different V_g to have the $V_{sd} - V_g$ diagram. Along the green line is the condition in Fig. 7.1 (e) and the blue spots are the condition in Fig. 7.1 (f). Since V_{sd} bias will partially cross on barriers and relatively tune $\mu(N)$, the blockade conditions are diamond-shape current-suppressed areas centered to the zero bias, and called to be **Coulomb diamond**. Alignments between $\mu(N)$ and μ_s or $\mu(N)$ and μ_d construct the edges or the boundary conditions of Coulomb diamonds (see Fig. 7.1 (h)). Notice that the size of every Coulomb diamond in Fig. 7.1 (g) [56] is actually different and especially large at $N = 2, 6, 12 \dots$. This arises from the atom-like property of the QD. Or specifically, the shell structure of the first few levels in a 2D atom is revealed -- 1s orbit allowing for 2 electrons, $2p^\pm$ (for 4 e^-), 3s and $3d^\pm$ (for 6 e^-).... Therefore, we can see that the addition energy is especially larger when the electron is going to occupy the next shell.

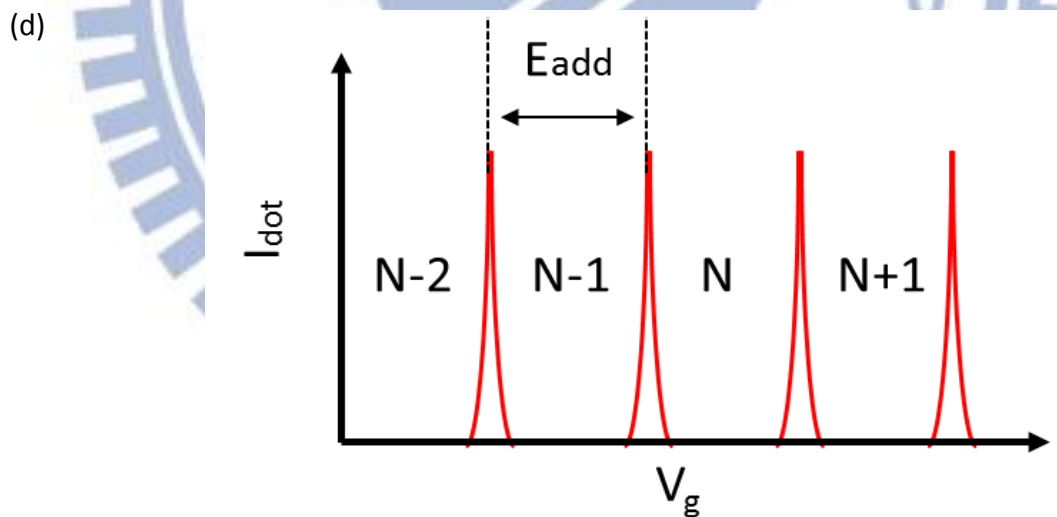
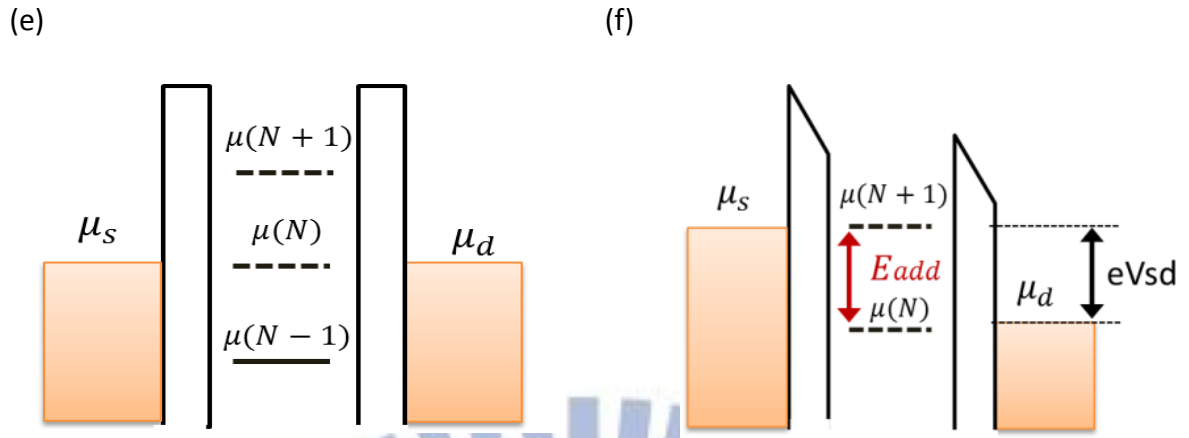


Fig. 7.1 (d) Coulomb Oscillations, the current peaks measured at $V_{sd} \approx 0$. The peaks only happens when $\mu(N) = \mu_s = \mu_d$, and we can tune $\mu(N)$ with V_g . The difference between the two neighboring peaks is the addition energy.



Figs. 7.1 (e-f) The schematic diagram for (e) Coulomb oscillation occurring (f) releasing the blockade situation as $eV_{sd} \geq E_{add}$.

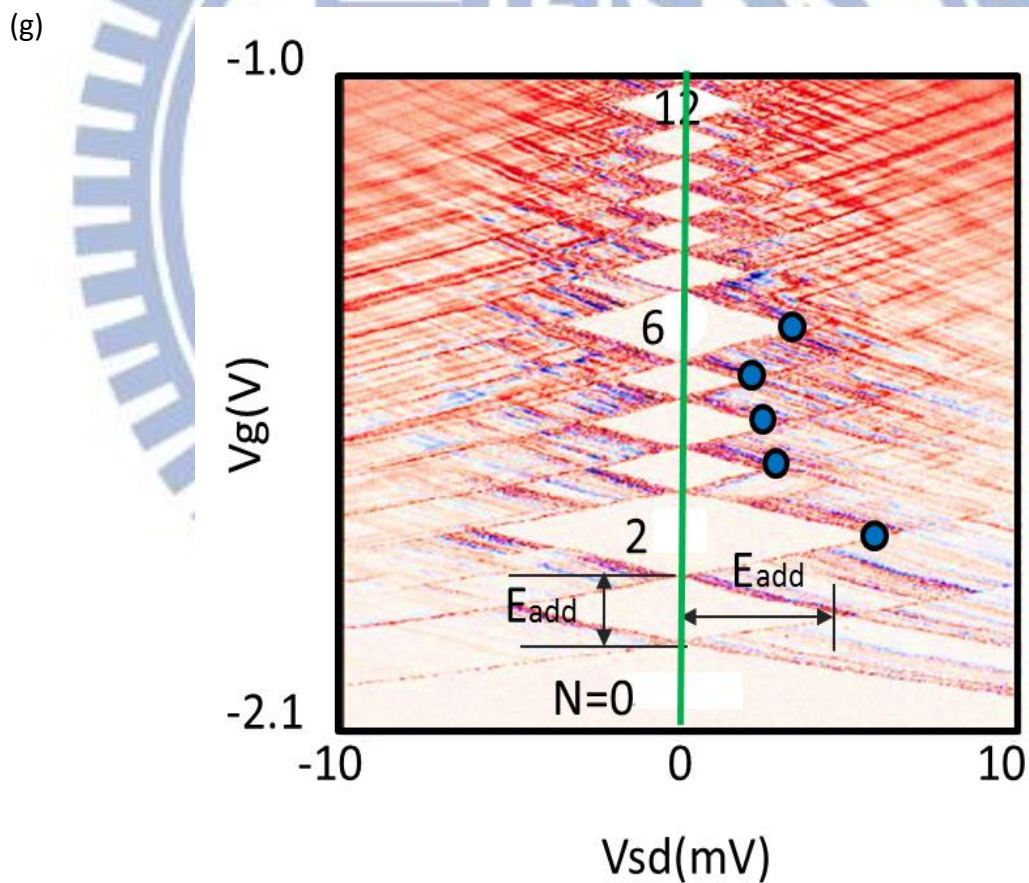


Fig. 7.1 (g) The measured Coulomb diamonds in the $V_{sd} - V_g$ diagrams revealing the shell structures of the dot [56].

(h)

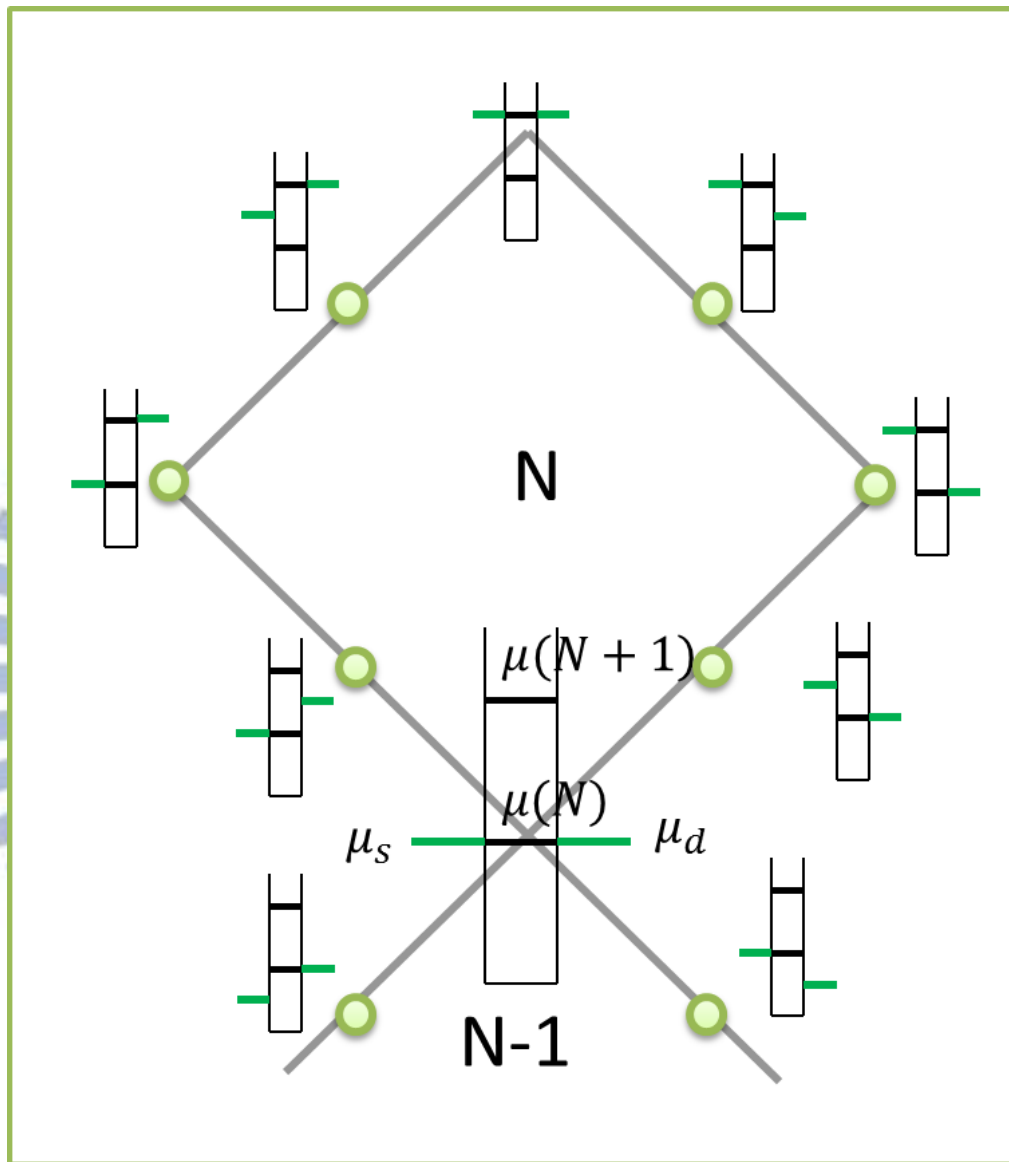
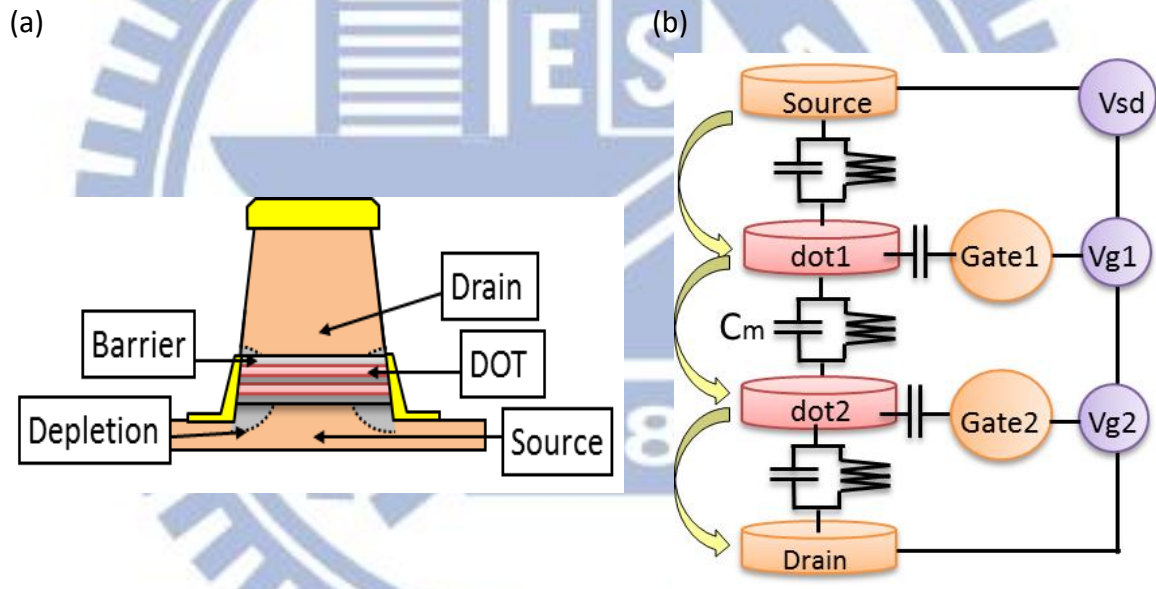


Fig. 7.1 (h) the Coulomb diamond boundary conditions are determined by the alignment of the chemical potential between either one of the lead and the dot, i.e. $\mu(N) = \mu_s$ or μ_d

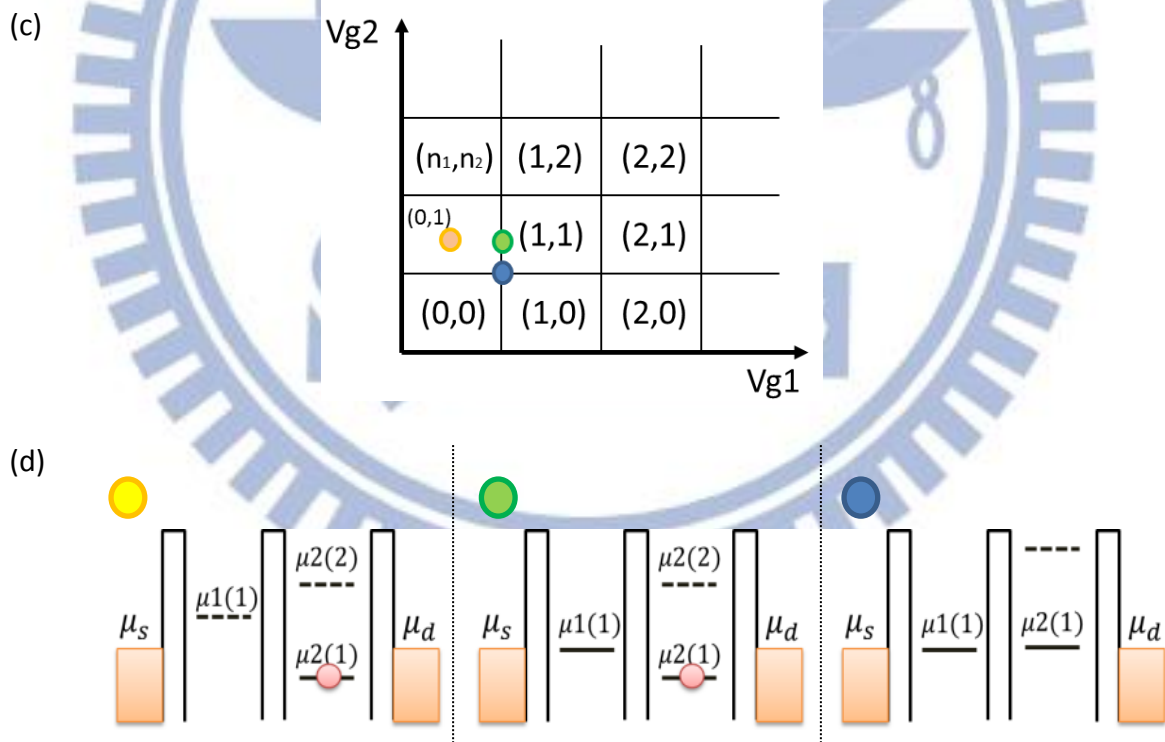
7.2 Vertical Double Quantum Dots

In our study, we choose the vertical double QDs to be our system. Comparing with the structure of the single QD, there is one more layer inset as center barrier as Fig. 7.2 (a). The CI model also suits for the double QD system with the equivalent circuit diagram shown in Fig. 7.2 (b) (see Appendix (C) for details). And now, besides there is one more extra QD needed to be considered, the Coulomb interaction crossing the dots such as the influence of the electron on one QD upon the other QD also plays an important role in the electron transport. And, we define this interdot Coulomb interaction as E_{cm} .



Figs. 7.2 (a-b) (a) A schematic diagram for a vertical double dot system in a crossing-section view. Two dots are separated and sandwiched by barriers, and their sizes are controlled by the depletion region due to Schottky gates, the drawn golden parts surrounding the dot side. (b) The equivalent circuits for the double vertical quantum dot system. Comparing with single dot as Fig. 7.1 (b), there is one more parameter as the interdot capacitance, which describes the interaction between dots due to the coupling, concluded.

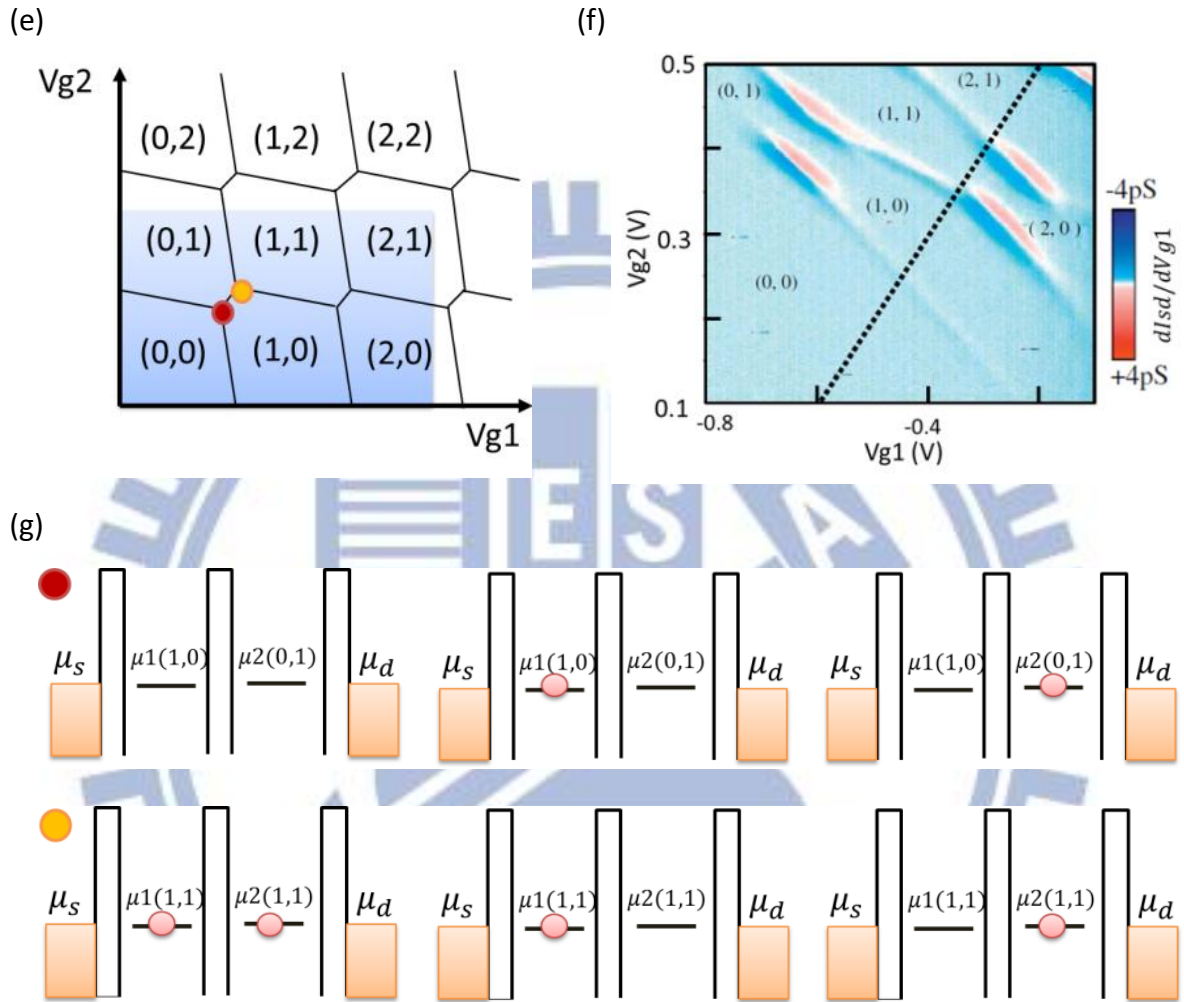
To realize the electric properties of double QDs, we can start from the **charge stability diagram**, which ignores the electron spin. Under the condition of $V_{sd} \approx 0$, we first assume that there is almost no coupling between two QDs, or interdot capacitance $C_m \approx 0$, so that the two gates can control $\mu(N)$ of each QD individually. Then, Coulomb oscillation (CO) peaks (see Sec. 7.1) can be expressed as a function of (V_{g1}, V_{g2}) as in Fig. 7.2 (c). The horizontal/vertical black line means the alignment of $\mu_s (= \mu_d)$ and $\mu(n_1, n_2)$ of QD1/QD2, and the CO peaks occur at the crosses of black lines. Between the lines, electrons outside/inside the dots do not have enough energy to tunnel in/out of the system, and the label (n_1, n_2) indicates the number of trapped electron in each dot. To be more clearly, the corresponding diagrams in the chemical potential are shown in Fig. 7.2 (d).



Figs. 7.2 (c-d) (c) The charge stability diagram for double quantum dot systems. (d) Three corresponding level diagram w.r.t the colored circles in Fig. 7.2 (c). Here, we treat two dots as individual ones. Electrons can do the first-order tunneling only at blue point(s).

If two QDs couple with each other, or when we consider the cross coupling between gate 1(2) and dot 2(1), then not only applying the gate voltage of one dot will affect the other dot, but the charging of dot 1(2) will also change the electrostatic energy of dot 2(1). Therefore, the charge stability diagram in Fig. 7.2 (c) is deformed to be hexagonal as Figs. 7.2 (e-f) and also named to be “honeycomb diagram”. Now, the transport occurs at the joined points of triple lines like the pair of yellow and red circles in Fig. 7.2 (e); one is going through the electron transport, while the other goes like the hole transport. The corresponding diagrams of chemical potentials for transport are in Fig. 7.2 (g). In experiments, with the aim of the honeycomb diagram, we can detune the wanted experiment condition. Such as the Pauli spin blockade occurs at the transport cycle of $(0,1) \rightarrow (1,1) \rightarrow (0,2) \rightarrow (0,1)$, and we tune the gates to be along the dotted line in Fig. 7.2 (f) [69] to achieve the conditions.

Figure 7.2 (h) shows the schematic $V_{sd} - V_g$ diagram of a double dot system. In single QD (such as the inset of Fig. 7.2 (h) or Fig. 7.1 (h) in Sec. 7.1), the CB regions are constructed by pairs of boundary conditions as $\mu(N) = \mu_s$ and $\mu(N) = \mu_d$. For a double QD system, we can consider that there will be two pairs of $\mu(n_1, n_2) = \mu_s$ and $\mu(n_1, n_2) = \mu_d$. That is, two colored (red and blue) lines in Fig. 7.2 (g); one is for QD1, while the other is for QD2. It is under the consideration that electrons directly tunnel into or out from QD1/QD2 while treating QD2/QD1 as a thick barrier (i.e. cotunneling process). These two colored lines provide us the conditions where the first-tunneling process can really occur, i.e. the black lines, and further help us to analyze a measured $V_{sd} - V_g$ diagram.



Figs. 7.2 (e-f) The (e) schematic and (f) measured honeycomb diagrams [69] revealing the coupling between two dots. (g) Diagrams of corresponding chemical potentials of dots and leads at the colored circles in (e). Notice that along the line linking up the paired circles, states in each dot are tuned simultaneously and equally. Unlike Fig. 7.2 (c), the chemical potentials represented as $\mu_{1/2}(n_1, n_2)$ here are due to the interdot coupling.

(h)

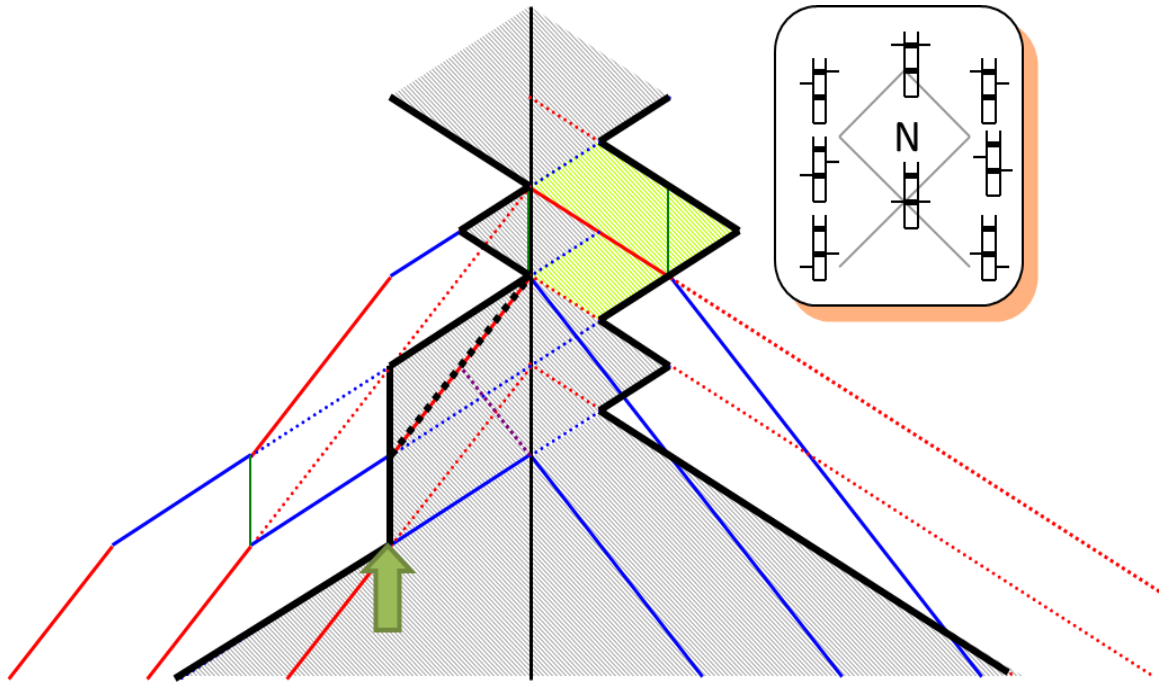


Fig. 7.2 (h) The $V_{sd} - V_g$ schematic diagram for the double dot systems. The block lines sketch the contours of blockade regions. Within the blockade area, red and blue lines show a second-tunneling process. The vertical lines indicate an offset between dots, or the offset number is revealed as the numbers of the vertical line.

A double dot system as in Figs. 7.2 (h-i), the $V_{sd} - V_g$ diagram may exhibit not only as the grey coulomb diamond shape similar to single dot systems, but also the vertical lines indicated by arrows. The vertical lines are due to an offset in the energy levels of two dots. This energy offset between two dots can be originally determined by the electron density of the source and drain when the device is made. Or, it can be detuned with different gate

voltages for systems with more than one gate. In vertical quantum dot systems, both of the composition of the chosen wafer and the micro fabrication process will affect the electron density of the electrodes, since it is believed [70] that a decrease in electron density in cylindrical mesa (drain) is higher than that in the substrate (source) during fabrication processes. The interpretative diagram for relative positions between electronic states when resonant current occurs for the double dot systems of offset = 1 are shown in Fig. 7.2 (j).

(i)

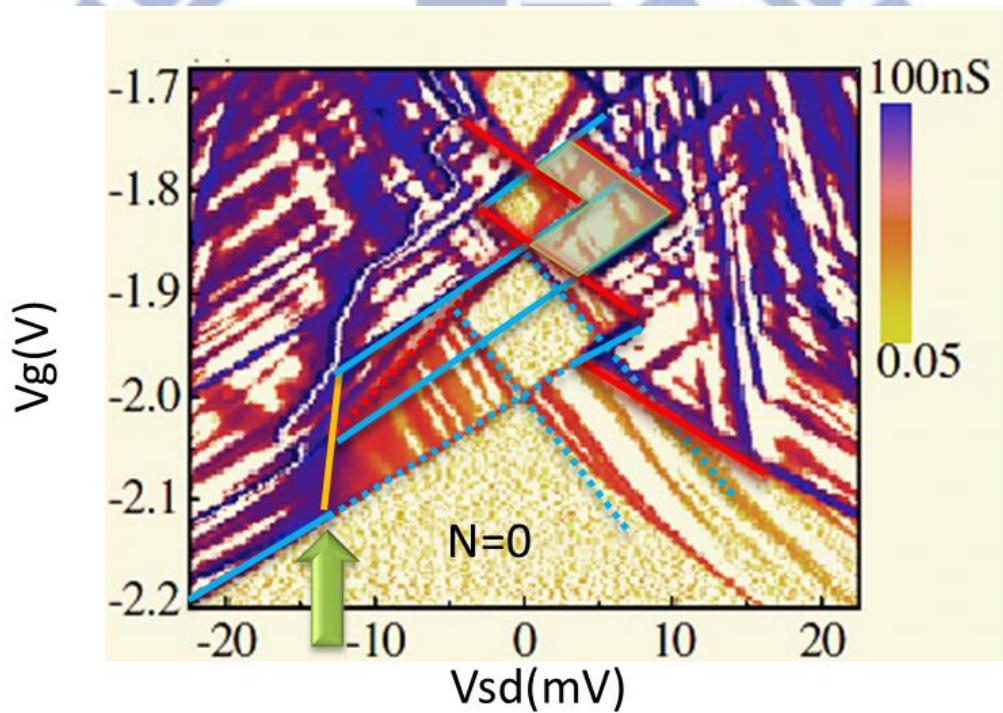


Fig. 7.2 (i) The measured $V_{sd} - V_g$ diagram of the double dot systems in dI_{sd}/dV_{sd} plots [71]. The vertical line indicates an offset = 1 and the corresponding positions of levels are in Fig. 7.2 (j).

(j)

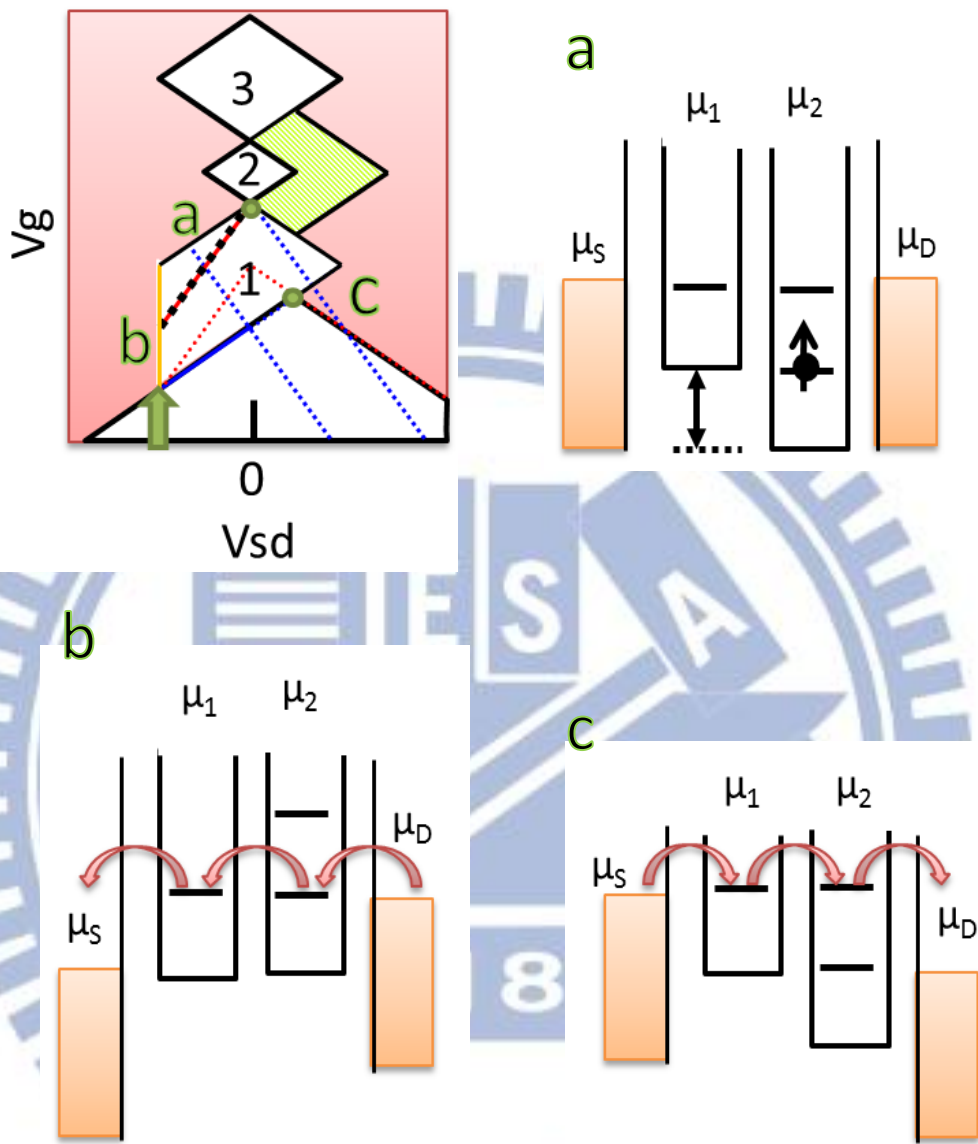


Fig. 7.2 (j) The corresponding energy level diagrams for a double dot system with inderdot offset = 1. At condition **a**, we can clearly see the energy difference between two dots. Condition **b** is along the vertical line, while **c** is at the kink side. For **b** electrons tunnel through the system via the two aligned ground states at an infinite source-drain bias, The applied gate voltages simultaneously and nearly equally tune states in both dots. Therefore, we have a vertical line, as the tunneling boundary, along the V_g axis.

7.3 Pauli Spin Blockade

Pauli spin blockade occurs in double QD systems during the electron transport cycle, $(0,1) \rightarrow (1,1) \rightarrow (0,2) \rightarrow (0,1)$ where (n_1, n_2) indicates the electron number in QD1 and QD2 [71]: once an electron tunneling into QD1 is with the spin direction the same as the electron originally trapped in QD2, the triplet spin state, $T(1,1)$, is formed and it may have trouble to tunnel into QD2. The $S(1,1)$ and $T(1,1)$ are nearly degenerate in energy, but $S(0,2)$ and $T(0,2)$ are not. As we know, the Pauli exclusion only allows two electrons with the opposite spin direction to share the same orbit, therefore the ground state 1s orbit of QD2 only has the singlet spin state, $S(0,2)$. The electron in QD1, which forms $T(1,1)$, cannot tunnel to the 1s orbit in QD2 to become $S(0,2)$ due to the spin conversion, whereas $T(0,2)$ that one of the electrons has to be at the first excited $2p+$ orbit may be too high in energy to be within the transport window opened by V_{sd} . so that results in the blockade (see Fig. 7.3 (a)).

In the $V_{sd} - V_g$ charge diagram, spin blockade (SB) demonstrates itself as an asymmetric current-suppressed region by the side of Coulomb blockade (CB) of the total electron number $N = 2$. As in Fig. 7.3 (b), SB occurs in the area enclosed by green lines, whereas electrons tunnel via $(0,1) \rightarrow (0,2) \rightarrow (1,1) \rightarrow (0,1)$ on the opposite bias side. The current in the blue color area is ~ 100 pA and is about 1 pA in the red color region (of the SB area and also the cotunneling area). And we can calculate the life time of the triplet spin state, $T(1,1)$, for $I = e/t$ where e is elementary charge. The $T(1,1)$ lifetime, or the lifting of SB, can be influenced by the spin-orbit interaction [72, 73], the hyperfine interaction [63, 66, 74] and electron spin resonance [60, 62]; once SB is lift, the situation goes back to be in Fig. 7.3 (a) until SB takes place again.

When we apply V_{sd} , the bias will drop on the three barriers, and detune the energy levels between dots at the same time. Within the SB region in the Fig. 7.3 (d), we have current for $V_{sd} \gtrsim 9$ mV : once the detuning due to applied V_{sd} is large enough to

compensate the energy difference between $T(1,1)$ and $T(0,2)$, SB will be completely released, and we see the electron flowing again. The schematic diagram to show this triplet tunneling channel (i.e. $(0,1) \rightarrow T(1,1) \rightarrow T(0,2) \rightarrow (0,1)$) developing with increasing V_{sd} is shown in Fig. 7.3 (c). The situation for $V_{sd} <$ the threshold voltage is SB, while for $V_{sd} >$ the threshold voltage, the current flow through the system with the “inelastic” interdot tunneling. As a result, what we see is a current peak marked by the arrow in Fig. 7.3 (d) where $T(1,1)$ just aligns with $T(0,2)$.

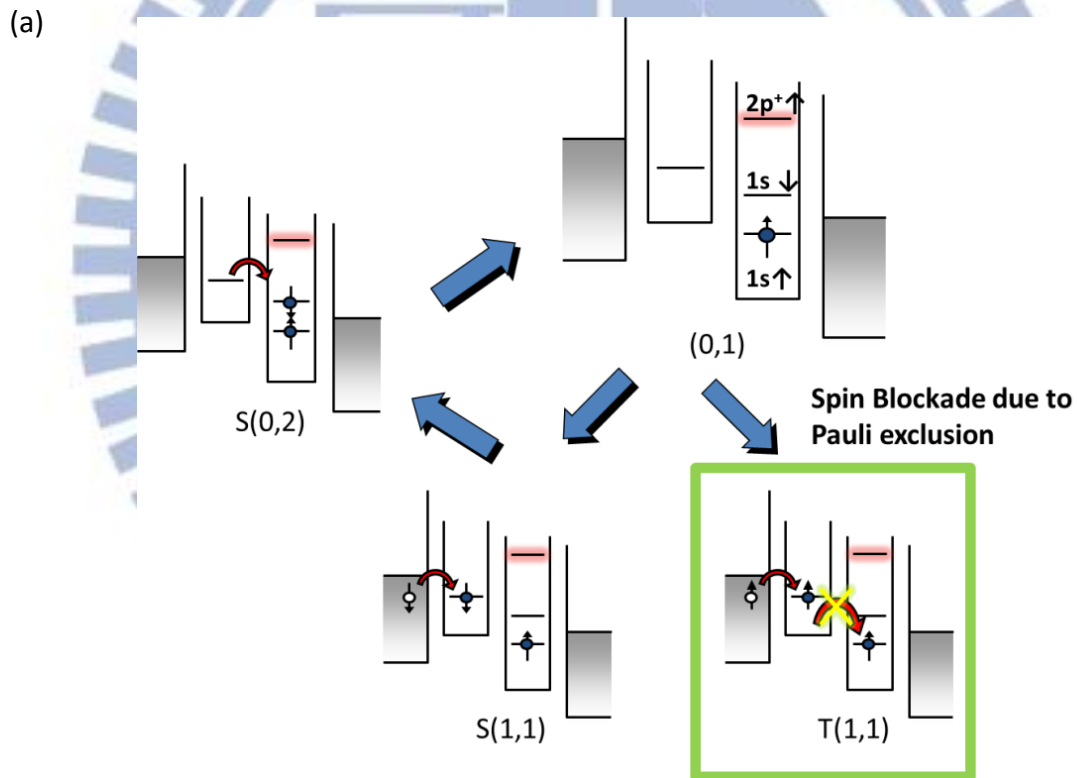


Fig. 7.3 (a) Schematic level diagrams of the Pauli spin blockade: During the $(0,1) \rightarrow (1,1) \rightarrow (0,2) \rightarrow (0,1)$ cycle, $(1,1)$ has both probability to be either spin singlet or triplets, so the electron may transport until SB will eventually occurs.

(b)

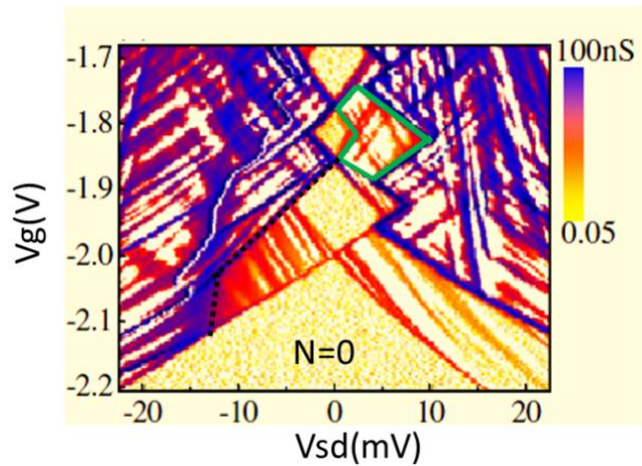


Fig. 7.3 (b) In the $V_{sd} - V_g$ diagram, SB shows an asymmetric current suppressed region at $N=2$ as the area green lines enclose. The small current in other red color region is due to the co-tunneling process [71].

(c)

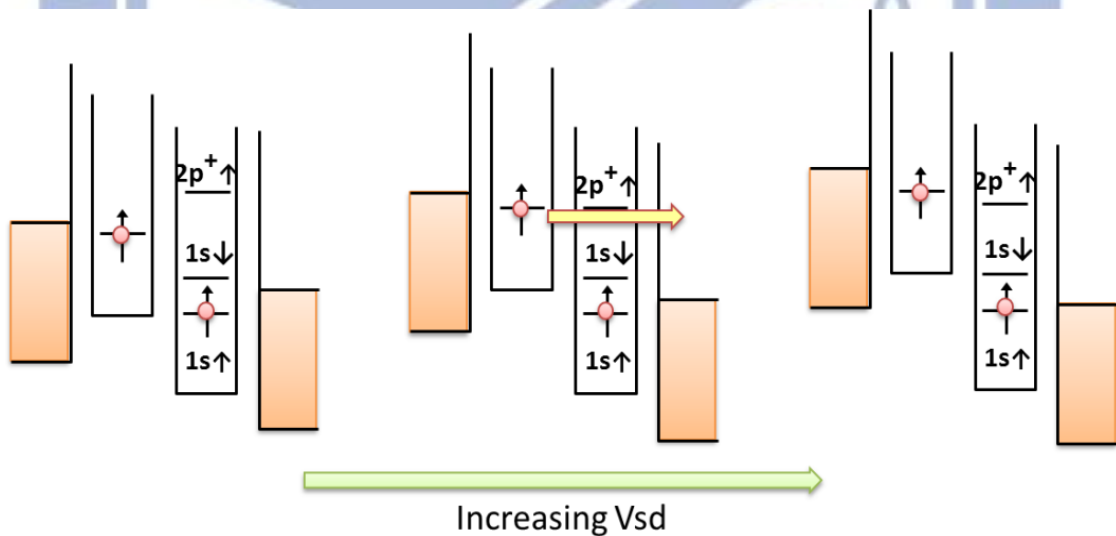


Fig. 7.3 (c) The schematic diagram of the triplet tunneling channel developed by applying V_{sd} . The V_{sd} bias crossing on three barriers tunes the relative energy between the dots. The energy difference between $T(1,1)$ and $T(0,2)$ is compensated by a finite and large enough V_{sd} bias, and release the spin blockade.

(d)

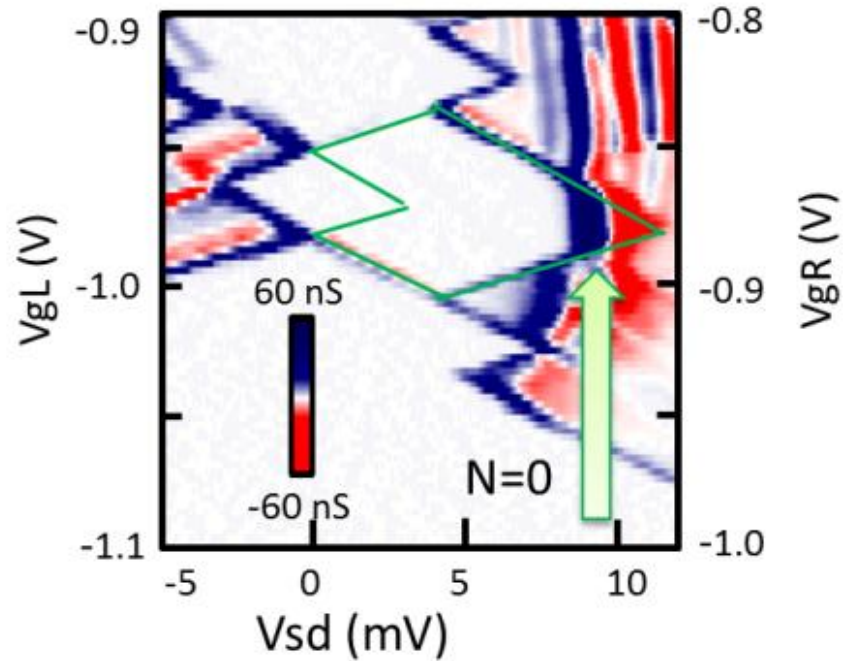


Fig. 7.3 (d) Spin blockade in the $V_{sd} - V_g$ diagram. A triplet tunneling channel developed at high bias as the arrow marks.

7.4 The Two-Electron Energy Diagram

The relative energy between the two-electron states including $S(1,1)$, $T(1,1)$, $S(0,2)$ and $T(0,2)$ plays a determinant role in the occurrence of SB. Hence in this section, we introduce the two-electron energy diagram.

At first, we consider $S(0,2)$ and $T(0,2)$ which are the same as the one-dot two-electron states. Remember that in Sec. 7.1, the energy spectrum of the disk-like shaped QD is $E_{n,l} = (2n + |l| + 1)\hbar\omega_0$. $S(0,2)/T(0,2)$ here means the situation that two electrons both occupy the ground state(1s orbit)/ one electron stays in the ground orbit while the other is at the first excited state(2p orbit). Therefore, we write down the addition

energy for these respective states **under low magnetic fields** as

$$S(0,2) = E_{0,0} + Ec = \hbar\omega_0 + Ec$$

$$T_0(0,2) = E_{0,1} + Ec = 2\hbar\omega_0 + Ec$$

$$T_+(0,2) = E_{0,1} + Ec + Ez = 2\hbar\omega_0 + Ec + g\mu_B B$$

$$T_-(0,2) = E_{0,1} + Ec - Ez = 2\hbar\omega_0 + Ec - g\mu_B B$$

Notice that the CI model is only available in low magnetic fields, and under this condition we can assume the Coulomb interaction is a constant value as Ec , and is the same for $S(0,2)$ and $T(0,2)$; Ez represents the Zeeman splitting term. In our QD system, the confinement energy $\hbar\omega_0$ is of meV order, while the Zeeman term is several μeV , thus the energy difference between $S(0,2)$ and $T(0,2)$, E_{st} , can be estimated to be around $\sim meV$.

For two electrons residing in QD1 and QD2 respectively, they could form either $S(1,1)$ or $T(1,1)$. The energy difference between the two states, J , depends on the coupling between the two dots, tc . According to G. Burkard *et al.* [75], J estimated in Hubbard approximation would be equal to $4tc^2/Ec$. In Fig. 7.4 (a), we put this four states, $S(1,1)$, $T(1,1)$, $S(0,2)$ and $T(0,2)$, together to see their relative values. We assume the simplest case that tc and the magnetic field, B , is small enough to have degenerated $T(1,1)$ and $S(1,1)$, and Zeeman terms in spin triplet $T(0,2)$ can be ignored. The detuning axis is the inter-dot energy difference, which becomes larger as applying higher V_{sd} . Since $S(1,1)$ and $T(1,1)$ have one electron in each dot, the detuning to lift the states in QD1 up while pull down the states in QD2 will make no difference on the energy of $(1,1)$ states. However, it will result the $(0,2)$ states lower with increasing detuning. Note that J and E_{st} are kept, since they are the function of tc , and ΔE respectively.

To understand SB, we can separate Fig. 7.4 (a) into three regions:

1. If we set the same orbit levels in each dot nearly align, the system keeps in Coulomb blockade.
2. To increase V_{sd} so that the detuning is larger enough to overcome the charging energy, then we can see the spin blockade phenomenon.
3. Further applying higher V_{sd} , the energy difference between $T(1,1)$ and $T(0,2)$ can be compensated and SB is released.

The real system case is in Fig. 7.4 (b). Due to the interdot coupling, $(0,2)$ and $(1,1)$ will hybridize with each other, so the intersections in Fig. 7.4 (a) turns to be anti-crossings, and lead the energy difference between $(1,1)$ and $(0,2)$ to have the maximum value of $2\sqrt{2}tc$.

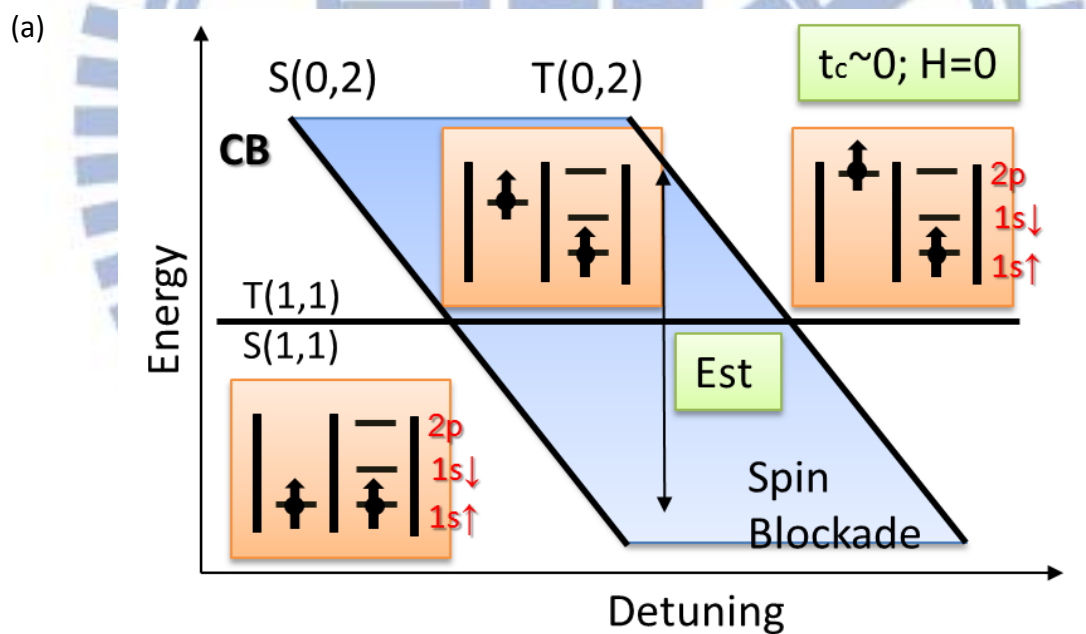


Fig. 7.4 (a) The Energy levels of two-electron states in double QDs as a function of detuning under the conditions of $t_c \sim 0$; $H = 0$. For $H = 0$, we can ignore the Zeeman splitting terms in triplets. The hybridized states are formed at the crossing of singlets and triplets due to the coupling t_c .

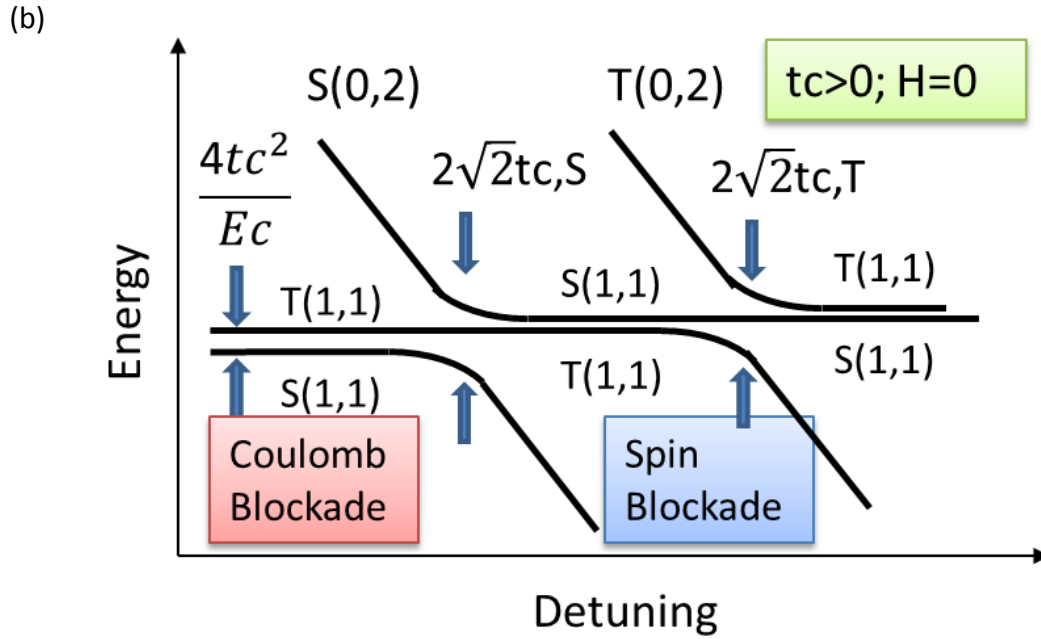


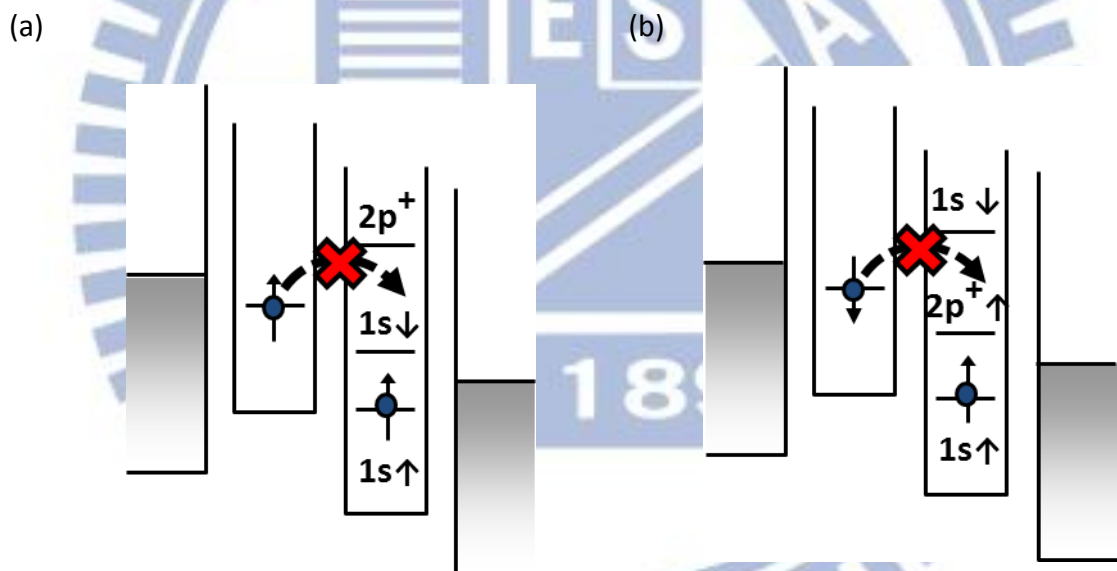
Fig. 7.4 (b) The Energy levels of two-electron states in double QDs as a function of detuning under the conditions of $tc > 0$; $H = 0$

7.5 Introduction to the Singlet Spin Blockade

In this section, we propose a mechanism to achieve the singlet spin blockade (SSB) in a double QD device in our system.

In the Pauli spin blockade, electrons forming $S(1,1)$ can tunnel through the system via the doubly occupied ground state $(0, 2)$ as spin singlet, whereas electron spin triplets $T(1,1)$ are blocked for $T(0,2)$ being outside of the bias window. The singlet spin blockade, on the contrary, is the phenomenon where the electronic transport blocks at electron spin singlet but not at spin triplets. Figures 7.5 (a-b) show the schematic diagrams of the Pauli spin blockade and the singlet spin blockade. In this thesis, we demonstrate the singlet spin

blockade by performing the singlet-triplet transition of the doubly occupied ground state in one of the dots (or QD2 in Sec. 7.3) under high magnetic field: we first find an optimized condition for exhibiting the Pauli spin blockade under zero magnetic field; then, while keeping the interdot offset the same (offset=1) with two gate voltages [67, 79, 81](or the ground state (0,2) always tune to be aligned up with (1,1) of the same spin configuration), we increase the magnetic field until the two-electron ground state in the second dot goes beyond the singlet-triplet spin transition to have the singlet spin blockade.



Figs. 7.5 (a-b) Schematic diagrams for the mechanism of (a) a conventional Pauli spin blockade and (b) a singlet spin blockade.

7.6 The Singlet-Triplet Transition

in a Two-Electron Quantum Dot

In this chapter, we describe the electron transport behavior with the constant interaction mode, which assume that the Coulomb interaction can be treated to be constant, while the discrete energy spectrum of a single particle on the dot is not affected by the interactions. However, in our experiments, we apply high magnetic fields to a system with two electrons. The high magnetic field means that there is an additional confinement affecting the discrete levels, and not to mention that the Coulomb interaction between two electrons now is not that simple to be a constant. That is, the CI model is no longer suitable here. Therefore, we explain the how the magnetic field plays a role in our system, especially on the two-electron states.

First, the Fock-Darwin spectrum [76] describes the variation of the **single-particle energy levels**, which means the complicated many body interaction or the electron-electron interaction can be avoided, **under magnetic fields** in a system of a 2D parabolic confining potential of $V(r) = \frac{1}{2} m^* \omega_0^2 r^2$. Ignoring the Zeeman splitting and the energy can be described to be

$$E_{n,l} = (2n + |l| + 1) \hbar (\omega_0^2 + \frac{1}{4} \omega_c^2)^{1/2} - \frac{1}{2} l \hbar \omega_c$$

where n stands for the radial number, l is angular momentum and $\hbar \omega_c = \hbar * eB/m^*$ is the cyclotron energy. Figure 7.2 (a) shows the Fock-Darwin spectrum of $\hbar \omega_0 = 3 \text{ meV}$ [57].

(a)

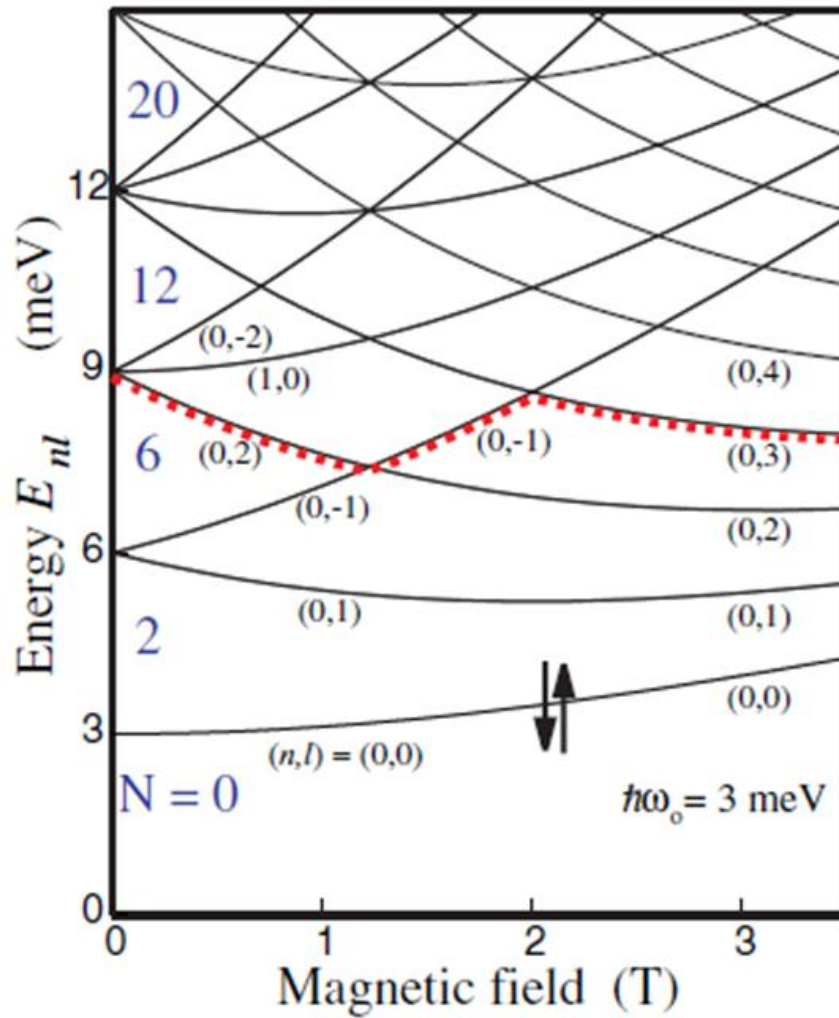


Fig. 7.6 (a) The Fock-Darwin spectrum describes a single electron within a 2D parabolic confinement under magnetic fields. At high magnetic field, the Landau levels are formed as marked $(n, l) = (0, 0), (0, 1), (0, 2), (0, 3), \dots$. Note that the spin degeneracy is ignored here [57].

(b)

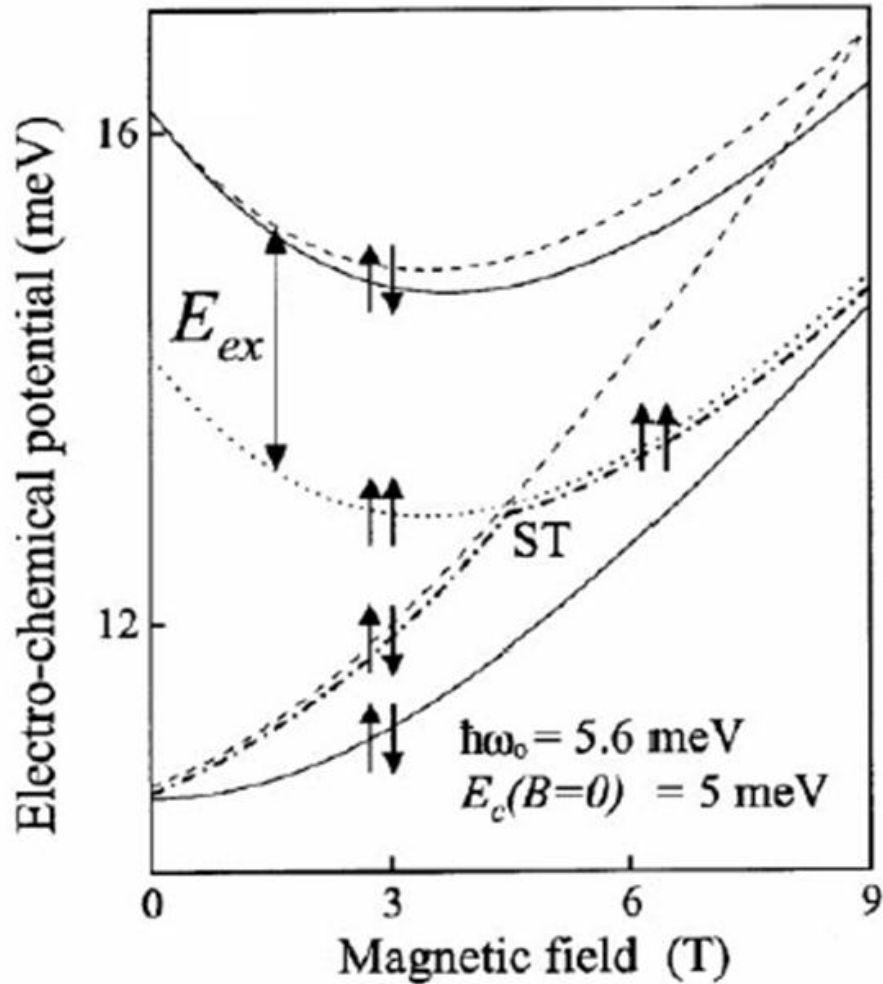


Fig. 7.6 (b) The calculated electrochemical potential μ of a two-electron dot as a function of magnetic field for $\hbar\omega_0 = 5.6 \text{ meV}$, $E_c = 5 \text{ meV}$ at 10 T: The lower solid curve is the ground state (GS), while the upper one is the excited state (ES). Dashed lines represent the situation involving the B-dependent Coulomb interaction. Due to the larger overlap of W.F. when both electrons staying in GS, the dashed line of GS grows faster than that of ES. The upper dashed curve with subtraction of a constant exchange energy results in the dotted curve. The GS, before and after the S-T transition, is indicated by a dashed-dotted line [77].

For the two-electron states, we can first simply consider the first two lowest states to be two electrons staying at the ground (0,0) state of the Fock-Darwin spectrum, while the first excited state is one at (0,0) state and the other at (0,1) state. Then, the total energy of the system at will be

Ground state: $E = 2E_{0,0} = 2 (\omega_0^2 + 1/4 \omega_c^2)^{1/2}$

1st excited state: $E = E_{0,0} + E_{0,1} = (\omega_0^2 + 1/4 \omega_c^2)^{1/2} + 2(\omega_0^2 + 1/4 \omega_c^2)^{1/2} - 1/2 \hbar\omega_c$

However, the above is actually the non-interacting particle case. We have to further consider the magnetic field dependent charge energy between two electrons. That is,

Ground state: $E = 2E_{0,0} + Ec(B)$

1st excited state: $E = E_{0,0} + E_{0,1} + Ec(B)$

The $Ec(B)$ term plays an important role in two-electron energy states. As in the Fock-Darwin spectrum, the single-particle level spectrum is a function of the magnetic field. For two electrons sharing the same $1s$ orbit ground state, which is the singlet state according to the Pauli exclusion, the wave function (W.F.) of the electron state shrinks in the radial direction with increasing magnetic fields. This leads to the Coulomb interaction we consider now progressively strengthens due to the less spatial extension of the wave function. At the same time, the energy of the $2p^+$ orbit is decreased, because its angular momentum is favored in the field. Thus, as enlarging the magnetic fields, the singlet and the triplet will approach to each other. Eventually at a certain magnetic field, the two electrons change their occupation from the orbit of $1s^2$ to that of $1s2p^+$ as the calculated result in Fig. 7.6 (b) [77]. Owing to the exchange Coulomb interaction between electrons in $1s$ and $2p^+$, the spin triplet is the ground state for $1s2p^+$, so we have the singlet-triplet transition (the S-T transition) as

the ground state orbit becomes $1s2p^+$ from $1s^2$. In a vertical double QD systems with a 2D harmonic confinement of ~ 5 meV, the ground-state transition occurs at the magnetic field of ~ 5 T, and the exchange splitting between the $1s2p^+$ triplet state and the $1s2p^+$ singlet excited state is ~ 2.5 meV [77, 78]. The singlet-triplet transition phenomenon has been previously observed in single dot systems [56, 77] as such in Fig. 7.6 (c).

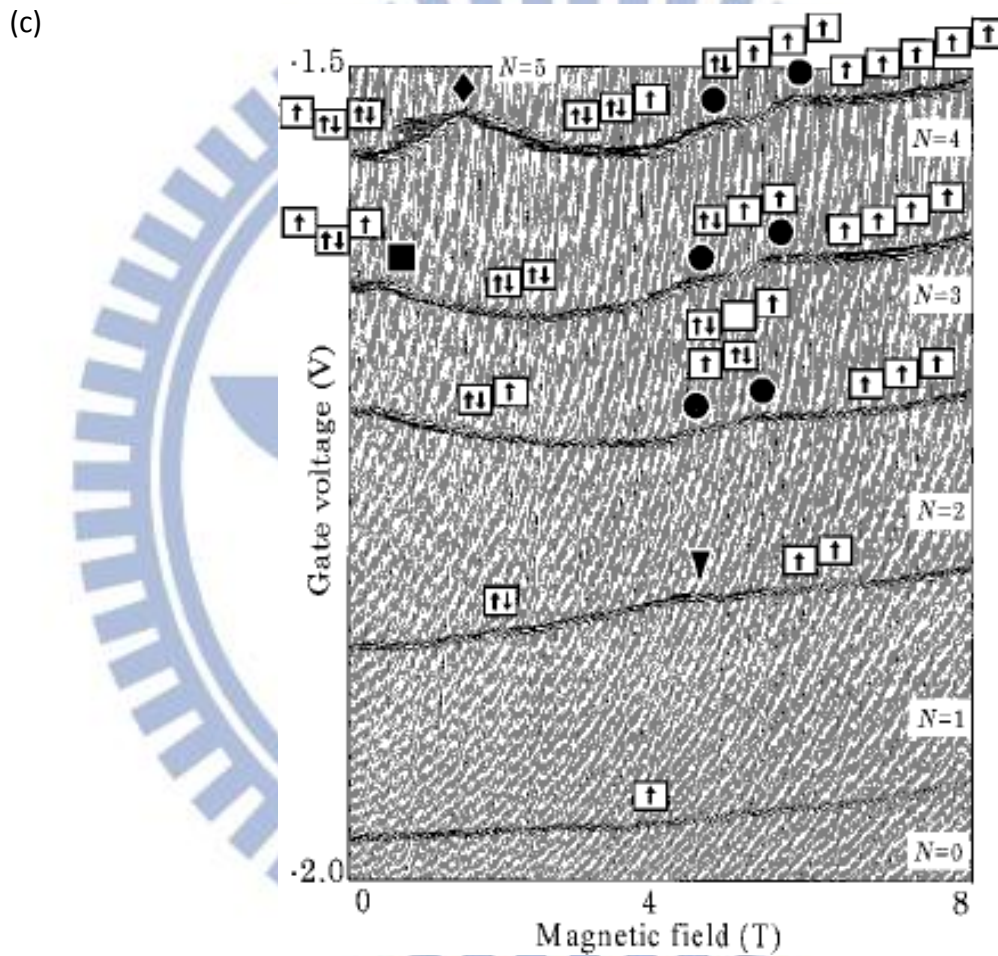


Fig. 7.6 (c) Plot of $I_{sd}(V_g, B)$ measured in a single QD system with $V_{sd} = 0.1$ meV which is so small to show only the ground states (of $N = 1$ to 5). For $N = 2$, the ground-state transition is marked with a triangle. The spin configurations, indicated with the arrows, show the transition from spin singlet to be spin triplet as gradually applying the magnetic field from 0 to 4.15 T. Note that the system gains additional exchange energy when the spins of two electrons are parallel [56].

Chapter 8

Device Fabrication and Experimental Setups

8.1 Structure of Devices

In this work, we employ two-gate attached vertical double semiconductor quantum dots as our system. The system acts as a field-effect transistor with source, drain and gates, and is composed of a triplet barrier heterostructure [81], $\text{Al}_{0.22}\text{Ga}_{0.78}\text{As} / \text{In}_{0.05}\text{Ga}_{0.95}\text{As} / \text{Al}_{0.22}\text{Ga}_{0.78}\text{As} / \text{In}_{0.05}\text{Ga}_{0.95}\text{As} / \text{Al}_{0.22}\text{Ga}_{0.78}\text{As}$. The bandgap of AlGaAs is larger than InGaAs, so that double quantum wells can be formed separately between the three barriers. The triplet barrier structure is clipped by gradiently n-doped GaAs layers, i.e. the source and drain electrodes. The bottoms of the conduction band of the wells are lower than the Fermi energy of n-AlGaAs. Hence, electrons from electrode contacts may flow to the wells until the equilibrium in electrostatic potential is reached as the schematic diagram of Fig. 8.1 (a) (Note: the doping of indium in GaAs would further reduce the bottom of conduction band.) The relevant parameters of the wafer are listed in Table 3.

The tunnel barrier has a limit requirement that $R_t \gg h/e^2 = 25.8 \text{ k}\Omega$, where the R_t is the tunneling resistance which can clearly define the electrons to be either in the leads or in dots. The Heisenberg uncertainty tells us that $\Delta E \Delta t \geq h$, and here Δt is the

charge/discharge time $R_t C$ (C represents the capacitance of the dot), and the uncertainty energy ΔE should be much less than charging energy $E_c = e^2/C$ for observing the quantized charge. Therefore, when designing a QD system, $(e^2/C)R_t C \geq \Delta E \Delta t \geq h$ or $R_t \gg h/e^2 = 25.8 \text{ k}\Omega$ is the basic requirement.

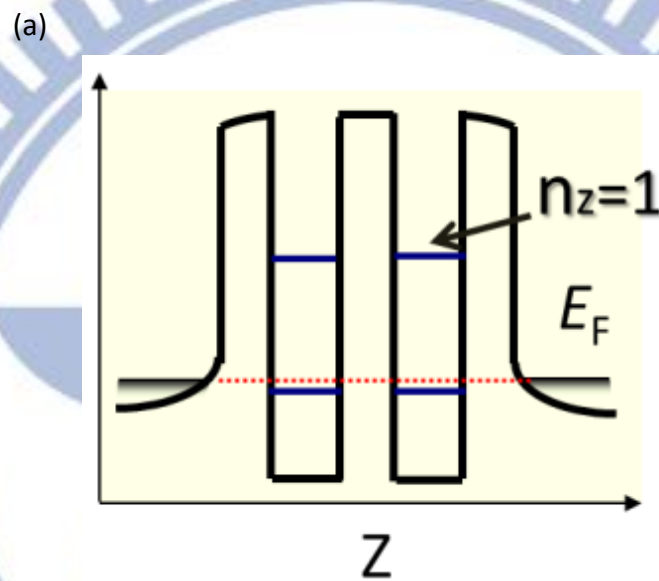


Fig. 8.1 (a) Schematic energy diagram of a double QD device where only the ground state in the z -direction occupied. The equilibrium in electrostatic potential among the electrodes and well is reached.

Table 3 Relevant parameters of the wafer used in our double QD device

Structures		Parameters	
Materials	Thickness(Å)	Doping Concentration (cm ⁻³)	Al(In) ratio
N-GaAs	70	2.0X10 ¹⁸	-
Si	0		-
N-GaAs	25	2.0X10 ¹⁸	
N-GaAs	175	2.0X10 ¹⁸	-
N-GaAs	1800	2.0X10 ¹⁷	-
N-GaAs	1500	1.4X10 ¹⁷	-
N-GaAs	700	1.2X10 ¹⁷	-
GaAs	30	-	-
AlGaAs	70	-	0.22
InGaAs	120	-	0.05
AlGaAs	80	-	0.22
InGaAs	120	-	0.05
AlGaAs	70	-	0.22
GaAs	30	-	-
N-GaAs	700	1.2X10 ¹⁷	-
N-GaAs	1500	1.4X10 ¹⁷	-
N-GaAs	1800	2.0X10 ¹⁷	-
N-GaAs	5000	2.0X10 ¹⁸	-
GaAs Substrate	600 μm		

8.2 Device Fabrication

Main processes of fabricating a vertical double QD device will be illustrated in this section, but we leave the details in Appendix (D): As the wafer is prepared (see Fig. 8.2 (a)), the materials of the QDs/barriers and thicknesses of barriers are already decided and we continuously construct a 0D structure with electrodes and gates. The schematic figures of fabricating devices are in Figs. 8.2 (b-f). Firstly, we deposit Ti(20 nm)/Au(200 nm), used as the bottom contact and the top electrode, on the substrate via photolithography and electron beam lithography, respectively. To contract the cylindrical structure, we continue to do dry etching. During this process, part of metal films and most of semiconductor are removed, but those covered by previously deposited Ti/Au will be left. We use BCl₃ plasma to etch down the wafer, and the embryo pillar structure is formed. Next, we use wet etching till the total etching depth is underneath the triplet barrier structure layers. The sulfuric acid etches all the semiconductor parts for several hundred angstroms but not the deposited metal. Therefore, the pillar is reduced in diameter, and this makes the following deposited Ti(20 nm)/Au(100 nm) layers, surrounding the pillar as gates, will not contact the top electrode too easily during the evaporation. After all the above processes, the vertical QDs system is indeed accomplished. However, for the electric transport measurement purpose, we need to further build the contact accesses from the device to the outside world. That is, we evaporate metal pads for wire bonding as the photos shown in Figs. 8.2 (g-j).

(a)

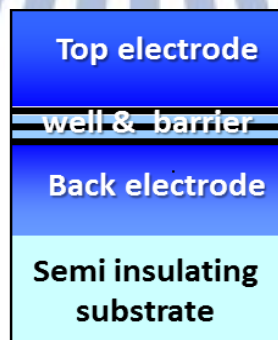
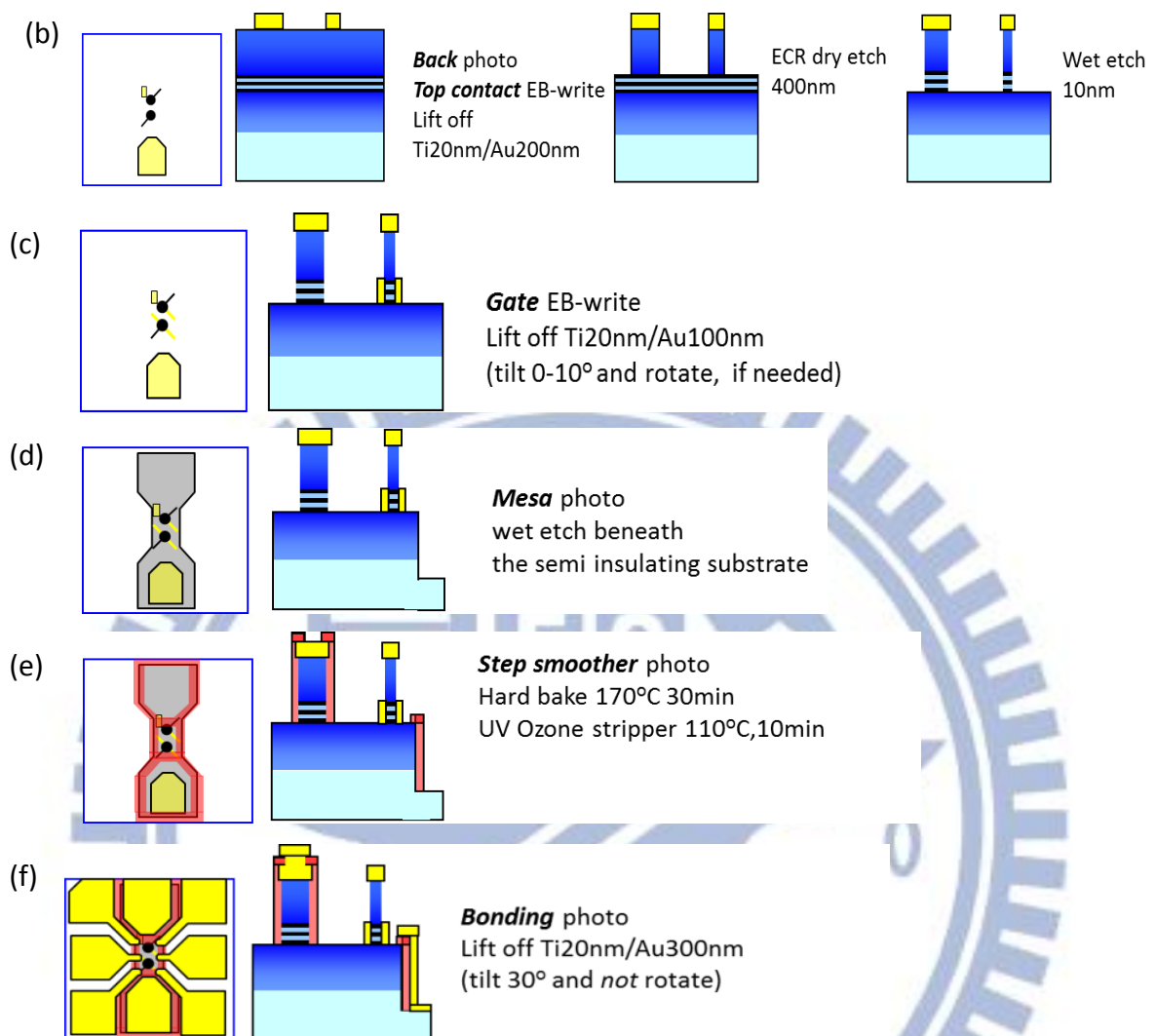
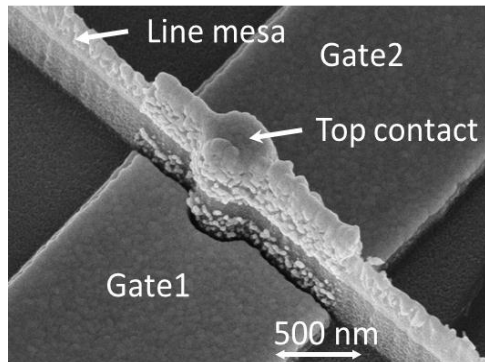


Fig. 8.2 (a) A simplified diagram for the wafer structure as in Table 3.

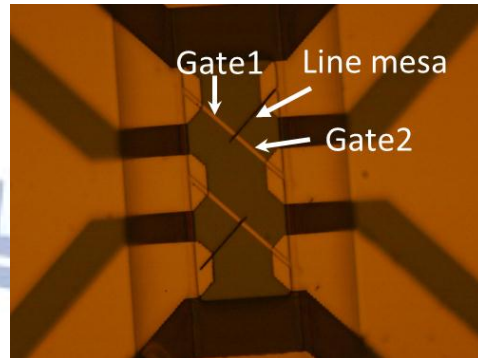


Figs. 8.2 (b-f) The main fabricating process in both aerial view and cross-section figures. (b) The first cross-section figure shows the deposited Ti/Au bottom and top contact. Titanium here is used for bonding metal electrodes and the substrate more tightly. The second and third cross-section figures are steps for the pillar structure. The dry etching process is to “sculpt” the pillar shape and the following wet etching further lessen semiconductor parts of the pillar in width and in depth until beneath the layers of three barrier structures. (c) Evaporating the metal gates around the pillar. (d-f) are steps for the contact pads for wire bonding. In (d), we use wet etching beneath the semi-insulating substrate; (e) step smoother with hard bake resist; (f) evaporating the metal contacts.

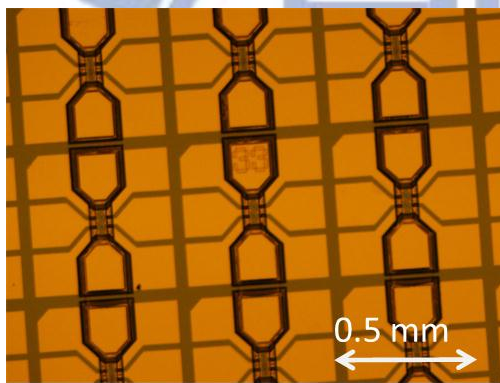
(g)



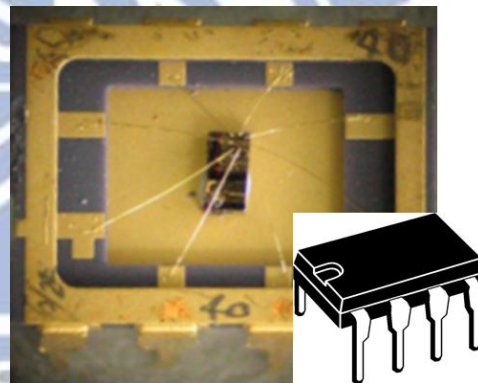
(h)



(i)



(j)



Figs. 8.2 (g-j) Photos of device similar with our samples. (g) A SEM image of a double-gate vertical QD device. (h) A image under optical microscope; two devices are included. (i) Contact pads for wire bonding. (j) A sample wire bonding to a chip carrier.

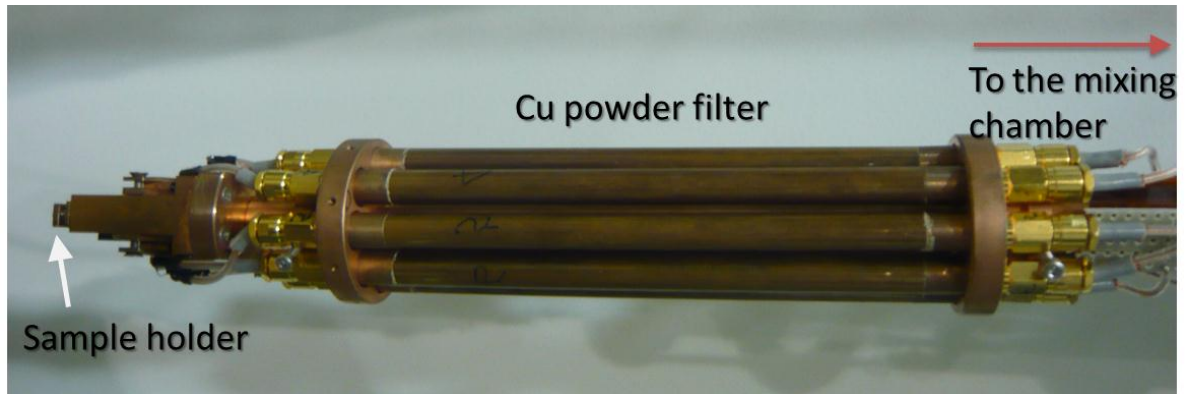
8.3 Low Temperature Measurement

All our experiments are performed at low temperature. There are two characteristic energy scales in the quantum dot systems, the charging energy E_c and the discreteness in

energy states. To observe those in the transport behaviors, the thermal energy should be well below the energy scales of the dots, i.e. $k_B T \ll E_c$. Thus, after examining all the samples in a cryostat capable to reach 1.5 K, we measured the selected suitable ones in a dilution refrigerator with a base temperature of ~ 40 mK with an Oxford IPS 120-10 superconducting magnet providing a magnetic field, which is along the z-direction of the sample or perpendicular to the barriers, up to 16 T.

In our experiments, the effective electron temperature is around ~ 0.5 K. In order to avoid the electron heating, the filters and the shielding room are used to attenuate the noise which is one of the sources causing heating. Besides normal RC filters utilized as low pass filters, Cu-powder filters (see Fig. 8.3 (a)) are launched between the sample holder and the mixing chamber of the fridge. As in the Fig. 8.3 (b), we fill winding Manganin wire and Cu powder into 100mm-long Cu tube with 10mm in diameter to make these filters. The Manganin wire is composed of Cu (86%), Mn (12%) and Ni (2%) and twists like “ ∞ ” as in Fig. 8.3 (b). The resistance of wire and the capacitance between wires and Cu powers works as an effective RC filter which can remove the high frequency of \sim GHz ranges.

(a)



(b)



Figs. 8.3 (a-b) (a) Copper powder filters, which can work well as a low pass filter even at low temperatures, are launched between the sample holder and mixing chamber of the fridge (b) The structure of the copper powder filter.

Chapter 9

Results and Discussions

In this chapter, we demonstrate the results of the singlet spin blockade occurring at high magnetic field in a two-electron vertical double QD device. We first explain the *experiment conditions* in our experiment in [Sec. 9.1](#). Then, *the two-electron excitation spectrum* is followed in [Sec. 9.2](#). In [Sec. 9.3](#), the agreement between the two-electron excitation spectrum and the range where *the current-suppressed phenomenon takes place in the $V_{sd} - V_g$ diagram* further supports the occurrence of the singlet spin blockade in our device. Finally, we discuss *the spin singlet lifetime due to random nuclear spin fluctuation* in [Sec. 9.4](#). This is consistent with *a leakage current* of ~ 10 pA order we observed *in SSB*.

9.1 Experimental Conditions

As mentioned in [Sec. 7.5](#), under zero magnetic field, we first find an optimized condition for the Pauli spin blockade; then, we demonstrate the singlet spin blockade by performing the singlet-triplet transition of the doubly occupied ground state in one of the dots.

In [Ref. \[61\]](#), *Ono et. al.* shows the development of a triplet channel in the SB region from 0 to 5 T as in [Fig. 9.1 \(a\)](#). Following this measurement, if we can adjust the detuning to align the ground state of (0,2) and (1,1) with the same spin configuration at different magnetic fields, then it is predicable that the threshold bias, where the resonance tunneling current

via the triplets take places, will approach to the zero bias as increasing the magnetic field. And eventually, the SB region will disappear or completely “be covered” when the S-T transition occurs. If we continuously enlarge the magnetic field higher than where the S-T transition occurs, then what will happen? From Chap. 2, we know that $S(0,2)$ will be higher and away from the ground state $T(0,2)$. For $S(1,1) \approx T(1,1)$ in energy and the ground $T(0,2)$ state detuned to align up with $T(1,1)$, the $S(0,2)$ now may be out of the transport window and leads to the blockade again. Thus, the spin blockade area shall appear again, and the current peak position deviates from $V_{sd} \sim 0$ along with the increasing magnetic field until it completely moves off the spin blockade region. Notice that the spin blockade now is owing to the formation of $S(1,1)$ instead of $T(1,1)$. The figure 9.1 (b) shows the ability of detuning the interdot offset with two gates in our device.

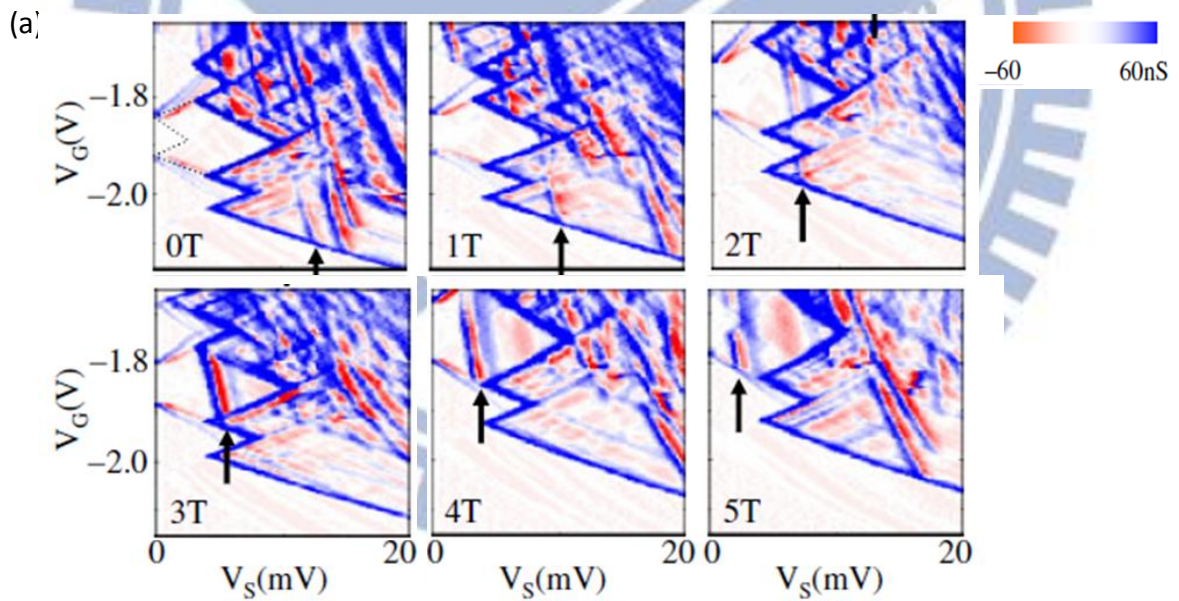


Fig. 9.1 (a) dI/dV_{sd} plots under magnetic field from 0 to 5 T. The Spin blockade region is indicated by the dotted line at 0 T. The triplet channel which collapses the spin blockade is marked by arrows. With increasing the magnetic field, the triplet channel enters into the SB region and approaches to the zero bias, but the CB is still left [61].

(b)

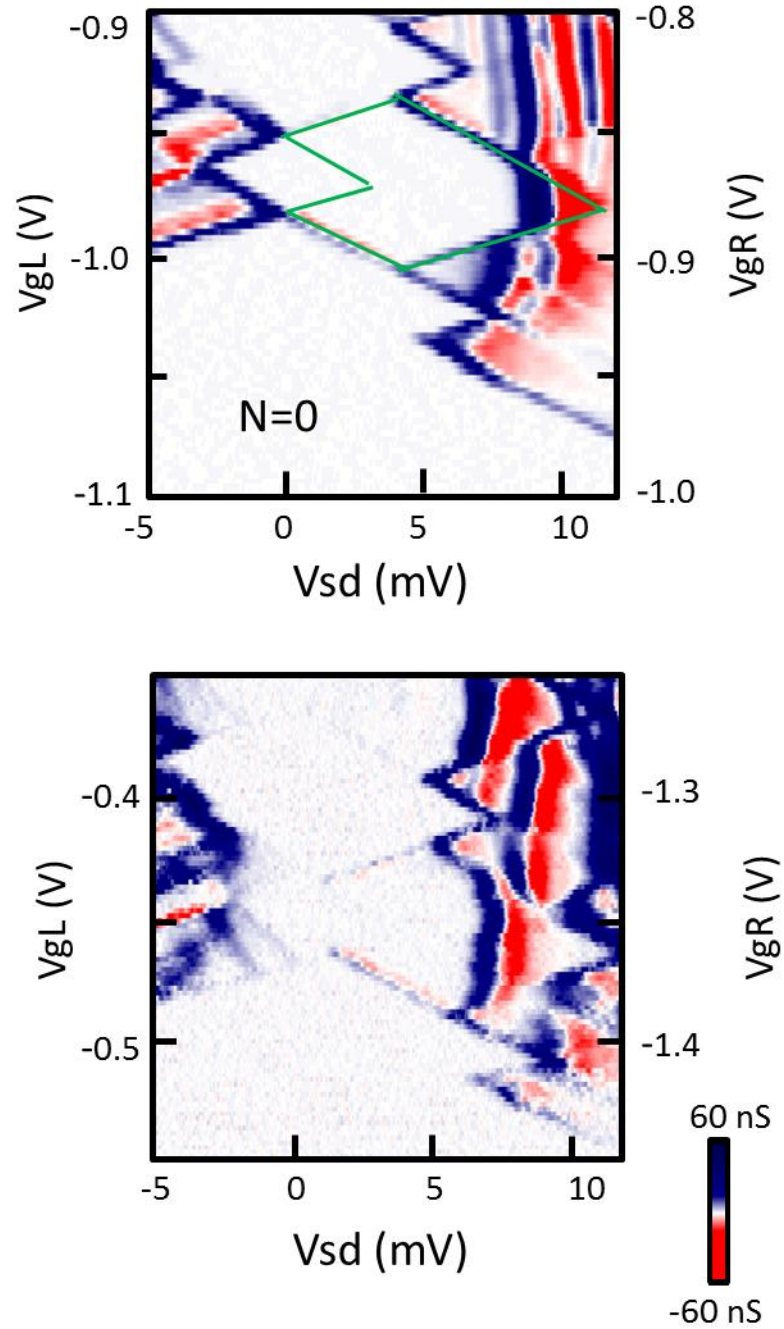


Fig. 9.1 (b) The $V_{sd} - V_g$ diagrams measured at 0 T with different gate conditions. The upper diagram shows the offset=1 case where $\mu_1(1,1) = \mu_2(0,2)$, whereas $\mu_1(1,1) > \mu_2(0,2)$ at the underlying diagram. These two diagrams demonstrate the ability to detune the interdot offset in our device.

9.2 The Two-Electron Excitation Spectrum

Similar to the measurement in Fig. 7.6 (c) where the single quantum dot with two electrons shows the singlet-triplet ground-state transition in magnetic fields [56], we measure the current strip by sweeping gate voltages, V_{gL}/V_{gR} , under various magnetic fields from 0 to 10 T with fixed $|V_{sd}| = 4$ mV (see Fig. 9.2 (a)), and the result is in Fig. 9.2 (b).

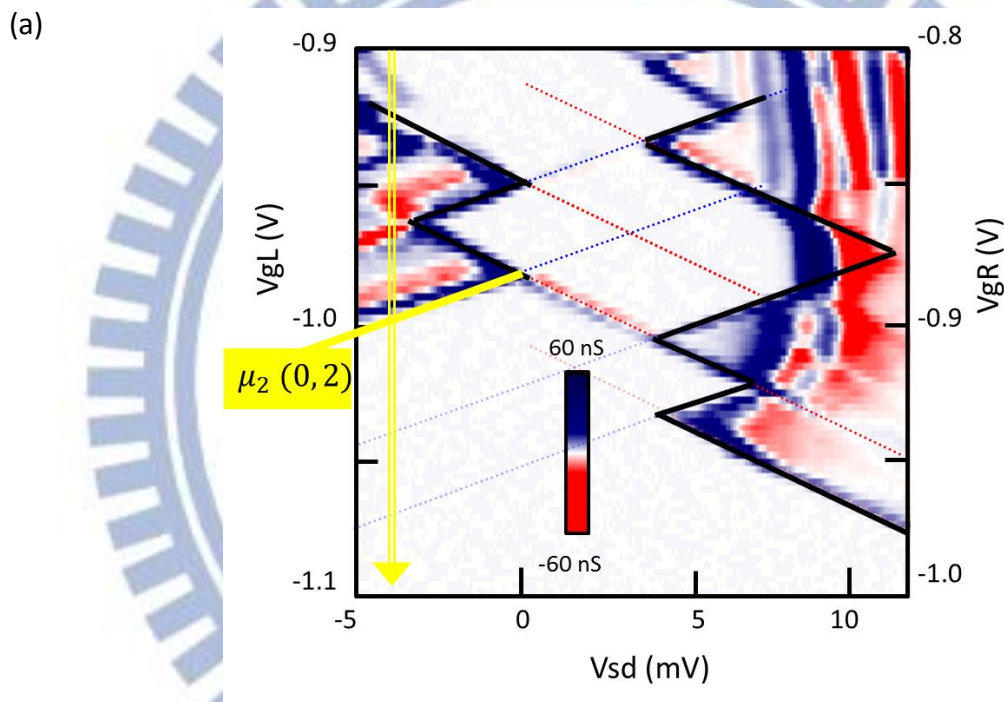


Fig. 9.2 (a) The Coulomb diamond diagram at 0 T. To measure the two-electron state energy spectrum, we sweep gate voltages along the yellow arrow to trace the variation of chemical potential of (0,2) states from 0 to 10 T, and the result is shown in Fig. 9.2 (b). The yellow line indicated $\mu_2(0,2)$ is the ground (0,2) state before the S-T transition.

In Fig. 9.2 (b), the $1s^2$ orbital S(0,2) state (indicated by the solid line) and the $1s2p^+$ orbital T(0,2) state (dashed line) are clearly resolved and show the ground-state transition at 5 T. Another excited state appears for $H > 7$ T (dotted line), and undergoes the second

ground-state transition at 9 T. This state is suggested to be the spin singlet state with high angular momentum [82]. The energy difference between the triplet ground state and the singlet excited state reaches to be maximum at ~ 7.5 T. Zeeman splitting was not observed owing to the expected small g -factor of our device. All these behaviors are consistent with previous experimental results in vertical single-dot devices [56, 77].

(b)

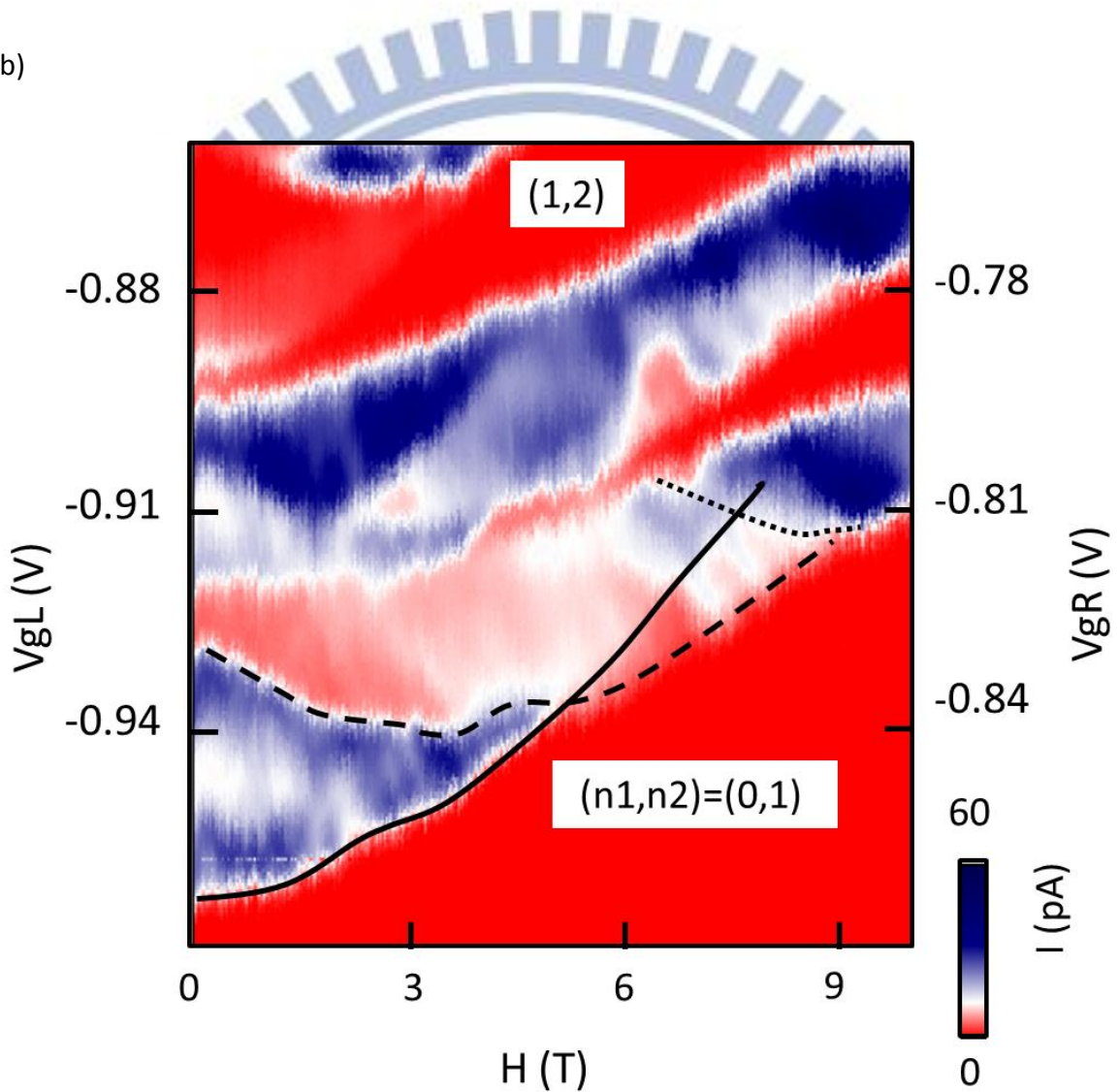


Fig. 9.2 (b) The excitation energy spectrum for $(0,2)$ states, measured at $V_{sd} = -4$ mV. The first current strip exhibits the $(0,2)$ state evolution among the solid line of the $1s^2$ orbital $(0,2)$ state with spin singlet, the dashed line of the $1s2p^+$ orbital $(0,2)$ state with spin triplet, and the dotted line for another $(0,2)$ state with spin singlet.

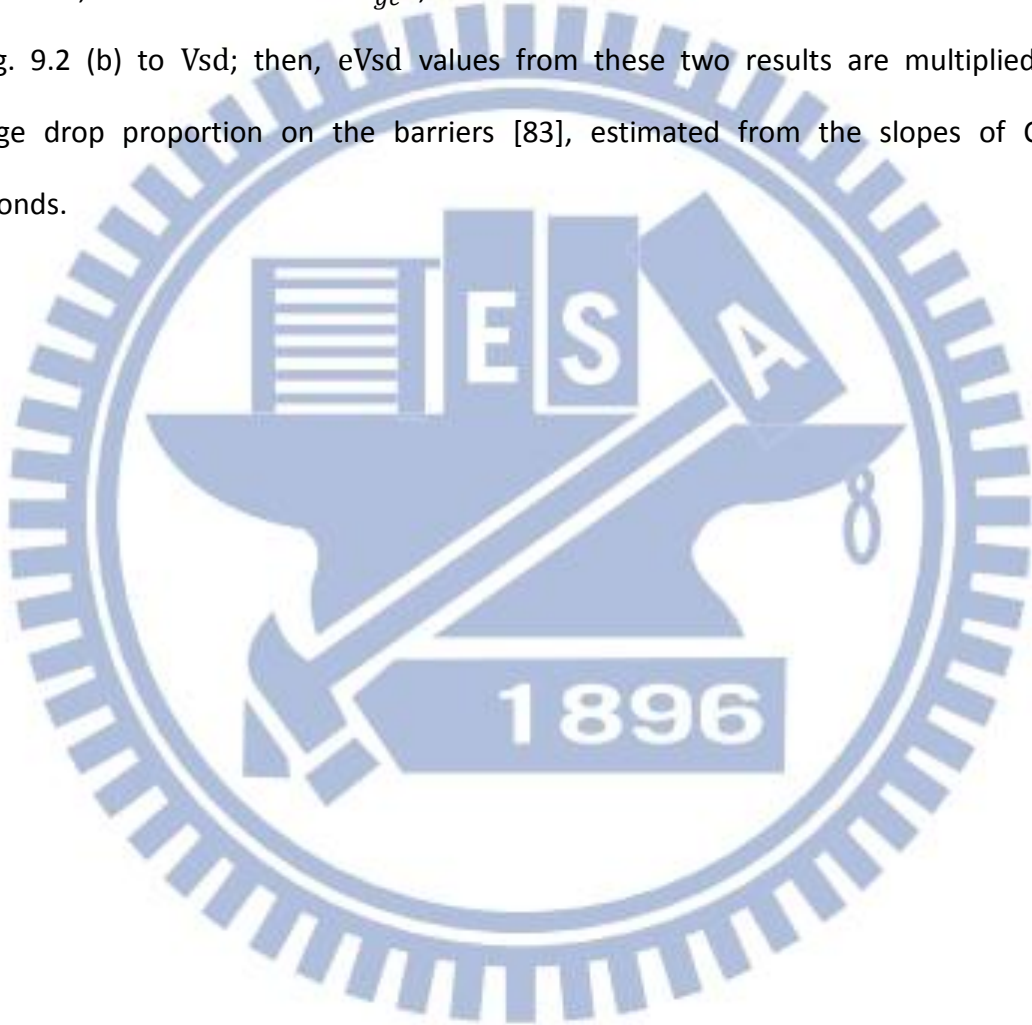
9.3 Spin Blockade in the V_{sd} - V_g Diagram under Magnetic Fields Going through the Singlet-Triplet Transition

The Coulomb diamond in an intensity plot of differential conductance, dI_{sd}/dV_{sd} , is measured from 0 to 9 T, and Figs. 9.3 (a-f) show data taken at the condition before, during and after the S-T transition.

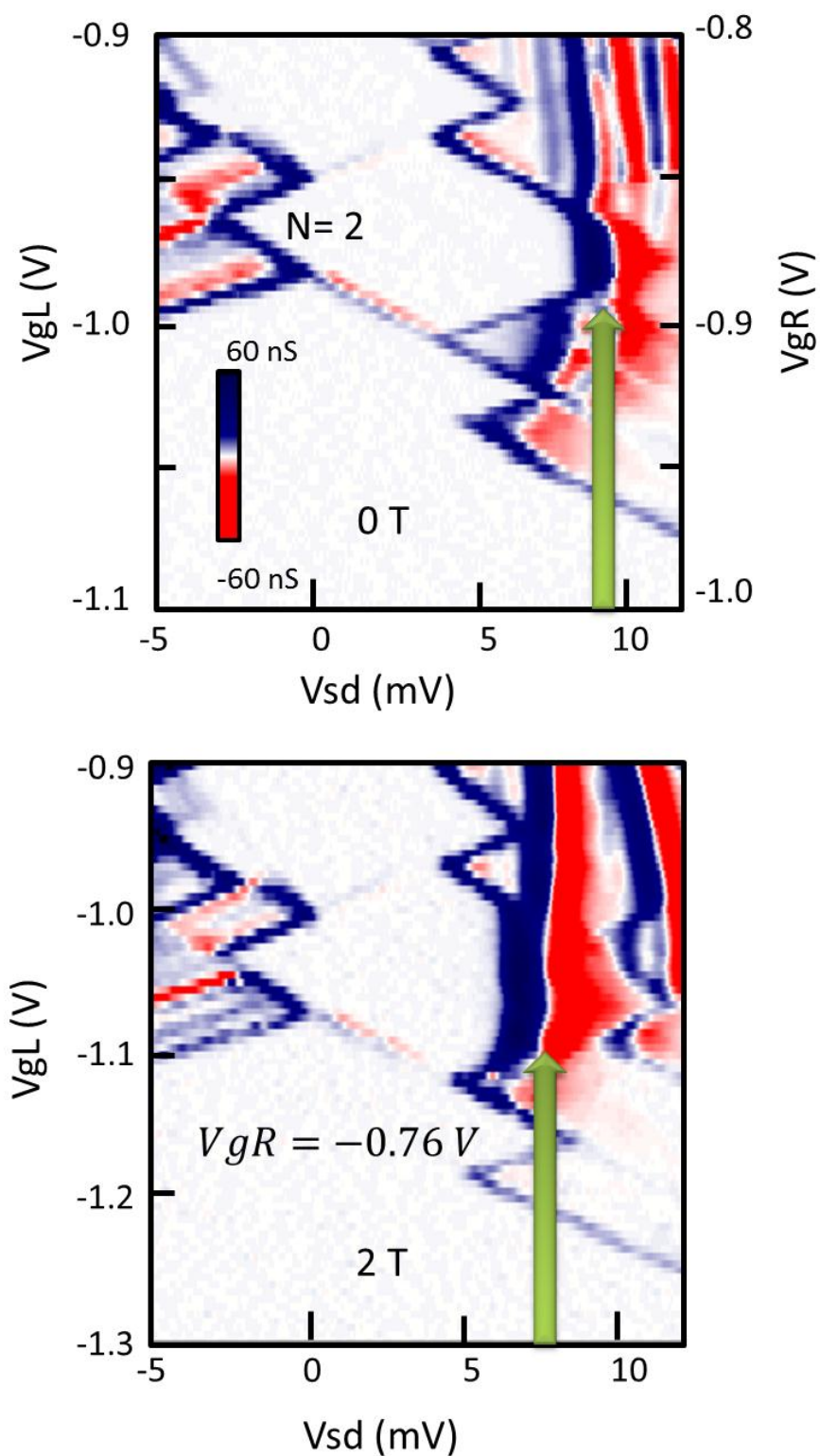
Begin with Fig. 9.3 (a) measured at 0 T, the SB appears on the positive V_{sd} side of the Coulomb diamond with the total electron number $N = 2$. The right corner of the SB region is partially cut by a current threshold that runs nearly parallel to the vertical axis and is indicated by an arrow. The current-carrying cycle for triplet states, $T(1,1) \rightarrow T(0,2) \rightarrow (0,1)$, takes place under this condition as previous studies. We also see a “current peak line” appears at two borders: between the SB region and the $N = 1$ Coulomb blockade region and between the SB region and the $N = 3$ Coulomb blockade region. SB is relieved on these two borders for $T(1,1)$ aligned with the Fermi energies of the source and drain electrodes, respectively. In all measurements in the $V_{sd} - V_g$ diagram, we tuned both V_{gL} and V_{gR} , so that the current peak lines touch $V_{sd} = 0$ in the dI_{sd}/dV_{sd} .

Corresponding to Sec. 9.1, increasing the magnetic field yet further before the S-T transition, the current threshold (due to $T(1,1) \rightarrow T(0,2)$ tunneling) indicated with arrows in Figs. 9.3 (a-c) shifts to a lower V_{sd} , and the current-suppressed area due to SB is decreased. At 5.0 T, near the S-T transition, the SB region completely disappears and leaves only the $N = 2$ Coulomb blockade region. Here at this time, both $S(1,1)$ and $T(1,1)$ can tunnel into $(0,2)$ states. Further increasing the magnetic field to be at the condition after the S-T transition, Coulomb diamond data again show the current threshold, which implies tunneling into an $(0,2)$ excited state (indicated by arrows in Figs. 9.3 (e-f)). We observed that the current threshold shifts to a higher V_{sd} with further increasing magnetic field. However, this threshold becomes blurred and difficult to trace for $H > 8.4$ T.

Both results of the (0,2) excitation spectrum (Fig. 9.2 (b)) and V_{sd} values at the current threshold (Figs. 9.3 (a-f)) give the magnetic-field-dependent energy difference between the ground and excited (0,2) states, ΔE_{ge} [56, 71]. We summarized them in Fig. 9.3 (g) using circles and triangles, respectively, and the results are nearly identical. This agreement confirms that SSB can take place in the range below the current threshold for $H > 5$ T. Notice that, in order to have ΔE_{ge} , we first convert the difference in the vertical V_g axis in Fig. 9.2 (b) to V_{sd} ; then, eV_{sd} values from these two results are multiplied by the voltage drop proportion on the barriers [83], estimated from the slopes of Coulomb diamonds.

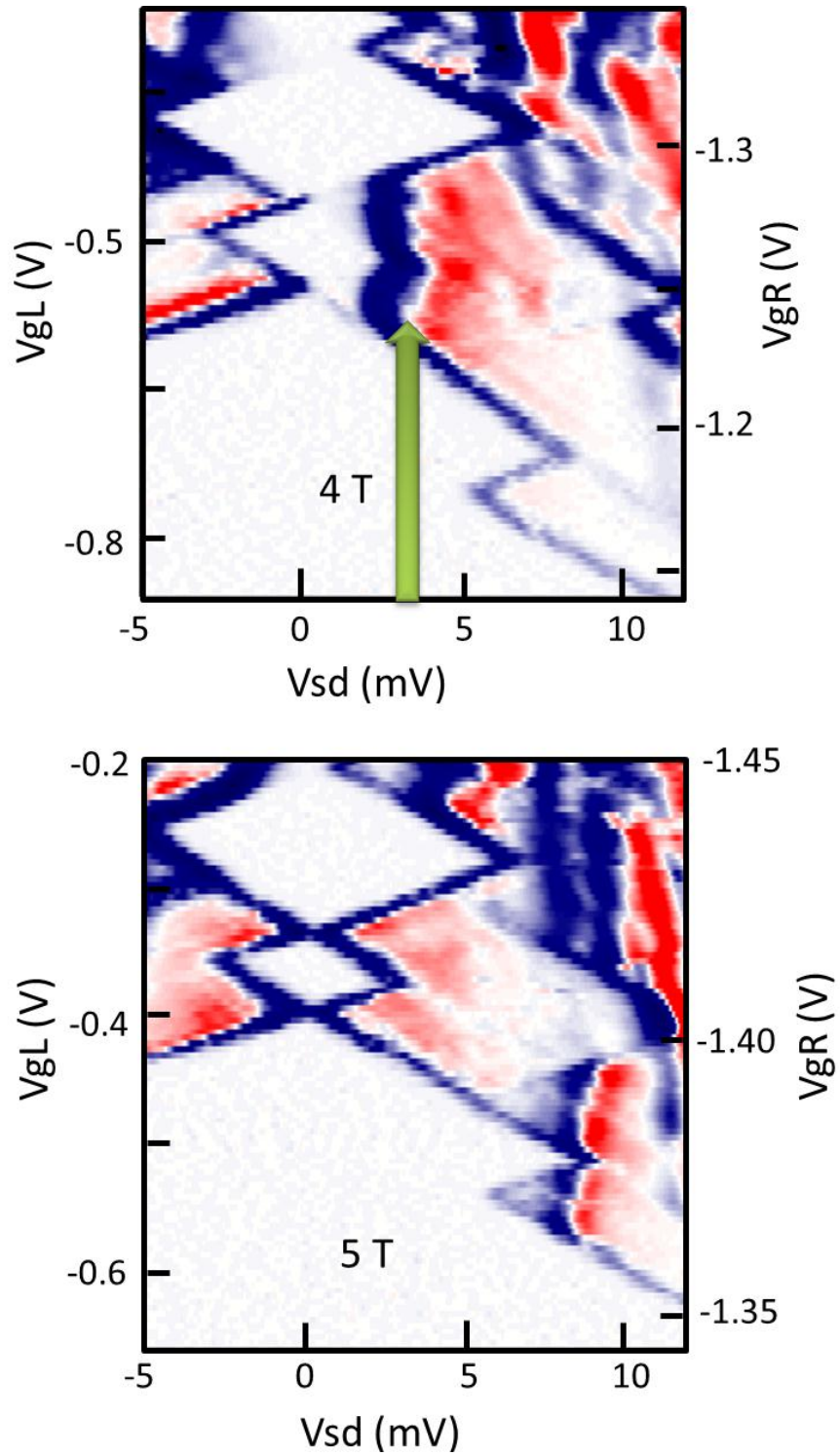


(a-b)



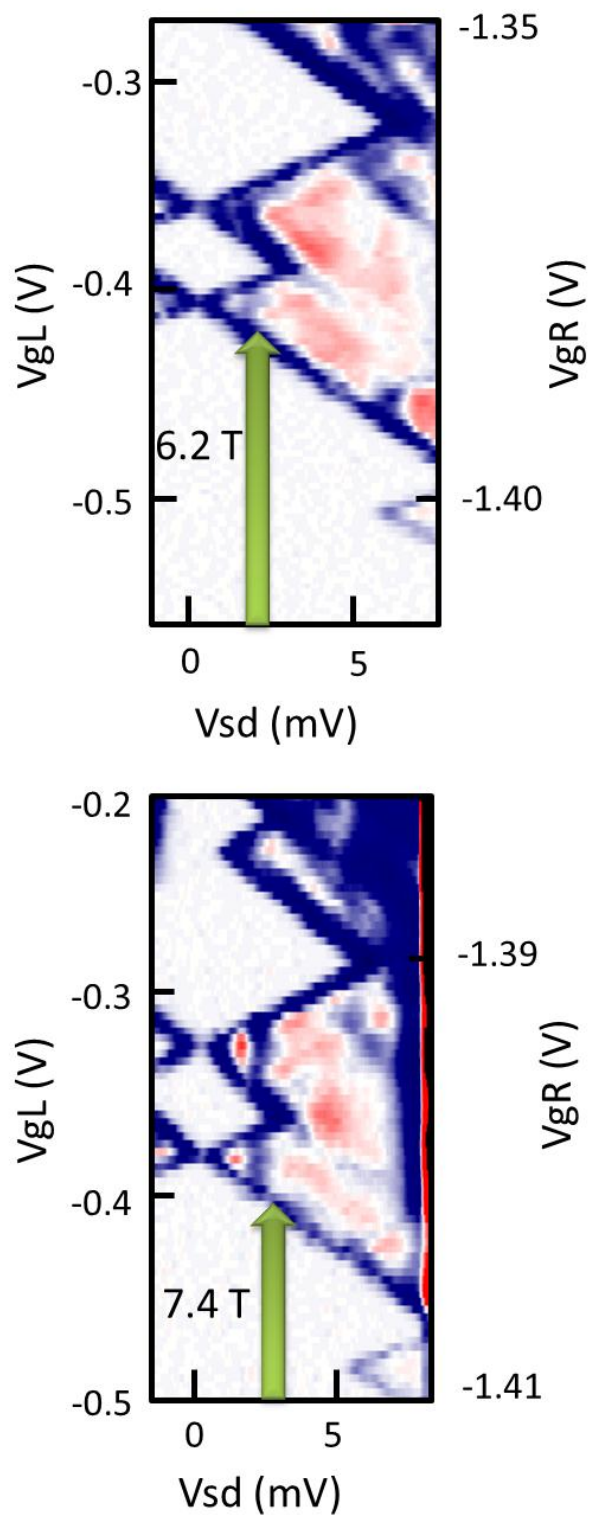
Figs. 9.3 (a-b) dI/dV plots under the magnetic fields of (a) 0.0 T, (b) 2.0 T. The arrows mark the threshold of SB.

(c-d)



Figs. 9.3 (c-d) dI/dV plots under the magnetic fields of (c) 4.0 T, (d) 5.0 T. The arrow marks the threshold of SB. At 5.0 T, SB is completely relieved and only the Coulomb blockade region is left.

(e-f)



Figs. 9.3 (e-f) dI_{sd}/dV_{sd} plots under the magnetic fields of (e) 6.2 T, (f) 7.4 T. The arrows mark the threshold of SSB.

(g)

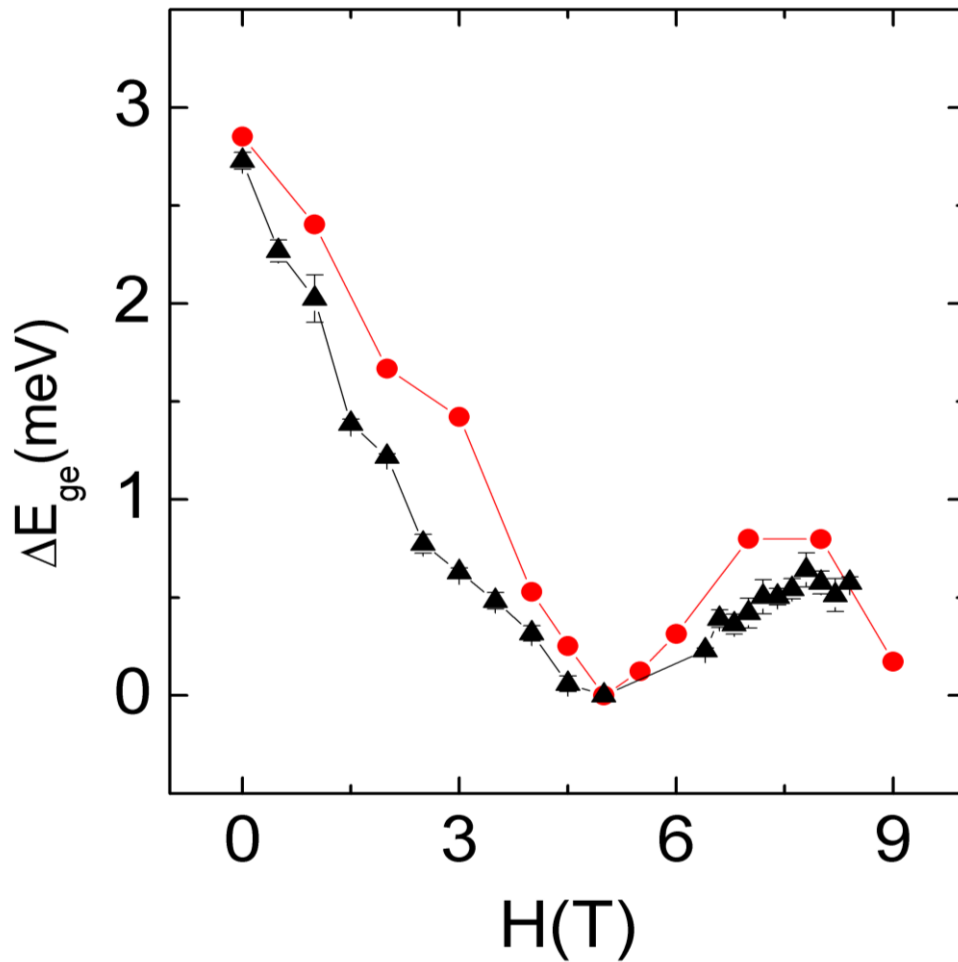


Fig. 9.3 (g) Plots of the energy difference between the ground and 1st excited (0,2) states, ΔE_{ge} . Circles indicate data extracted from (0,2) excitation spectrum in Fig. 9.2 (b), and triangles are data from the series of Coulomb diamond measurements shown in Figs. 9.3 (a-f). ΔE_{ge} measured as V_{gL}/V_{gR} (Fig. 9.2 (b)) and V_{sd} (Figs. 9.3 (a-f)) are converted to energy using the voltage drop ratio of three tunneling barriers.

9.4 Hyperfine Interaction Leads to a Short Lifetime of Spin Singlet State

Figure 9.4 (a) shows the $I_{sd} - V_{sd}$ curve measured along the dashed line in the insert. The current step at $V_{sd} \sim 3$ mV is the tunneling threshold of the first excited (0,2) state. The “leakage current” of ~ 10 pA is seen between the Coulomb blockade region and the threshold. Although the order of the current level is the same as the one above the threshold (~ 15 pA), we consider this value of leakage current consistent with SSB.

In the SSB region, the blocked $S(1,1)$ state is nearly degenerated with one of the unblocked triplets, $T_0(1,1)$, where T_0 is the zero component of triplet states. In the presence of the hyperfine interaction, nuclear spins generate a randomly fluctuating effective magnetic field ΔB_{nuc} . Whenever $S(1,1)$ and $T_0(1,1)$ are close enough to be $\lesssim g\mu_B \Delta B_{nuc}$, the two states will mix with each other efficiently via the hyperfine interaction. The energy difference between $S(1,1)$ and $T_0(1,1)$ is introduced in Sec. 7.4. With the result of a double-dot device with similar barrier thicknesses, the $S(1,1) - T(1,1)$ energy difference near zero magnetic field is estimated to be 0.42 to $0.83 \mu\text{eV}$ [84]. For ΔB_{nuc} inversely proportional to the square root of the nuclei number, our effective ΔB_{nuc} is ~ 10 mT [63] (each electron resides in our system confronting 10^5 nuclei in the GaAs dot with an effective diameter ~ 30 nm and the lattice constant = 0.57 nm). Thus, the hyperfine induced mixing is dominant in our devices.

The time required for the mixing due to hyperfine interaction was measured in the lateral double quantum dots to be ~ 10 ns [63]. Our leakage current of 10 pA suggests that the average tunneling interval is $e/(10 \text{ pA}) \sim 10$ ns, where e is the elementary charge. This time interval is consistent with the expected lifetime of $S(1,1)$! Notice that the $S(1,1) - T(1,1)$ energy difference is a function of t_c , therefore diminishing the interdot tunnel barrier, less than the 8 nm in our system, will lift the degeneracy of the $S(1,1)$ and

$T_0(1,1)$ states and decrease the leakage current in SSB.

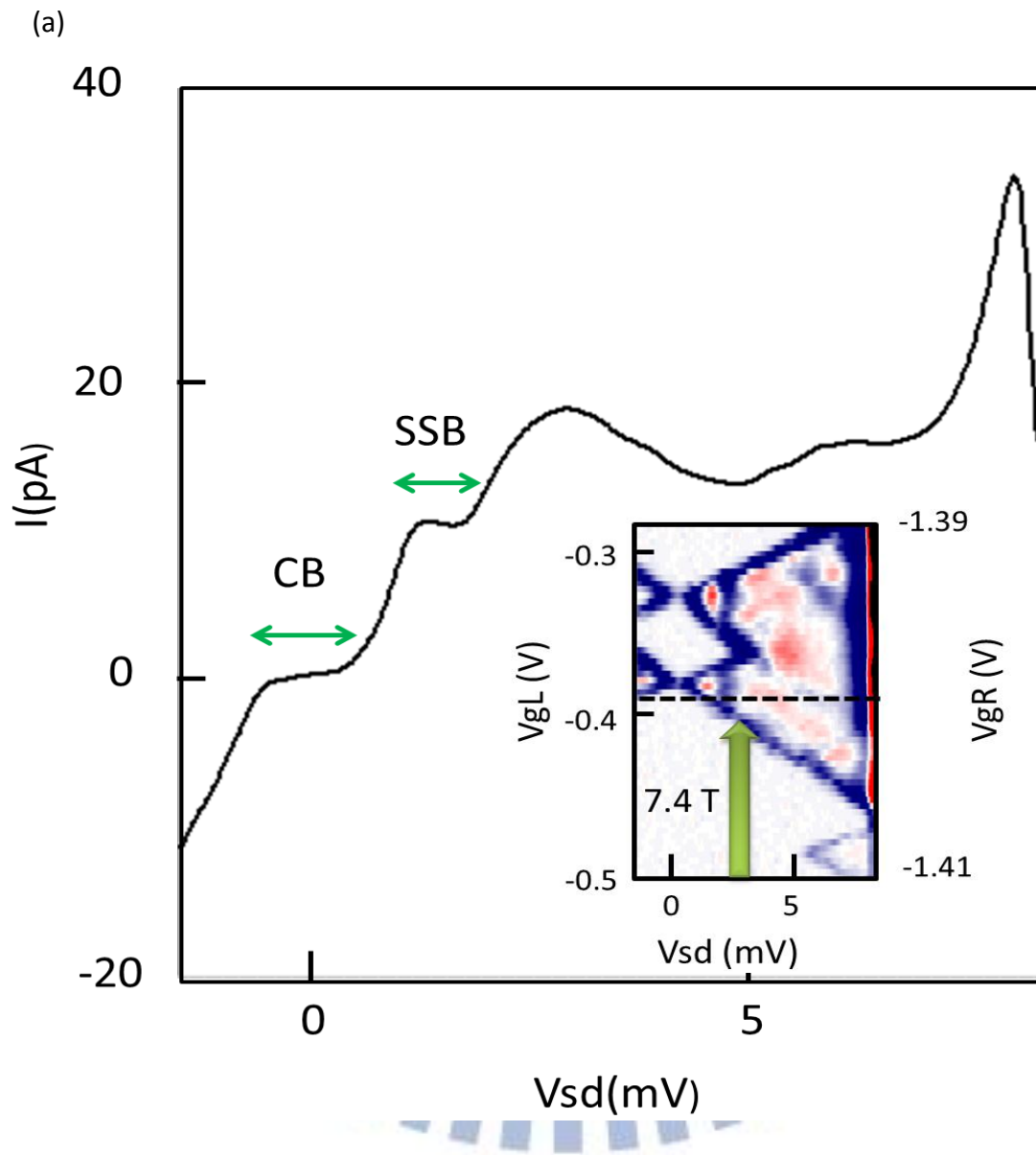


Fig. 9.4 (a) The $I_{sd} - V_{sd}$ curve along the dashed line in the insert $V_{sd} - V_g$ diagram measured at 7.4 T. A leakage current of 10 pA is observed in the SSB region.

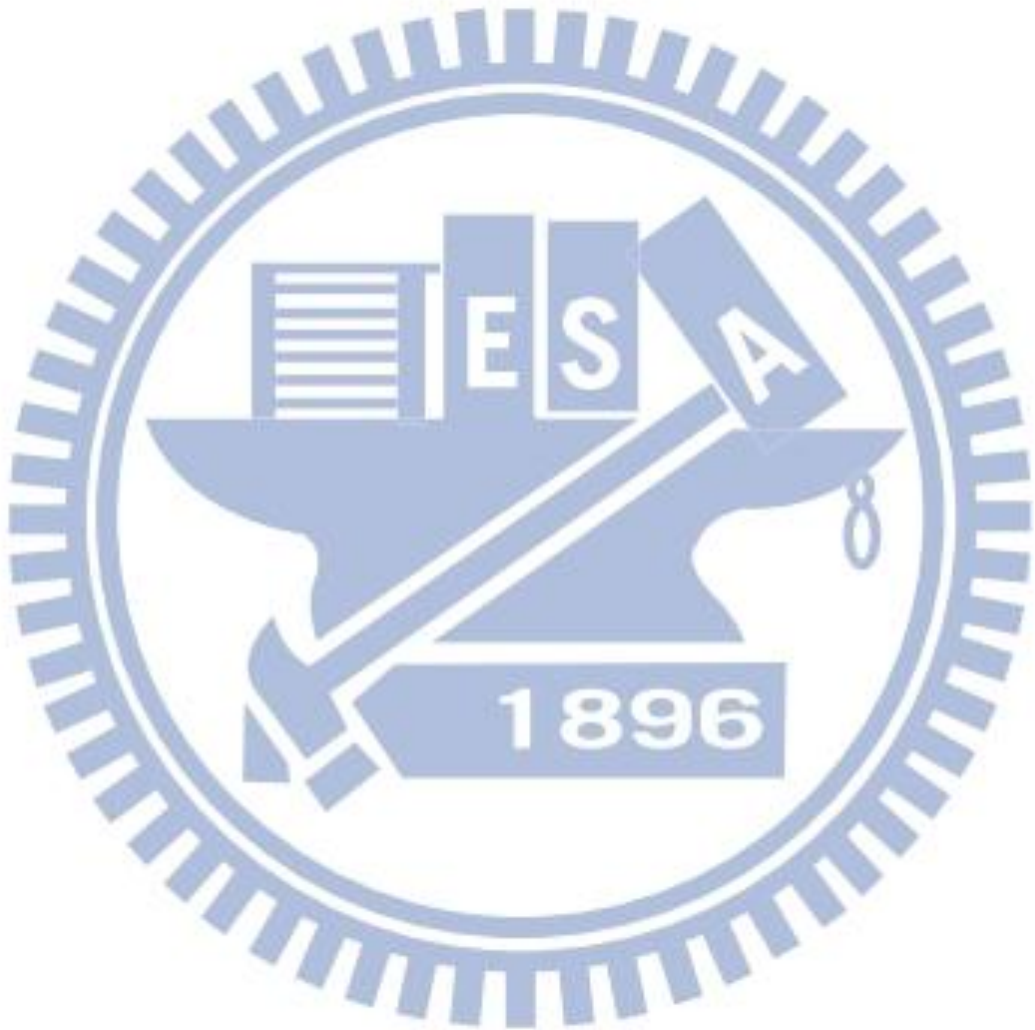
Chapter 10

Summary and Further Works

In this thesis, we observe the a new form of the spin blockade -- the singlet spin state blockade (SSB) in two-electron charge diagrams of a vertical double QD system, where the (0,2) state takes the spin triplet as the ground state under high magnetic field. The source-drain voltage dependences of the current threshold from the SB and SSB regions are consistent with the measured magnetic field dependence of the excitation spectrum of the (0,2) states. The leakage current found in SSB gives the lifetime of $S(1,1) \sim 10$ ns restricted by the randomly fluctuating effective magnetic field owing to the hyperfine interaction.

Under SSB, as proposed in Sec. 6.2 or Appendix (A), two nuclear spins in each of the two dots respectively can be entangled whenever spin flip-flop process occurs due to the hyperfine interaction. In the further work, we would like to verify the the steady condition for the nuclear spins being spin singlet by measuring the nuclear magnetic fields with similar devices of a smaller interdot tunnel barrier. To emphasize that the S pumping in Ref. [85] successively alters the gate voltage to let the system be at $S(0,2) \rightarrow S(1,1) \rightarrow$ the degeneracy of $S(1,1) - T(1,1)$ in lateral double QDs. The entanglement in $S(1,1)$ can also pass to nuclei at the $S(1,1) - T(1,1)$ degeneracy. However, to generate the nuclei

entanglement by repeating the gate-control sequence (via capacitance coupling to the dots) takes much longer time than just staying SSB to wait for SSB lifting and taking places repeatedly.



Appendix (A) The Expected Value of the Entangled Pairs of Nuclear Spins under the SSB condition

To calculate the steady condition that the system reaches as the singlet electron spin state repeatedly passes the entanglement to a nuclear spin pair from each of the two QDs via the spin flip-flop interaction, we first consider the simplest case $N_1 = N_2 = 2$, where the N_1/N_2 is the total number of the nuclear spins in QD1/QD2 as shown in Fig. A (a).

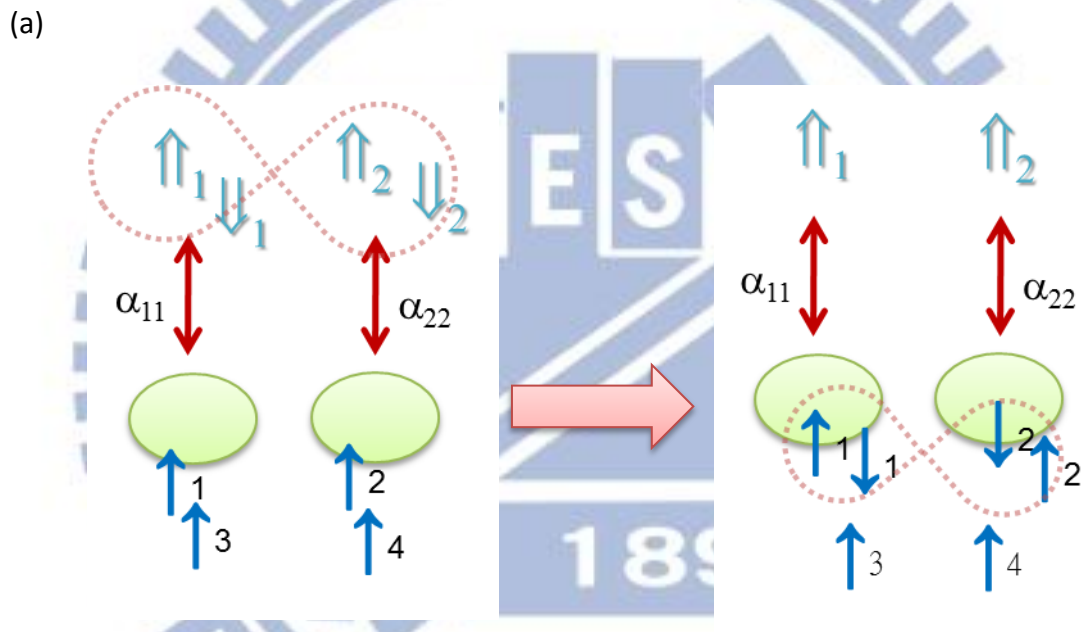


Fig. A (a) The schematic diagram of the electron/nuclear spins, represented as \uparrow/\downarrow , in a imaged system that there are only two nuclear spins in each dot. Under SSB, the system is blocked with electron spin singlet until it interacts with nuclear spins via the hyperfine interaction and release the SSB by spin flip-flop process which passes the entanglement to the nuclear pairs. The α indicates the hyperfine interaction strength (see Sec. 6.2).

In Fig. A (a), we assume $N_1 = N_2 = 2$. Since the nuclear spin direction can be either spin up or spin down, we express the mixed state of the four nuclear spins to be

$$(\alpha_1 \uparrow_1 + \beta_1 \downarrow_1)(\alpha_2 \uparrow_2 + \beta_2 \downarrow_2)(\alpha_3 \uparrow_3 + \beta_3 \downarrow_3)(\alpha_4 \uparrow_4 + \beta_4 \downarrow_4) \equiv \text{mix}^2$$

for $|\alpha_i|^2 + |\beta_i|^2 = 1$, \uparrow, \downarrow standing for the nuclear spin direction.

After the first time the singlet electron spin state interacting with the nuclear spins under the spin flip-flop process which can be regarded as an exchange states action (see Sec. 6.2), the nuclear spin state can be rewritten as

$$(\uparrow_1 \downarrow_2 - \downarrow_1 \uparrow_2)(\alpha_3 \uparrow_3 + \beta_3 \downarrow_3)(\alpha_4 \uparrow_4 + \beta_4 \downarrow_4) \equiv S_{12} \text{mix}_{34}$$

this is considering the case that the nuclear spin 1 in QD1 and the nuclear spin 2 in QD2 are entangled to be spin singlet. However, we cannot actually distinguish or identify the nuclei, so the condition would be the combination of all the possibilities as

$$\frac{1}{4} S_{12} \text{mix}_{34} + \frac{1}{4} S_{14} \text{mix}_{32} + \frac{1}{4} S_{32} \text{mix}_{14} + \frac{1}{4} S_{34} \text{mix}_{12} \equiv S \cdot \text{mix}$$

If the same action takes place for the second time, the measured nuclear spin state before and after would be

$$S \cdot \text{mix} \equiv \frac{1}{4} S_{12} \text{mix}_{34} + \frac{1}{4} S_{14} \text{mix}_{32} + \frac{1}{4} S_{32} \text{mix}_{14} + \frac{1}{4} S_{34} \text{mix}_{12}$$

$$\xrightarrow{\text{after } 2^{\text{nd}} \text{ time}} 0 + \frac{1}{3} S_{12} \text{mix}_{34} + \frac{1}{3} S_{12} \text{mix}_{34} + \frac{1}{3} S_{12} S_{34} = \frac{2}{3} S_{12} \text{mix}_{34} + \frac{1}{3} S_{12} S_{34}$$

here, we assume the nuclear spin 1 and 2 are entangled at the (1st and) 2nd time. If one of the possible spin pairs has been already entangled, then we can ignore the condition the same pair entangled again at the next time. Therefore, the $S_{12} \text{mix}_{34}$ term become 0; for

the $S_{14}mix_{32}/S_{32}mix_{14}$ terms, the entangled nuclear spin pair of 1 and 4/ 3 and 2 are broken to have the new entangled spin pair of 1 and 2. Further, we also may have two entangled pairs as $S_{12}S_{34}$. Similarly, if we consider all the probabilities, the condition is

$$\begin{aligned}
 S \cdot mix &\xrightarrow{\text{after } 2^{nd} \text{ time}} \frac{1}{4} \left(\frac{2}{3} S_{12}mix_{34} + \frac{1}{3} S_{12}S_{34} \right) + \frac{1}{4} \left(\frac{2}{3} S_{14}mix_{32} + \frac{1}{3} S_{14}S_{32} \right) \\
 &\quad + \frac{1}{4} \left(\frac{2}{3} S_{32}mix_{14} + \frac{1}{3} S_{32}S_{14} \right) + \frac{1}{4} \left(\frac{2}{3} S_{34}mix_{12} + \frac{1}{3} S_{34}S_{12} \right) \\
 &= \frac{2}{3} \left(\frac{1}{4} S_{12}mix_{34} + \frac{1}{4} S_{14}mix_{32} + \frac{1}{4} S_{32}mix_{14} + \frac{1}{4} S_{34}mix_{12} \right) \\
 &\quad + \frac{1}{3} \left(\frac{1}{4} S_{12}S_{34} + \frac{1}{4} S_{34}S_{12} + \frac{1}{4} S_{32}S_{14} + \frac{1}{4} S_{34}S_{12} \right) \equiv \frac{2}{3} S \cdot mix + \frac{1}{3} S^2
 \end{aligned}$$

For the case $N_1 = N_2 = 2$, it can be expected that there are only three possible states as mix^2 , $S \cdot mix$, and S^2 . Here, we try to see how the S^2 state changes after the spin flip-flop process happens again. Say if the nuclear spin 1 and 2 are entangled after one more interaction, then similarly

$$\begin{aligned}
 S^2 &\equiv \frac{1}{4} (S_{12}S_{34} + S_{34}S_{12} + S_{32}S_{14} + S_{34}S_{12}) \\
 &\xrightarrow{\text{after one more interaction}} \frac{1}{2} (0 + S_{12}mix_{34} + S_{12}mix_{34} + 0)
 \end{aligned}$$

If we consider all the possibilities, then

$$\begin{aligned}
 S^2 &\xrightarrow{\text{one more interaction}} \frac{1}{4} \left[\frac{1}{2} (S_{12}mix_{34} + S_{12}mix_{34}) \right] + \frac{1}{4} \left[\frac{1}{2} (S_{14}mix_{32} + S_{14}mix_{32}) \right] \\
 &\quad + \frac{1}{4} \left[\frac{1}{2} (S_{32}mix_{14} + S_{32}mix_{14}) \right] + \frac{1}{4} \left[\frac{1}{2} (S_{34}mix_{12} + S_{34}mix_{12}) \right] \\
 &= S \cdot mix
 \end{aligned}$$

That is, as the spin flip-flop process exchanges the nuclear spin and electron spin states,

the original nuclear spin state will from

$$\text{mix}^2 \xrightarrow{\text{become}} S \cdot \text{mix}$$

$$S \cdot \text{mix} \xrightarrow{\text{become}} \frac{2}{3} S \cdot \text{mix} + \frac{1}{3} S^2$$

$$S^2 \xrightarrow{\text{become}} S \cdot \text{mix}$$

In Fig. A (b), we express what and the possibilities the nuclear spin state changes to be as the spin flip-flop process repeatedly occurs under SSB due to the hyperfine interaction. After the n^{th} process or action, the probability of nuclear spins being mix^2 , $S \cdot \text{mix}$, and S^2 is $P_0(n)$, $P_1(n)$ and $P_2(n)$ respectively (note: $P_i(n)$ for i indicating the number of nuclear spin pairs being as spin singlet). And, the matrix form is

$$\begin{bmatrix} P_0(n+1) \\ P_1(n+1) \\ P_2(n+1) \end{bmatrix} = \begin{bmatrix} 0 & 0 & 0 \\ 1 & \frac{2}{3} & 1 \\ 0 & \frac{1}{3} & 0 \end{bmatrix} \begin{bmatrix} P_0(n) \\ P_1(n) \\ P_2(n) \end{bmatrix}$$

while,

$$P_0(n) + P_1(n) + P_2(n) = 1$$

(b)

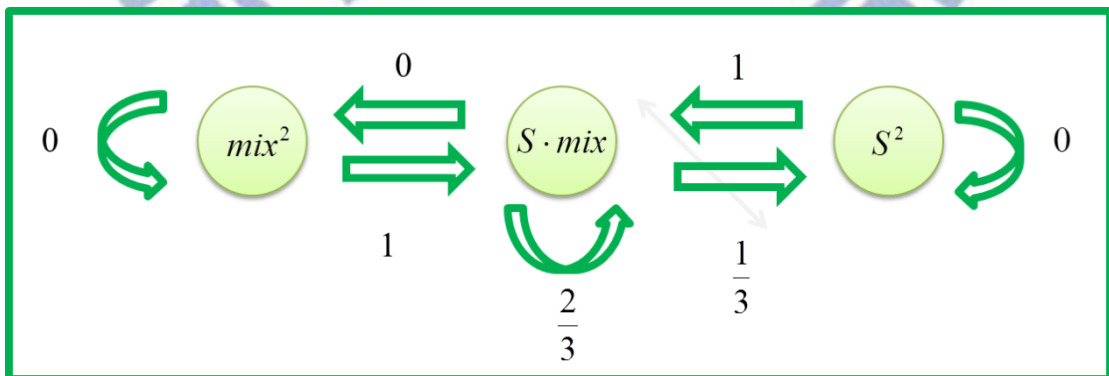


Fig. A (b) The diagram that the nuclear spins change among mix^2 , $S \cdot \text{mix}$, and S^2 condition. The arrow show the change of the direction and the number above is the change probability.

Under the steady condition, $P_i(n+1)$ should be equal to $P_i(n)$ for $i = 0,1,2$. Therefore, we can solve the matrix and have $P_0 = 0$, $P_1 = \frac{3}{4}$ and $P_2 = \frac{1}{4}$, and the expected value \bar{P} for nuclear spin pairs being singlet is

$$\bar{P} = \sum_{i=0}^2 i \cdot P_i = 0 \cdot 0 + 1 \cdot \frac{3}{4} + 2 \cdot \frac{1}{4} = \frac{5}{4}$$

since we cannot distinguish the difference of the nuclear spin in the same dot, the results be a half of this value, i.e.

$$\frac{\bar{P}}{2} = \frac{5}{8} = 62.5\%$$

With the understanding the $N_1 = N_2 = 2$ case, we go further to the case $N_1 = N_2 = N$: firstly, we can expect that after N^{th} interaction, nuclear spins may have $\text{mix}^N, S \cdot \text{mix}^{N-1}, S^2 \cdot \text{mix}^{N-2}, \dots$ or S^N conditions as expressed in Fig. A (c). Besides the mix^N and S^N , being as $S^n \cdot \text{mix}^m$ ($n + m = N$), there will be three possible results whenever the hyperfine interaction again passes the electron singlet state to nuclear spins, and the total possibility equals to 1:

(1) $S^{n+1} \cdot \text{mix}^{m-1}$: The interaction pairs one of the random nuclear spins in QD1 and that in QD2, so that there will be $m \times m = m^2$ possibilities, and we have one more extra entangled pair.

(2) $S^n \cdot \text{mix}^m$: One nuclear spin from the singlet nuclear spin pair entangles one of the random nuclear spins. Since one of the original pairs is taken apart to form a new pair, the number of the nuclear spin singlet keeps the same.

(3) $S^{n-1} \cdot \text{mix}^{m+1}$: Two singlet spin pairs are broken and each provides one nuclear spin to form a new pair of spin singlet. The possibility will be $n \times (n - 1) = n^2 - n$. Like in Fig. A (b), we also draw a diagram of the change of the nuclear spins among all possible conditions in Fig. A (d) for clear.

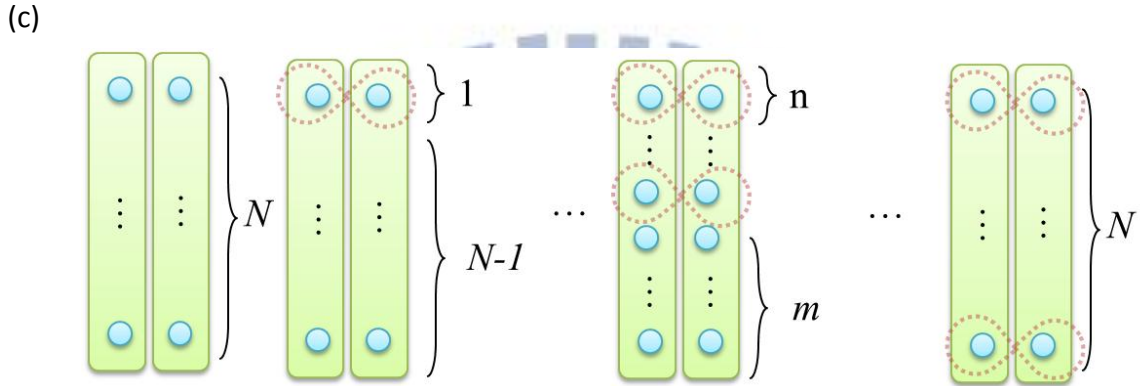


Fig. A (c) Assuming there are N nuclear spins in both QD1 and QD2, then after n th hyperfine interaction to exchange the spin state with electron spin singlet under SSB, the nuclear spins have $\text{mix}^N, S \cdot \text{mix}^{N-1}, S^2 \cdot \text{mix}^{N-2}, \dots$ or S^N possible conditions.

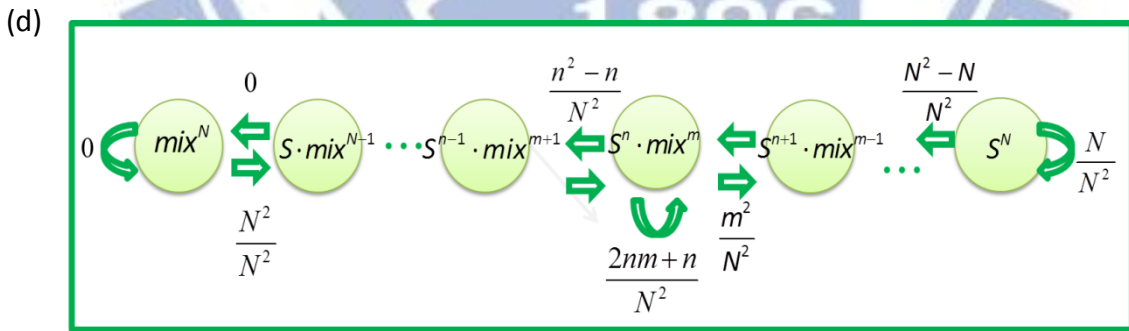


Fig. A (d) The diagram of the nuclear spins changing among the $\text{mix}^N, S \cdot \text{mix}^{N-1}, S^2 \cdot \text{mix}^{N-2}, \dots$ or S^N possible conditions. Whenever the interaction acts at the condition of $S^n \cdot \text{mix}^m$ ($n + m = N$), it may change to be $S^{n+1} \cdot \text{mix}^{m-1}, S^n \cdot \text{mix}^m$ or $S^{n-1} \cdot \text{mix}^{m+1}$. The arrow show the change of the direction and the number above is the probability.

Similarly, we can also calculate the expected value \bar{P} for nuclear spin pair being singlet with the following conditions:

(a) $\sum_{i=0}^N P_i = 1$

(b) $P_i(n+1) = P_i(n)$ under the steady condition and

$$\begin{bmatrix} P_0(n+1) \\ P_1(n+1) \\ P_2(n+1) \\ \vdots \\ P_{N-1}(n+1) \\ P_N(n+1) \end{bmatrix} = \frac{1}{N^2} \cdot \begin{bmatrix} 0 & 1^2-1 & 0 & \dots & 0 & 0 \\ N^2 & 2 \cdot 1 \cdot (N-1)+1 & 2^2-2 & & 0 & 0 \\ 0 & (N-1)^2 & 2 \cdot 2 \cdot (N-2)+2 & & 0 & 0 \\ \vdots & \vdots & \vdots & \ddots & \vdots & \vdots \\ 0 & 0 & 0 & \dots & 2 \cdot (N-1) \cdot 1+N & N^2-N \\ 0 & 0 & 0 & \dots & 1^2 & N \end{bmatrix} \begin{bmatrix} P_0(n) \\ P_1(n) \\ P_2(n) \\ \vdots \\ P_{N-1}(n) \\ P_N(n) \end{bmatrix}$$

So that, we will have

(1) For $n=0$: $P_0 = 0$

(2) For $1 \leq n \leq N-1$: $P_n = \frac{1}{N^2} \{ [N-(n-1)]^2 P_{n-1} + (2nm+n)P_n + [(n+1)^2 - (n+1)]P_{n+1} \}$

$$\rightarrow [N^2 - (2nm+n)]P_n = [N-(n-1)]^2 P_{n-1} + (n^2+n)P_{n+1}$$

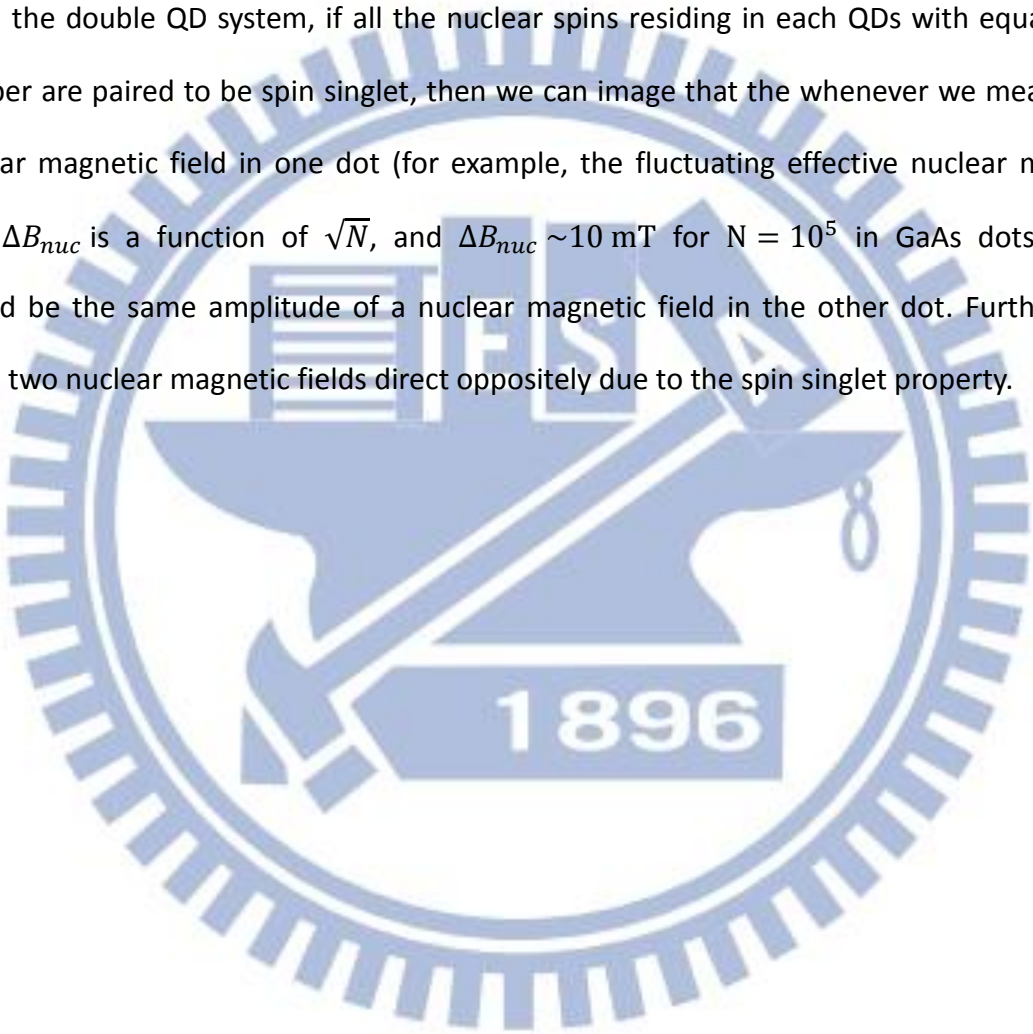
(3) For $n=N$: $P_N = \frac{1}{N^2} (P_{N-1} + NP_N)$

$$\rightarrow P_N = \frac{P_{N-1}}{N^2 - N}$$

By setting the initial conditions, and repeatedly N times of the exchange state action to have the $P_0, P_1 \dots P_N$. Then, the expected value for nuclear spin pair being singlet is

$$\frac{\bar{P}}{N} = \frac{\sum_{i=0}^N nP_i}{N}$$

In the double QD system, if all the nuclear spins residing in each QDs with equal nuclei number are paired to be spin singlet, then we can image that the whenever we measured a nuclear magnetic field in one dot (for example, the fluctuating effective nuclear magnetic field ΔB_{nuc} is a function of \sqrt{N} , and $\Delta B_{nuc} \sim 10$ mT for $N = 10^5$ in GaAs dots), there should be the same amplitude of a nuclear magnetic field in the other dot. Furthermore, these two nuclear magnetic fields direct oppositely due to the spin singlet property.



Appendix (B) Constant Interaction Model for Single QD

To understand the electronic transport properties through the quantum dot systems, we introduce the constant-interaction (CI) model. And, there are two assumptions under the CI model, and Fig. B (a) shows an equivalent circuit of a single dot system:

1. The Coulomb interaction of an electron on the dot with the environment and with other electrons on the dot can be parameterized with a constant capacitance C .
2. The influence of interaction on the discrete single-particle energy spectrum is ignored.

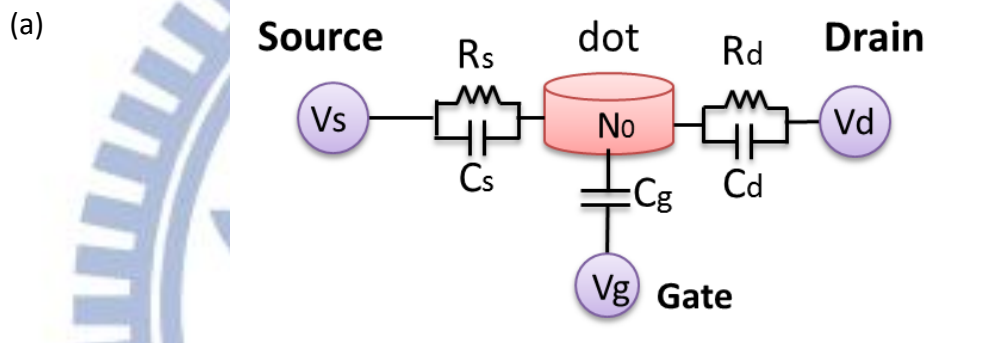


Fig. B (a) An equivalent circuit for the single-quantum-dot system. The dot connected to the leads via tunnel barriers is characterized by parallel series of the resistor R_s/R_d and the capacitor C_s/C_d , while it capacitively couples to the gate through a capacitor C_g .

Under the above assumption, we can write down the electrostatic energy $U(N)$ of the single dot system as a summation of the charge energy and the sum of electron-occupied energy levels:

$$U(N) = \frac{\{-e(N-N_0) + C_g V_g + C_s V_s + C_d V_d\}^2}{2C} + \sum_{i=1}^N E_i,$$

where N_0 is the number of electrons inside the dot without applying V_g , $C = C_s +$

$C_d + C_g$, and E_i represents the i -th single-particle energy level. $|e|N_0$ compensates the positive background charge due to the donors in the heterostructure, and $C_g V_g, C_s V_s, C_d V_d$ terms represent effective induced charges that changes the electrostatic potential in the dot continuously.

The electron transport condition can be easily exhibited by the electrochemical potential, $\mu(N)$, defined as the energy needed to add the N th electron into the dot. μ_s/μ_d are electrochemical potential of the source/drain, and only when $\mu(N)$ is within the bias window, i.e. $\mu_s \geq \mu(N) \geq \mu_d$ (see Fig. B (b)), electrons can flow through the system; beyond this condition, the system is in the so-called Coulomb blockade (CB) regions. Since the energy needed to add the N th electron into the dot should be the difference of the total energy of the system with N and $N-1$ electrons, or $\mu(N) \equiv U(N) - U(N-1)$, we write down $\mu(N)$ as

$$\mu(N) = \left(N - N_0 - \frac{1}{2}\right) E_c - \frac{E_c}{|e|} (C_g V_g + C_s V_s + C_d V_d) + E_N,$$

for $E_c = e^2/C$ is the charging energy.

(b)

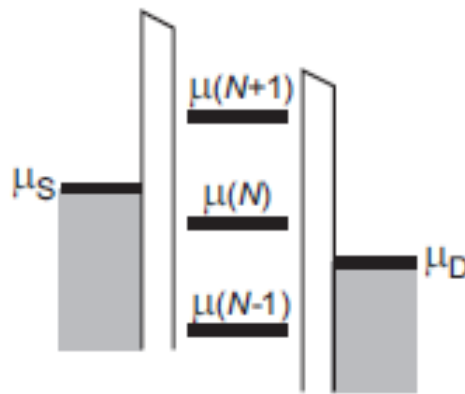


Fig. B (b) A schematic diagram of the levels in single quantum-dot device, the electron can flow via the system only when levels falls within the bias window determined by μ_s and μ_d [79].

With the value of $\mu(N)$, we can have the boundary conditions of CB regions as a function of V_{sd} and V_g , i.e. the boundary of white regions in the $V_{sd} - V_g$ charge diagram shown in Figs. B (c-d): First, considering the situation of $V_{sd} \sim 0$. The current only flows when $\mu(N, V_g) = \mu_{lead}$. In another word, along the V_g axis, the current peak can be predicted to occur with an interval of $\Delta V_g = (C/eC_g)\Delta\mu(N)$ given by $\mu(N, V_g) = \mu(N + 1, V_g + \Delta V_g) = \mu_{lead}$. Note that the addition energy, E_{add} , is defined to be $\Delta\mu(N)$ equal to $\Delta E + E_c$. Second, if we applied $\Delta V_{sd} > 0$ and assume that $\mu_s = e\Delta V_{sd}/2$ and $\mu_d = -e\Delta V_{sd}/2$, then $\Delta\mu(N)$ can be expressed when $\mu_s = \mu(N + 1)$ and $\mu_d = \mu(N)$ or $\Delta\mu(N) = e\Delta V_{sd}$. This is the condition at the yellow crossing point of a pair of two lines in Fig. B (c). With the relations of $\Delta V_g = (C/eC_g)\Delta\mu(N)$ and $\Delta\mu(N) = e\Delta V_{sd}$, we can analysis the spectrum in Fig. B (d).

(c)

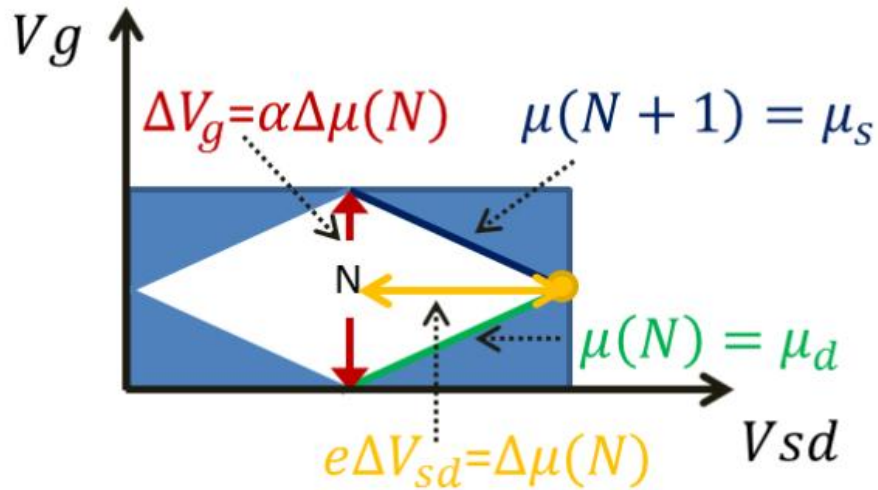


Fig. B (c) The schematic diagram for a Coulomb diamond. The alignment between $\mu(N)$ and at least one of μ_{lead} determines the boundaries.

(d)

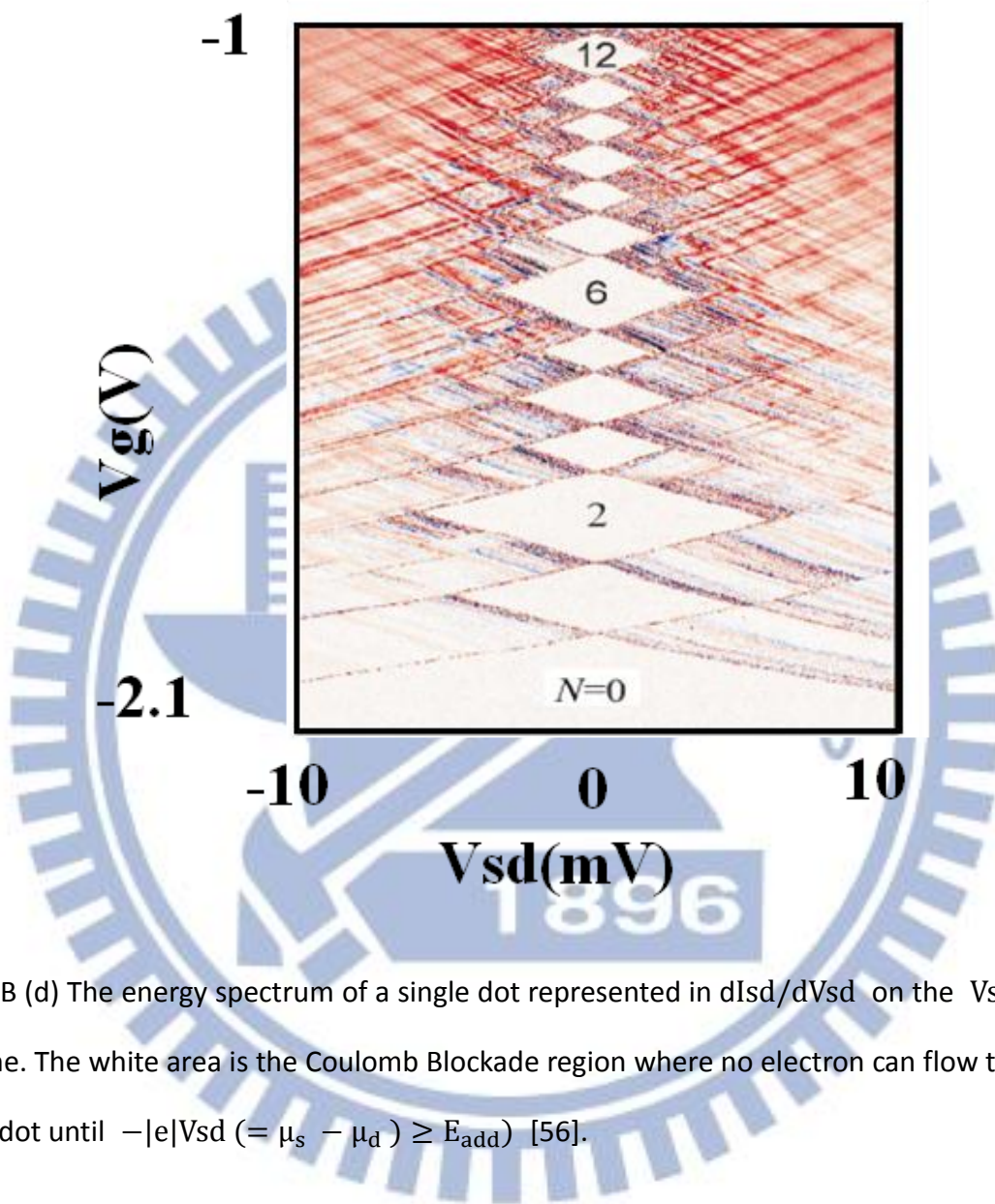


Fig. B (d) The energy spectrum of a single dot represented in dI/dV on the $V_{sd} - V_g$ plane. The white area is the Coulomb Blockade region where no electron can flow through the dot until $-|e|V_{sd} (= \mu_s - \mu_d) \geq E_{add}$ [56].

Appendix (C) Constant Interaction Model for double QDs

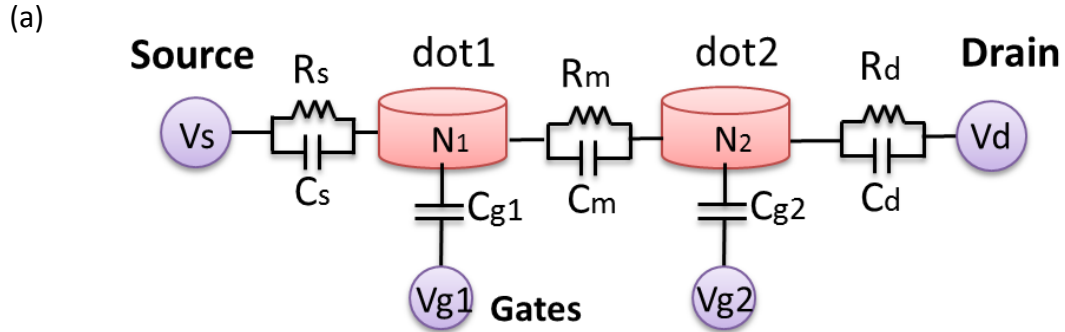


Fig. C (a) As single dot in Fig. B (a), a double quantum dot system connected to the leads and gates can be also characterized by resistors and capacitors. Besides, the tunnel barrier separating two series-connected dots is represented by a resistor R_m and a capacitor C_m , while the tiny cross-capacitances (such as between V_{g1} and dot 2) are ignored.

An equivalent circuit of a double quantum dot system under CI model is shown in Fig. C (a), and the coupling between two dots is assumed to be C_m . In single quantum dot system, the chemical potential includes the charge energy and the single-part energy parts:

$$\mu(N) \equiv U(N) - U(N-1) = \left(N - N_0 - \frac{1}{2} \right) E_c - \frac{E_c}{|e|} (C_g V_g + C_s V_s + C_d V_d) + E_N$$

as well as the additional energy, $E_{add} \equiv \Delta\mu(N) = E_c + \Delta E$. And, we have similar forms for double QD systems. We define $\mu_{1(2)}(N_1, N_2)$ as the energy needed for the $N_{1(2)}$ -th electron entering the dot1(2) to occupy discrete level N_1/N_2 , while there are already $N_2(N_1)$ electrons in dot 2(1), i.e.

$$\mu_1(N_1, N_2) \equiv U(N_1, N_2) - U(N_1 - 1, N_2) \text{ \&}$$

$$\mu_2(N_1, N_2) \equiv U(N_1, N_2) - U(N_1, N_2 - 1)$$

With respect to the single QD system, we have to further consider the interdot charge energy. Therefore,

$$\mu_1(N_1, N_2) = (N_1 - \frac{1}{2}) E_{C1} + N_2 E_{Cm} - \frac{1}{|e|} (C_{g1} V_{g1} E_{C1} + C_{g2} V_{g2} E_{Cm}) + E_{N1};$$

$$\mu_2(N_1, N_2) = (N_2 - \frac{1}{2}) E_{C2} + N_1 E_{Cm} - \frac{1}{|e|} (C_{g1} V_{g1} E_{Cm} + C_{g2} V_{g2} E_{C1}) + E_{N2}$$

where $E_{C1(2)} = e^2 \frac{C_{2(1)}}{C_1 C_2 - C_m^2}$ for $C_{1(2)} = C_{s(d)} + C_{g1(2)} + C_m$, and $E_{Cm} = e^2 \frac{C_m}{C_1 C_2 - C_m^2}$ is the energy change of one dot as an electron entering into another dot.

As mentioned in Chap. 2.2, electrons can transport through the system via two sequences of electron states as though one is going through the electron transport, while the other is through the hole transport:

$$(N_1, N_2) \rightarrow (N_1 + 1, N_2) \rightarrow (N_1, N_2 + 1) \rightarrow (N_1, N_2) \quad \&$$

$$(N_1, N_2 + 1) \rightarrow (N_1 + 1, N_2 + 1) \rightarrow (N_1 + 1, N_2) \rightarrow (N_1, N_2 + 1)$$

thus, these two situations construct the boundaries of the CB diamond edges in the $V_{sd} - V_g$ plane. And whenever either of the conditions below is achieved, the current can flow through the dots, and the corresponding diagrams of chemical potentials for transport are in Figs. C (b-c) :

$$\mu_s \geq \mu_1(N_1 + 1, N_2) \geq \mu_2(N_1, N_2 + 1) \geq \mu_d$$

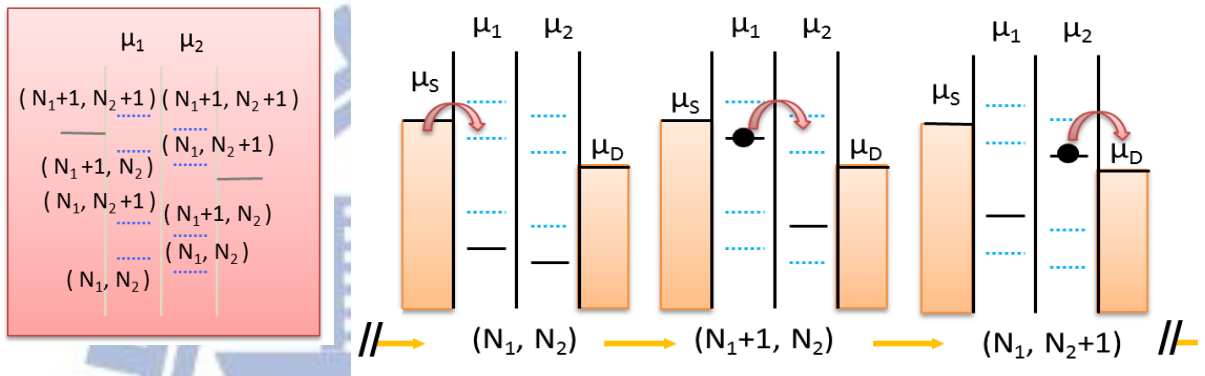
or

$$\mu_s \geq \mu_1(N_1 + 1, N_2 + 1);$$

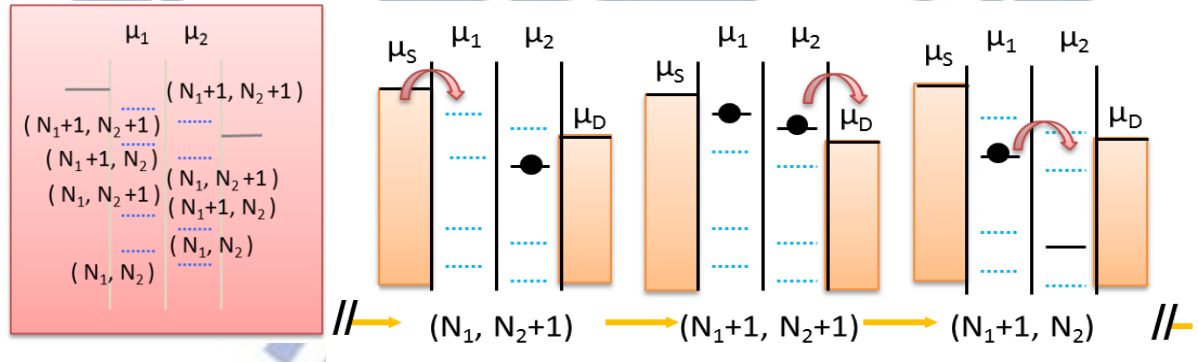
$$\mu_1(N_1 + 1, N_2) \geq \mu_2(N_1, N_2 + 1);$$

$$\mu_2(N_1, N_2 + 1) \geq \mu_d$$

(b)



(c)



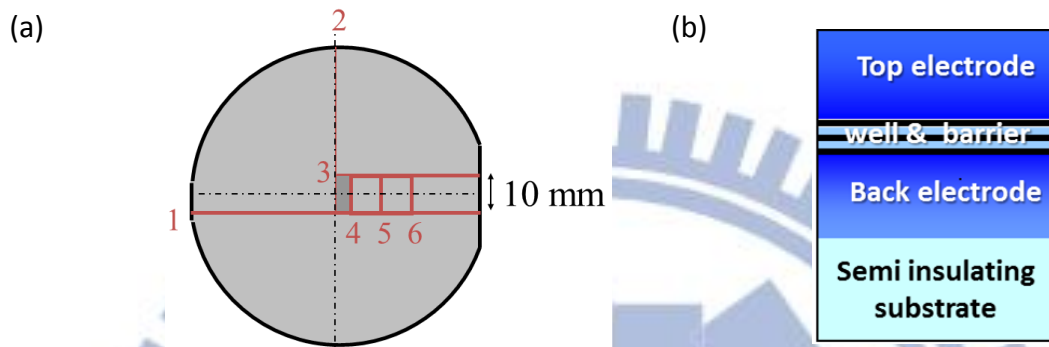
Figs. C (b-c) Electrochemical potential levels in a double-dot system. Electrons can tunnel through the system via the sequence of

(b) $(N_1, N_2) \rightarrow (N_1 + 1, N_2) \rightarrow (N_1, N_2 + 1) \rightarrow (N_1, N_2)$ or

(c) $(N_1, N_2 + 1) \rightarrow (N_1 + 1, N_2 + 1) \rightarrow (N_1 + 1, N_2) \rightarrow (N_1, N_2 + 1)$.

Appendix (D) Device Fabrication

A. **Preparation** prepare the suitable size of the wafer, and clean the surface before the fabrication.



Figs. D (a-b) (a) The wafer is prepared in a size of 9×10 mm (4 x 10 mm chip for test samples) for the following fabrication processes (b) The simplified schematic diagram of the wafer structure composed of multilayers as Table 3.

1. Prepare wafer in suitable size:
Scribe and cut the wafer in a size of **9×10 mm**.
2. Clean the surface & Etch the oxide on the surface
 - A. Immerse the wafer in a plastic beaker with **IPA** (Isopropyl alcohol).
 - B. Clean the wafer in the beaker with an ultrasonic cleaner for 5 mins (Twice).
 - C. Dry the wafer by blowing N_2 , and check the surface under microscopic.
 - D. Put the wafer in a plastic beaker with alkali for 30 secs to remove the oxide on the surface.
 - E. Rinse the wafer with flowing DI water over than 1 min, and make it dry by blowing N_2 .
 - F. Post-bake for 10 mins under $110^\circ C$.

B. Back Contact the back contact and the number are fabricated with photolithography.

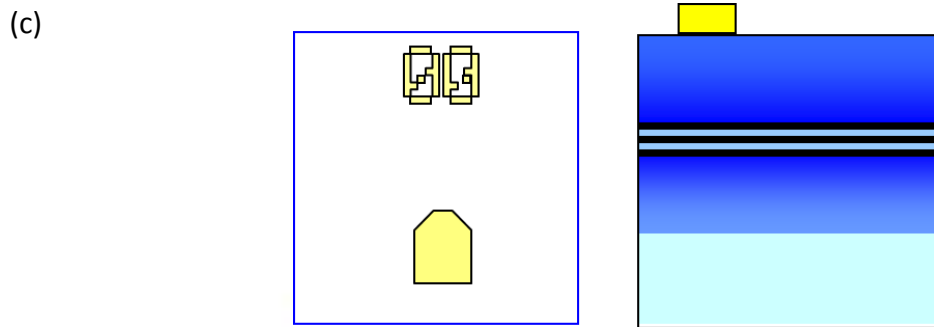


Fig. D (c) Schematic diagrams of the top views (left) and the side views (right) of the wafer during the back contact fabrication.

1. Photolithography: Spin coating and Exposure
 - A. Drop the photoresist on the center of the surface.
 - B. Spin coating in 3 stages:
500 rpm for 3 secs → slop for 7 secs → 4000 rpm for 40 secs.
 - C. Pre-bake (soft-bake) for 20mins under 80°C.
 - D. Expose with a mercury lamp for 12 secs.
2. Developing: Remove the photoresist
 - A. Develop with S351 developer, and sway for 40~60 secs.
 - B. Rinse with flowing DI water over than 1 min, and make it dry by blowing N₂.
3. Evaporation and Lift off
 - A. Deposit 20 nm-thick Ti and then 200 nm-thick Au.
 - B. Immerse in Acetone for 5 mins, and spray Acetone to lift the photoresist off.
 - C. Immerse in clean Acetone for 1 min and rinse with flowing DI water.
 - D. Bake for 10 mins under 110°C.

C. **Top Contact** In this step, the top contact is fabricated with E-beam lithography.

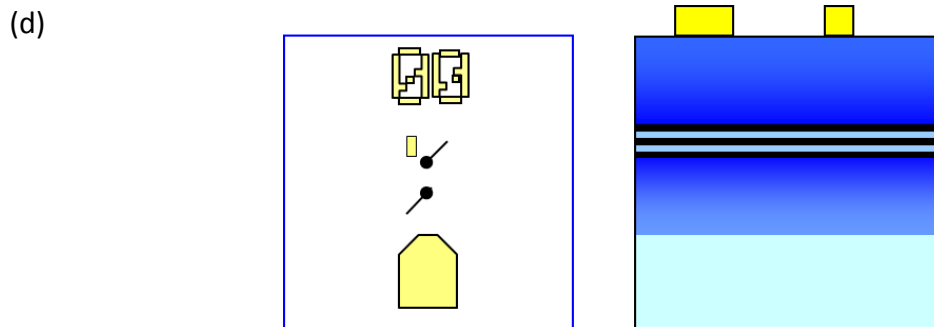


Fig. D (d) Schematic diagrams of the top views (left) and the side views (right) of the wafer during the top contact fabrication.

1. E-beam lithography: Spin coating and Exposure
 - A. Drop PMMA on the center of the surface.
 - B. Spin coating in 3 stages:
500 rpm for 3 secs → stop for 7 secs → 4000 rpm for 60 secs.
 - C. Pre-bake for over 1 hour under 170°C.
 - D. Expose with E-beam lithography.
2. Developing
 - A. Develop with both IPA and OEPR-1000 under 13.6°C:
IPA for 1 min → OEPR-1000 for 30 secs → IPA for 1 min.
 - B. dry by blowing N₂ (note : no DI water)
3. Evaporation and Lift off
 - A. Deposit 20 nm-thick Ti and then 100 nm-thick Au.
 - B. Lift off:
Acetone for 5 mins → spray Acetone → immerse in clean Acetone for 1 min.

- C. Rinse with flowing DI water and make it dry by blowing N₂
- D. Bake for 10 mins under 110°C.
- E. UV Ozone stripper: Purge Ozone for 10 mins under 200°C.
- F. Rinse with flowing DI water and dry by blowing N₂.
- G. Bake for 10 mins under 110°C.

D. **ECR (electron cyclotron resonance) Dry Etch** The embryo pillar structure is sculpted in this step: part of metal films and most of semiconductor are removed, but those covered by deposited Ti/Au are left.

(e)

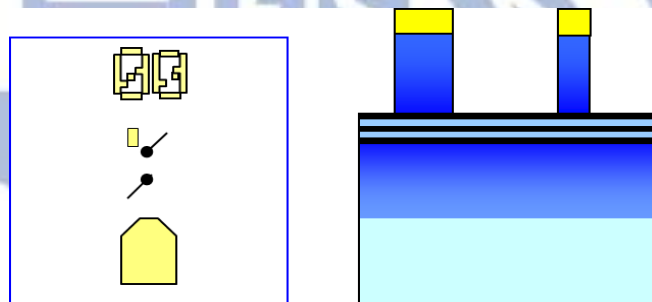


Fig. D (e) Schematic diagrams of the top views (left) and the side views (right) of the wafer during the dry etch process.

1. Attached to a Si wafer with the photoresist and bake for 10 mins under 110°C.
2. UV Ozone stripper: Purge Ozone for 10 mins under 110°C.
3. Etch the wafer down before the three-barrier structure (about 400 nm) with BCl₃ plasma.
4. Rinse with flowing DI water, make it dry by blowing N₂ and bake for 10 mins under 110°C, and then check with SEM.

E. **Wet Etch** The sulfuric acid etches down the semiconductor parts to the three-barrier layers, and the diameter of the pillar is also lessened.

(f)

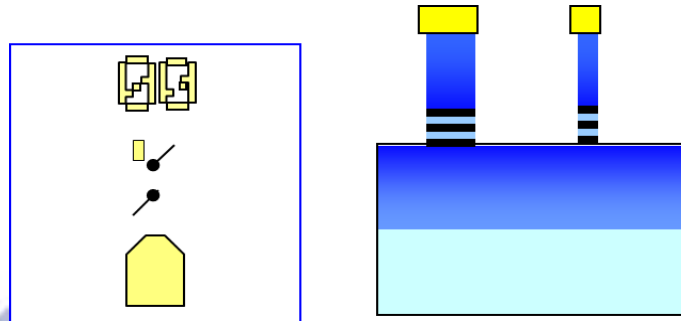


Fig. D (f) Schematic diagrams of the top views (left) and the side views (right) of the wafer during the wet etch process.

1. Etch down the wafer beneath the end of the three barrier structure with the sulfuric acid ($\text{H}_2\text{O} : \text{H}_2\text{SO}_4 : \text{H}_2\text{O}_2 = 25 : 5 : 1$) in three steps:
under 10°C H_2O for 1 min \rightarrow sulfuric acid (about tens of nm) \rightarrow H_2O for 1 min
2. Rinse with flowing DI water, make it dry by blowing N_2 and bake for 10 mins under 110°C, and then check with SEM.

F. **Gate** In this step, the gate(s) is fabricated with E-beam lithography.

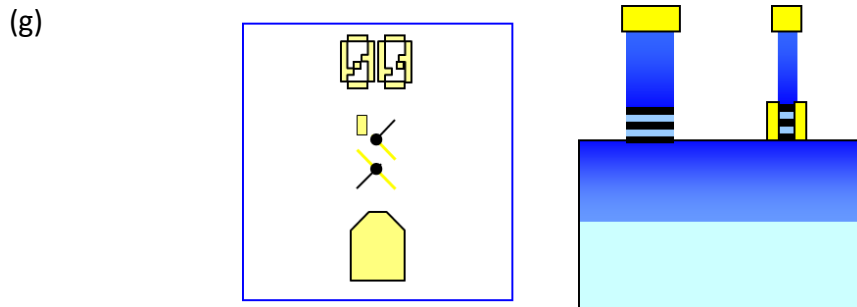


Fig. D (g) Schematic diagrams of the top views (left) and the side views (right) of the wafer during the gate fabrication.

1. E-beam lithography: Spin coating and Exposure

A. Drop PMMA on the center of the surface.

B. Spin coating in 3 stages:

500 rpm for 3 secs → slop for 7 secs → 4000 rpm for 60 secs.

C. Pre-bake for over 1 hour under 170°C.

D. Expose with E-beam lithography.

2. Developing

A. Develop with both IPA and OEPR-1000 at **room temperature**:

IPA for 1 min → OEPR-1000 for 30 secs → IPA for 1 min.

B. dry by blowing N₂

3. Evaporation and Lift off

A. Deposit 20 nm-thick Ti and then 100 nm-thick Au.

B. Lift off:

Acetone for over 6 hrs → spray Acetone → immerse in clean Acetone for 1 min.

- C. Rinse with flowing DI water, make it dry by blowing N₂ and bake for 10 mins under 110°C.
- D. UV Ozone stripper: Purge Ozone for 10 mins under 200°C.
- E. Rinse with flowing DI water, dry by blowing N₂ and bake for 10 mins under 110°C.
- F. Check by SEM.



G. Mesa

(h)

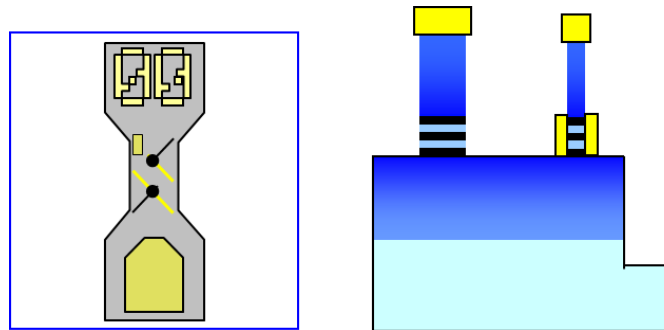


Fig. D (h) Schematic diagrams of the top views (left) and the side views (right) of the wafer during the mesa process.

1. Photolithography: Spin coating and Exposure

- A. Drop the photoresist on the center of the surface.
- B. Spin coating in 3 stages:
500 rpm for 3 secs → slop for 7 secs → 4000 rpm for 40 secs.
- C. Pre-bake (soft-bake) for 20 mins under 80°C.
- D. Expose with a mercury lamp for 20 secs.

2. Developing: Remove the photoresist

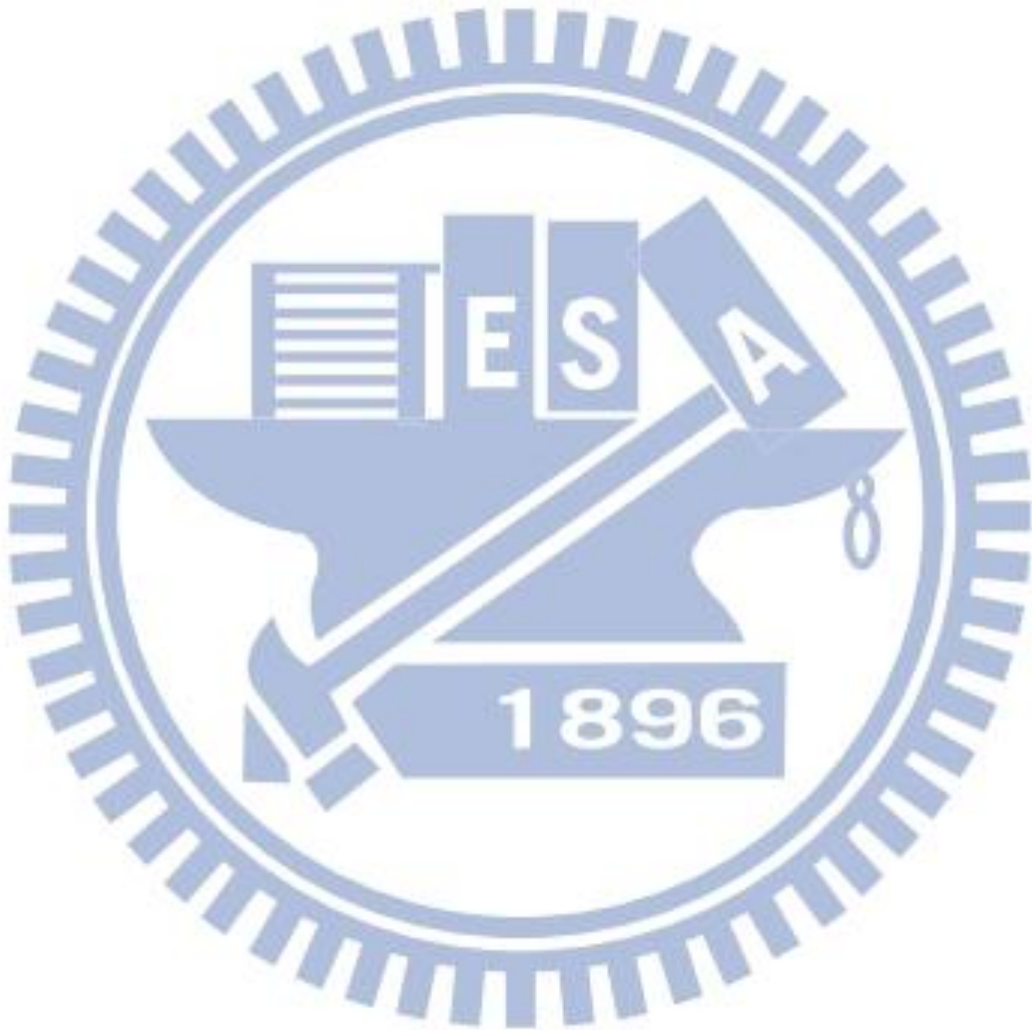
- A. Develop with S351 developer, and sway for 1 min.
- B. Rinse with flowing DI water over than 1 min, and make it dry by blowing N₂.
- C. Bake for 10 mins under 110°C.

3. Wet etching

- A. Etch down the wafer beneath the end of the three barrier structure with the sulfuric acid (H₂O: H₂SO₄: H₂O₂= 25: 5: 1) in three steps:

under 10°C H₂O for 1 min → sulfuric acid → H₂O for 1 min.

- B. Rinse with flowing DI water, make it dry by blowing N_2 and bake for 10 mins. under 110°C . (Repeat A & B until etching to the wanted condition)
- C. Immerse in Acetone for 1 min (Twice).
- D. Rinse with flowing DI water and make it dry by blowing N_2



H. Step Smoother

(i)

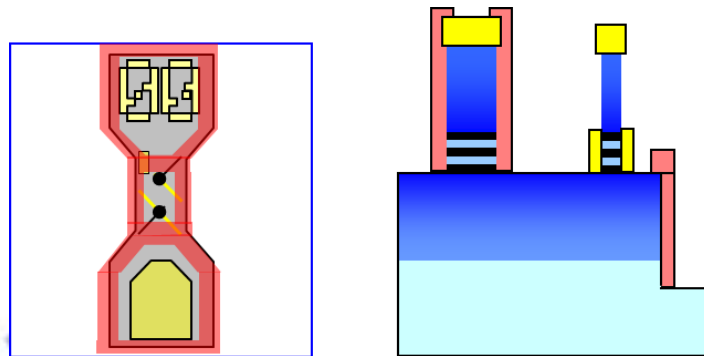


Fig. D (i) Schematic diagrams of the top views (left) and the side views (right) of the wafer during the step smoother process.

1. Photolithography: Spin coating and Exposure

- A. Drop the photoresist on the center of the surface.
- B. Spin coating in 3 stages:
500 rpm for 3 secs → slop for 7 secs → 4000 rpm for 40 secs.
- C. Pre-bake (soft-bake) for 20 mins under 80°C.
- D. Expose with a mercury lamp for 20 secs.

2. Developing: Remove the photoresist

- A. Develop with S351 developer, and sway for 1 min.
- B. Rinse with flowing DI water over than 1 min, and make it dry by blowing N₂.
- C. Bake for more than 30 mins under 170°C.
- D. UV Ozone stripper: Purge Ozone for 10 mins under 200°C.
- E. Rinse with flowing DI water, make it dry by blowing N₂ and bake for 10 mins. under 110°C.

I. Bonding Pad

(j)

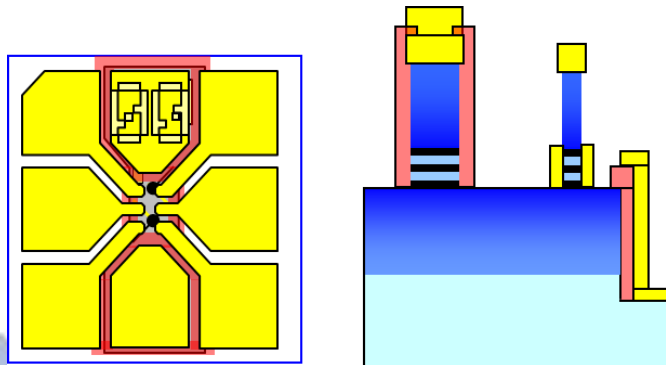


Fig. D (j) Schematic diagrams of the top views (left) and the side views (right) of the wafer during the bonding pad process.

1. Photolithography: Spin coating and Exposure

- A. Drop the photoresist on the center of the surface.
- B. Spin coating in 3 stages:
500 rpm for 3 secs → slop for 7 secs → 4000 rpm for 40 secs.
- C. Pre-bake (soft-bake) for 20mins under 80°C.
- D. Expose with a mercury lamp for **25 secs**.

2. Developing: Remove the photoresist

- A. Immerse in Chlorobenzene for 4.5 mins to make the surface of the resist harder.
- B. Blowing with N₂.
- C. Bake for more than 5 mins under 80°C and cool down by blowing N₂.
- D. Develop with S351 developer, and sway for 1 min 20 secs.
- E. Rinse with flowing DI water, make it dry by blowing N₂.

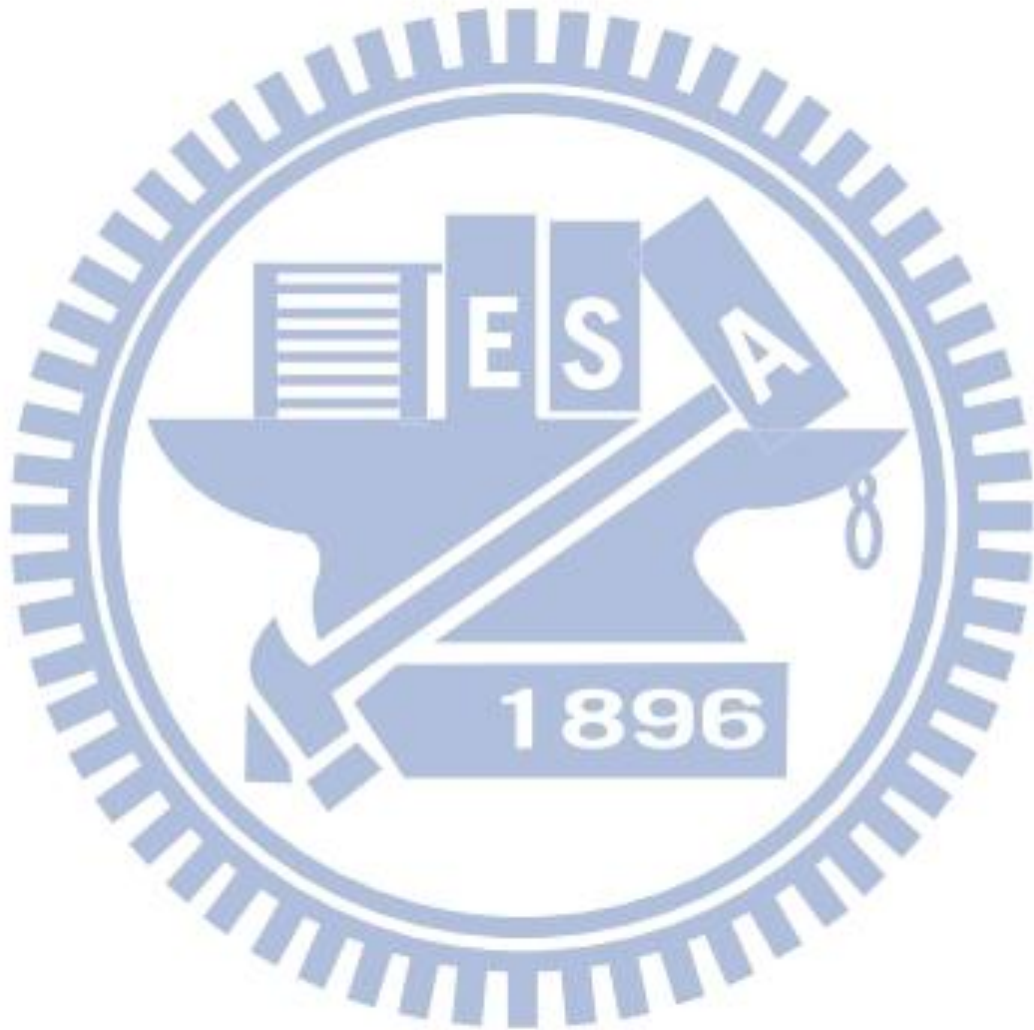
3. Evaporation and Lift off

A. Deposit 20 nm-thick Ti and then 300 nm-thick Au.

B. Lift off:

Acetone for 5 mins → spray Acetone → immerse in clean Acetone for 1 min.

C. Rinse with flowing DI water, make it dry by blowing N₂ and bake for 10 mins under 110°C.



Reference

- [1] J. M. Rowell and L. Y. Shen, Phys. Rev. Lett. **17**, 15(1966).
- [2] F. Mezei, Phys. Lett. **25A**, 534 (1967).
- [3] A. F. G. Wyatt and D. J. Lythall, Phys. Lett. **25A**, 541(1967).
- [4] D. J. Lythall and A. F. G. Wyatt, Phys. Rev. Lett., **20**, 1361 (1968).
- [5] F. Mezei and A. Zawadowski, Phys. Rev. B **3**, 3127 (1971).
- [6] Y. H. Lin, Y. C. Sun, W. B. Jian, H. M. Chang, Y. S. Huang, and J. J. Lin, Nanotechnology **19**, 045711 (2008).
- [7] P. A. Gould, Br. J. Appl. Phys. **16**, 1481 (1965).
- [8] V. A. Krupenin, V. O. Zalunin, and A. B. Zorin, Microelectron. Eng. **81**, 217 (2005).
- [9] B. L. Altshuler and A. G. Aronov, in *Electron-Electron Interactions in Disordered Systems* (North-Holland, Amsterdam, 1985).
- [10] B. L. Altshuler and A. G. Aronov, Sov. Phys. JETP **50**, 968 (1979).
- [11] B. L. Altshuler, A. G. Aronov, and P. A. Lee, Phys. Rev. Lett. **44**, 1288 (1980).
- [12] B. L. Altshuler, A. G. Aronov, and A. Yu. Zuzin, Zh. Eksp. Teor. Fiz. **86**, 709 (1984) [Sov. Phys. JETP **59**, 415 (1984)].
- [13] B. L. Altshuler and A. G. Aronov, Solid State Commun. **30**, 115 (1979).
- [14] W. L. McMillan, Phys. Rev. B **24**, 2739 (1981).
- [15] W. L. McMillan and J. Mochel, Phys. Rev. Lett. **46**, 556 (1981).
- [16] R. C. Dynes and J. P. Garno, Phys. Rev. Lett. **46**, 137 (1981).

- [17] L. Y. L. Shen and J. M. Rowell, Phys. Rev. **165**, 566 (1968).
- [18] X. M. Lin, H. M. Jaeger, C. M. Sorensen, and K. J. Klabunde, J. Phys. Chem. B **105**, 3353 (2001).
- [19] D. J. Mowbray and M. S. Skolnick, J. Phys. D **38** 2059 (2005).
- [20] D. Beysens, C. M. Knobler and H. Schaffar, Phys. Rev. B **41**, 9814 (1990).
- [21] R. W. Simon, B. J. Dalrymple, D. Van Vechten, W. W. Fuller, and S. A. Wolf, Phys. Rev. B **36**, 1962 (1987).
- [22] A. Gerber, J. Phys.: Condens. Matter **2**, 8161 (1990).
- [23] A. Gerber, A. Milner, G. Deutscher, M. Karpovsky, and A. Gladkikh, Phys. Rev. Lett. **78**, 4277 (1997).
- [24] L. Rotkina, S. Oh, J. N. Eckstein, and S. V. Rotkin, Phys. Rev. B **72**, 233407 (2005).
- [25] I. S. Beloborodov, A. V. Lopatin, V. M. Vinokur, and K. B. Efetov, Rev. Mod. Phys. **79**, 469 (2007).
- [26] K. B. Efetov and A. Tschersich, Phys. Rev. B **67**, 174205 (2003); Europhys. Lett. **59**, 114 (2002).
- [27] I. S. Beloborodov, A. V. Lopatin, G. Schwiete, and V. M. Vinokur, Phys. Rev. B **70**, 073404 (2004).
- [28] R. W. Simon, B. J. Dalrymple, D. Van Vechten, W. W. Fuller, and S. A. Wolf, Phys. Rev. B **36**, 1962 (1987).
- [29] B. Abeles, P. Sheng, M. D. Coutts, and Y. Arie, Adv. Phys. **24**, 407 (1975).
- [30] T. B. Tran, I. Beloborodov, X. M. Lin, T. P. Bigioni, V. M. Vinokur, and H. M. Jaeger, Phys. Rev. Lett. **95**, 076806 (2005).
- [31] I. S. Beloborodov, A. V. Lopatin, and V. M. Vinokur, Phys. Rev. B **72**, 125121 (2005).
- [32] It should be aware that the $\sigma \propto -\exp(\sqrt{T_0/T})$ dependence can alternatively and satisfactorily be explained by the conductivity theory of P. Sheng, B. Abeles, and Y. Arie, Phys. Rev. Lett. **31**, 44 (1973). Further experiments to critically discriminate the

microscopic origins of this temperature behavior in the insulating regime would be highly meaningful.

- [33] E. L. Wolf, *Principles of Electron Tunneling Spectroscopy* (Oxford University Press, New York, 1985).
- [34] W. F. Brinkman, R. C. Dynes, and J. M. Rowell. *J. Appl. Phys.* **41**, 1915 (1970).
- [35] P. A. Lee and T. V. Ramakrishnan, *Rev. Mod. Phys.* **57**, 287 (1985).
- [36] Y. Imry and Z. Ovadyahu, *Phys. Rev. Lett.* **49**, 841 (1982).
- [37] A. E. White, R. C. Dynes, and J. P. Garno, *Phys. Rev. B.* **31**, 1174 (1985).
- [38] V. N. Lutski, A. S. Rylík, and A. K. Savchenko, *JETP Lett.* **41**, 163 (1985).
- [39] M. Gijs, Y. Bruynseraede, and A. Gilibert, *Solid State Commun.* **57**, 141 (1986).
- [40] M. E. Gershenson, V. N. Gubankov, and M. I. Falei, *Sov. Phys. JETP* **63**, 1287 (1986).
- [41] S. Schmitz and S. Ewert, *Solid State Commun.* **74**, 1067 (1990).
- [42] G. Hertel, D. J. Bishop, E. G. Spencer, J. M. Rowell, and R. C. Dynes, *Phys. Rev. Lett.* **50**, 743 (1983).
- [43] M. Kobayashi, K. Tanaka, A. Fujimori, S. Ray, and D. D. Sarma, *Phys. Rev. Lett.* **98**, 246401 (2007).
- [44] I. S. Beloborodov, K. B. Efetov, A. V. Lopatin, and V. M. Vinokur, *Phys. Rev. Lett.* **91**, 246801 (2003).
- [45] I. Estermann, S. A. Friedberg, and J. E. Goldman, *Phys. Rev.* **87**, 582 (1952).
- [46] X. X. Zhang, C. Wan, H. Liu, Z. Q. Li, P. Sheng, and J. J. Lin, *Phys. Rev. Lett.* **86**, 5562 (2001).
- [47] J. J. Lin and J. P. Bird, *J. Phys.: Condens. Matter* **14**, R501 (2002).
- [48] Alternatively, for spherical grains of radius a separated by insulating barriers with average thickness s , the charging energy is predicted to be $E_c = 2se^2/\epsilon_r\epsilon_0a(a/2 + s)$, where ϵ_0 is the permittivity of vacuum and ϵ_r is the dielectric constant of the insulating barrier (Refs. 9 and 16). Taking $\epsilon_r \approx 13$ for Cr_2O_3 [P. H. Fang and W. S.

Brower, Phys. Rev. **129**, 1561 (1963)], a thickness $s \sim 0.2$ nm, and a diameter $a \sim 10$ nm, we obtain an estimate of $E_c \sim 10$ meV. This estimated value is in good accord with those values obtained by using $E_c \approx 10k_B T^*$.

- [49] M. Huth, D. Klingenberg, Ch. Grimm, F. Porrati, and R. Sachser, New J. Phys. **11**, 033032 (2009).
- [50] P. Achatz, W. Gajewski, E. Bustarret, C. Marcenat, R. Piquerel, C. Chapelier, T. Dubouchet, O. A. Williams, K. Haenen, J. A. Garrido, and M. Stutzmann, Phys. Rev. B **79**, 201203(R) (2009).
- [51] Using $D = 1.4$ cm²/s, we obtain the thermal diffusion length $L_T = \sqrt{D\hbar/k_B T} \approx 33/\sqrt{T}$ nm in the sample A. Therefore, in terms of the EEI effect, the Cr electrode should be 3D at temperatures above ≈ 1 K. If we insisted in plotting resistance versus temperature for the sample B (D), a dependence $R \propto \ln T$ is observed in essentially the same temperature interval shown in Fig. 4.1 (b). However, the measured resistance rise is more than a factor of 3 as could be expected from the 2D EEI and WL effects, taking the sheet resistance listed in Table 1 into calculation.
- [52] M. V. Feigel'man, A. S. Iosevich, and M. A. Skvortsov, Phys. Rev. Lett. **93**, 136403 (2004). Previously, a $G(V) \propto \sqrt{V}$ dependence had been observed in granular Al films, R. C. Dynes and J. P. Garno, Phys. Rev. Lett. **46**, 137 (1981). However, the authors interpreted their results in terms of then available Altshuler-Aronov theory of weakly disordered homogeneous conductors (Ref. 13).
- [53] D. Loss and D. P. DiVincenzo, Phys. Rev. A **67**, 120 (1998).
- [54] D. P. DiVincenzo and D. Loss, J. Magn. Magn. Mater. **200**, 202 (1999).
- [55] D. P. DiVincenzo, Science, **309**, 30 (2005).
- [56] L. P. Kouwenhoven, T. H. Oosterkamp, M. W. S. Danoesastro, M. Eto, D. G. Austing, T. Honda, and S. Tarucha, Science **278**, 1788 (1997).
- [57] L. P. Kouwenhoven, D. G. Austing, and S. Tarucha, Rep. Prog. Phys. **64**, 701 (2001).

- [58] E. Knill, Nature **463**, 441 (2010); M. A. Nielsen and I. L. Chuang, *Quantum Computation and Quantum Information* (Cambridge University Press, UK, 2000).
- [59] D. P. DiVincenzo, J. Appl. Phys. **85**, 4785 (1999).
- [60] M. Pioro-Ladrière, T. Obata, Y. Tokura, Y.-S. Shin, T. Kubo, K. Yoshida, T. Taniyama, and S. Tarucha, Nature Phys. **4**, 776 (2008).
- [61] S. Nadj-Perge, S. M. Frolov, E. P. A. M. Bakkers, and L. P. Kouwenhoven, Nature **468**, 1084 (2010).
- [62] F. H. L. Koppens, C. Buizert, K. J. Tielrooij, I. T. Vink, K. C. Nowack, T. Meunier, L. P. Kouwenhoven, and L. M. K. Vandersypen, Nature **442**, 766 (2006).
- [63] J. R. Petta, A. C. Johnson, J. M. Taylor, E. A. Laird, A. Yacoby, M. D. Lukin, C. M. Marcus, M. P. Hanson, and A. C. Gossard, Science **309**, 2180 (2005).
- [64] S. Foletti, H. Bluhm, D. Mahalu, V. Umansky, and A. Yacoby, Nat. Phys. **5**, 903 (2009).
- [65] J. M. Taylor, C. M. Marcus, and M. D. Lukin, Phys. Rev. Lett. **90**, 206803 (2003)
- [66] J. Baugh, Y. Kitamura, K. Ono, and S. Tarucha, Phys. Rev. Lett. **99**, 096804 (2007); phys. stat. sol. (c) **5**, 302 (2008).
- [67] R. Takahashi, K. Kono, S. Tarucha, and K. Ono, Phys. Rev. Lett. **107**, 026602 (2011).
- [68] R. C. Ashoori, Nature **379**, 413 (1996)
- [69] R. Takahashi, K. Kono, S. Tarucha, and K. Ono, Physica E **42**, 833 (2010)
- [70] K. Ono, D. G. Austing, Y. Tokura, S. Tarucha, phys. stat. sol. (b) **238**, 335 (2003)
- [71] K. Ono, D. G. Austing, Y. Tokura, S. Tarucha, Science **297**, 1313(2002)
- [72] A. Pfund, I. Shorubalko, K. Ensslin, and R. Leturcq, Phys. Rev. Lett. **99**, 036801 (2007); Phys. Rev. B **76**, 161308(R) (2007).
- [73] S. Nadj-Perge, S. M. Frolov, E. P. A. M. Bakkers, and L. P. Kouwenhoven, Nature **468**, 1084 (2010).
- [74] A. C. Johnson, J. R. Petta, J. M. Taylor, A. Yacoby, M. D. Lukin, C. M. Marcus, M. P. Hanson, and A. C. Gossard, Nature **435**, 925 (2005).

- [75] G. Burkard, D. Loss, and D. P. DiVincenzo" Phys. Rev. B **59**, 2070 (1999).
- [76] V. Fock, Z. Physik. **47**, 446 (1928); C.G. Darwin, Proc. Camb. Philos. Soc. **27**, 86 (1931).
- [77] W. G. van der Wiel, T. H. Oosterkamp, J. W. Janssen, L. P. Kouwenhoven, D. G. Austing, T. Honda, and S. Tarucha, Physica B **256**, 173 (1998).
- [78] M. Eto, Jpn. J. Appl. Phys. **38**, 376 (1999).
- [79] R. Hanson, L. P. Kouwenhoven, J. R. Petta, S. Tarucha, and L. M. K. Vandersypen, Rev. Mod. Phys. **79**, 1217 (2007).
- [80] F. H. L. Koppens, J. A. Folk, J. M. Elzerman, R. Hanson, L. H. Willems van Beveren, I. T. Vink, H. P. Tranitz, W. Wegscheider, L. P. Kouwenhoven, and L. M. K. Vandersypen, Science **309**, 1346 (2005).
- [81] D. G. Austing, T. Honda, and S. Tarucha, Jpn. J. Appl. Phys. **36**, 1667 (1997).
- [82] M. Wagner, U. Merkt, and A. V. Chaplik, Phys. Rev. B **45**, 1951 (1992).
- [83] S. M. Huang, Y. Tokura, H. Akimoto, K. Kono, J. J. Lin, S. Tarucha, and K. Ono, Phys. Rev. Lett. **104**, 136801 (2010).
- [84] T. Koder, K. Ono, Y. Kitamura, Y. Tokura, Y. Arakawa, and S. Tarucha, Phys. Rev. Lett. **102**, 146802 (2009).
- [85] S. Foletti, H. Bluhm, D. Mahalu, V. Umansky and A. Yacoby, Nature Phys. **5**, 903 (2009).